Backscatter Communication Solutions for Ubiquitous Sensing

Mohamad Katanbaf

A dissertation
submitted in partial fulfillment of the
requirements for the degree of

Doctor of Philosophy

University of Washington

2022

Reading Committee:

Joshua R. Smith, Chair

Payman Arabshahi

Matthew Reynolds

Program Authorized to Offer Degree:
Electrical and Computer Engineering

University of Washington

Abstract

Backscatter Communication Solutions for Ubiquitous Sensing

Mohamad Katanbaf

Chair of the Supervisory Committee:
Prof. Joshua R. Smith
Electrical and Computer Engineering

Backscatter communication suggests a low-cost solution to connect billions of devices through wireless signals and realize the vision of the Internet Of Things (IoT). However, due to challenges such as deployment complexity, reliability, and scalability, the promise of ubiquitous backscatter connectivity has eluded us. In this writing, I suggest three solutions to address these challenges and enable widespread backscatter connectivity. First, I introduce "Full-Duplex LoRa Backscatter" a low-cost, long-range monostatic backscatter solution that simplifies the deployment of low-cost backscatter systems. Next, I explain "Relacks" a bistatic backscatter system compatible with the BLE standard that exploits frequency and antenna diversity and a closed-loop design to deliver reliable backscatter coverage. Finally, I propose "MultiScatter", the first multistatic backscatter network for battery-free sensing, where a network of multiple receivers and transmitters base units are employed to deliver backscatter connectivity to many battery-free sensor nodes over a wide area.

TABLE OF CONTENTS

LIST OF FIGURES

LIST OF TABLES

ACKNOWLEDGMENTS

This dissertation is only made possible through the support and encouragement of many people to whom I owe my deepest gratitude.

First and foremost, I would like to thank my advisor, Professor Joshua Smith for his invaluable advice and unreserved support over the last several years. His deep technical knowledge, keen interest in diverse research problems, and the support and freedom he gives to me and other graduate students have set a great example to guide me in my own research journey and personal life. I feel truly fortunate to work with and learn from him.

I want to thank Professor Payman Arabshahi, Professor Matthew Reynolds, and Professor Mohammad Malakooti for their interest in my work and their valuable comments. It was an honor to have them on my committee.

I am deeply grateful to Professor Jacques Rudell, who admitted me to the Univerity of Washington and was my advisor for the first two years of my Ph.D. I learned so much about conducting and presenting research from him, and I want to thank him for that.

My labmates in Sensor Systems Lab have been a great source of help and support. I want to thank Ali Saffari, who I had the pleasure of working closely with on multiple projects, for his dedication, insightful discussions, and the many coffee breaks we had together. I would also like to thank Jared Nakahara for many fun and informative talks on many random topics. Brody Mahoney, Gregory Moore, Patrick Lancaster, Zerina Kepetanovic, Boling Yang, Shanti Garman, Kedi Yan, and Timothy Amish, it was a great pleasure knowing and working with you, and thank you for all your help over the past several years. I would also like to thank former UW students, Dr.Hossein Hosseini, Dr.Mehrdad Hessar, Dr.Vikram Iyer, Dr.Saman Naderiparizi, Dr.Tong Zhang, Dr.Kun-Da Chu, Dr.John Uehlin, Dr.Samrat

Dey, Dr.Chenxin Su, Fucheng Yin, Dr.Aaron Parks, Dr.Xingyi Shi, and Dr.Vaishnavi Ranganathan, for their friendship, help, advice, and many delightful conversations. And a special thanks to Dr.Ali Najafi, who encouraged me to join UW and has been a great friend since. His advice and comments have always helped me throughout my career.

I had the privilege of working with many great collaborators outside of our research group. I thank professor Gregor Henze, professor Soumik Sarkar, Sin Yong Tan, Dr.Anthony Florita, and Dr.Margarite Jacoby for their support and encouragement while we were working on the Whisper project. I would also like to thank professor Arka Majumdar, professor Suzie Pun, professor Bo Zhang, Dr.Quentin Tanguy, Lucy Yang, and Ruixuan Wan for the valuable discussions during our collaboration on the Touchscreen project.

The lessons I learned during my internships have contributed to this dissertation significantly. I would like to express my gratitude to Dr.Vamsi Talla for many insightful discussions during my several internships at Jeeva Wireless. I would also like to thank Dr. Vivek Jain for his mentorship and support during my internship at Bosch.

I thank Paul Allen School and the ECE department administrative staff for their help. Special thanks to Lisa Merlin for swiftly handling many purchase orders, and to Brenda Larson for her thorough advice and support whenever I went to her office with a question.

When I first arrived in the United States, I was fortunate to meet Samia Ashraf and Lou Davidson through UW FIUTS. I am deeply grateful for all their kindness and support over the years, especially for including us in every Thanksgiving dinner!

I owe my deepest gratitude to my parents, Yousef and Tayebeh, and my sisters for their unconditional love, support, and encouragement over so many years. I am extremely fortunate to have them in my life.

Finally, I dedicate this thesis to my wife, Mojdeh, for sharing every moment of this journey with me. I am truly blessed to have her in my life, and I am forever grateful for her sacrifices that allowed me to pursue my dreams on the other side of the planet.

DEDICATION

To my dear wife, Mojdeh

Chapter 1

INTRODUCTION

The importance of data in solving the challenges that humankind faces is indisputable. From climate change and smart agriculture to early detection of diseases such as cancer and diabetes, researchers and scientists rely on data collected from physical sensors to find innovative solutions and improve the quality of life on the planet.

One of the main challenges toward widespread and ubiquitous fine-grained sensing is the sensor nodes' power dynamics. For most applications, using wires to deliver the required energy is not an option since it increases the cost and limits the deployment. Similarly, replacing batteries is an undesirable solution that requires constant human involvement and increases the cost. Ideally, the sensor nodes should be "battery-free" or "self-powered" systems, which means they should work with a battery for the entire duration of their lifetime, or harvest enough energy to support their sensing and communication needs.

Recent advances in energy harvesting [67, 184], wireless power transfer [203, 71], and low-power and low-cost integrated sensors [73, 32, 37] has made significant steps toward enabling the vision of ubiquitous connectivity. However, the energy required to transfer the data collected by the sensor to a central unit remains a barrier toward that vision. Fig. 1.1 compares the power consumption of several sensors, including temperature sensor, accelerometer, microphone, and image sensor, with the power consumption of several wireless communication solutions based on Bluetooth Low Energy (BLE), Zigbee, and WiFi. Current wireless communications solutions have several orders of magnitude higher power consumption compared to the sensors. Thus, lowering the energy required for wireless communication would significantly affect the power dynamics of the battery-free and self-powered systems.

Power consumption of low-power radio transceivers such as BLE is dominated by the

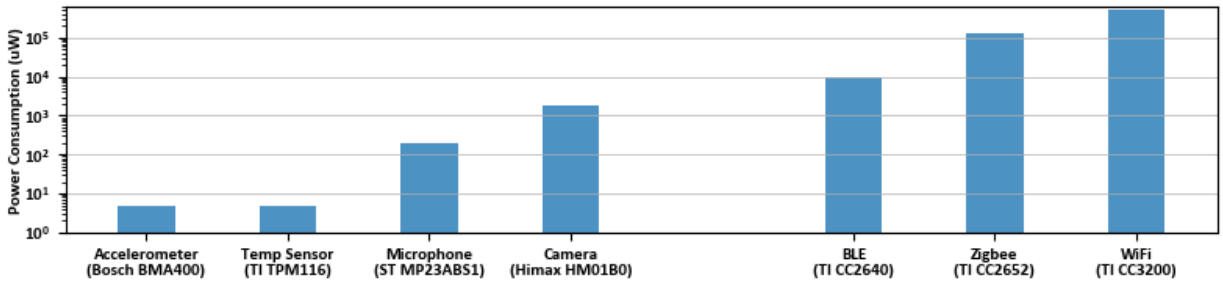

Figure 1.1: Power consumption of several sensors compared to wireless communication solutions.

relatively power-hungry local oscillator and power amplifier [70]. The power consumption of each circuit block is proportional to its operating frequency, and local oscillators and power amplifiers consume relatively high energy since they have to operate at hundreds of MHz to several GHz frequency bands. Sensors and baseband modulators work at a much lower frequency, and thus consume much lower energy. Backscatter communication is an ultra-low-power communication solution, where a device preserves energy by reflecting RF signals in the environment instead of generating them. In backscatter communication, the power-hungry high frequency circuits are taken out of the sensor node, and the low frequency data modulator is directly connected to the sensor node antenna. The backscatter device modulates the reflection by modifying the impedance connected to its antenna. The reflected power is proportional to the difference of the reflection coefficients of the loads connected to the antenna [195]

Commercial RFID tags use the backscattering principle to communicate with RFID readers. However, the high cost of the RFID reader infrastructure and their relatively short communication distance have limited their adaptation in many applications. Recent works have shown the possibility of backscatter systems using low-cost embedded radios in devices such as smartphones [125, 108, 89]. These works utilize the available radios for backscatter communication and and eliminate the initial cost of the dedicated infrastructure. However, we need to examine several aspects of the backscatter wireless network design to make

practical solutions and pave the way toward integrating backscatter solutions in everyday life. First of all, most previous works use separate transmitter and receiver units which results in complex coverage planning and deployment scenarios. Furthermore, the reliability of backscatter systems especially in multipath-rich indoor environments is not investigated thoroughly. Finally, the backscatter nodes limitations must be considered in the design of wireless networks protocols. In this work, I propose several techniques to tackle the remaining challenges in deploying low-cost, reliable, and scalable backscatter wireless networks for ubiquitous sensing.

1.1 Simplifying Backscatter Deployments

A conventional half-duplex deployment requires two devices - a transmitter and a receiver- to communicate with a backscatter tag. The transmitter emits the continuous wave carrier, the tag generates a packet by reflecting this signal at an offset frequency, and the receiver demodulates the backscattered packet to recover data. However, in addition to the backscattered packet, the receiver also experiences an interference at the adjacent frequency due to the continuous wave carrier. Half duplex systems solve the self interference problem by physically separating the transmitter and receiver. This requirement of two physically-separate plugged-in devices and need for co-ordination across three instead of just two devices is a major limiting factor.

To resolve these issues, we need to combine the transmitter and receiver into a single device which both generates the carrier and decodes the backscattered packet. We call this the full-duplex backscatter reader. This would bring the backscatter deployment on par with conventional wireless systems, wherein two devices communicate with each other. It is important that when we bring the transmitter and receiver in a single device, we do not significantly degrade performance and system characteristics, when compared to a half-duplex system.

In chapter 2, I propose "Full-Duplex LoRa Backscatter", the first long-range full-duplex LoRa backscatter reader. I leverage existing LoRa chipsets as transceivers and use a micro-

controller combined with inexpensive passive elements such as a hybrid coupler, inductors, tunable capacitors, and resistors to achieve 78 dB of self-interference cancellation and build a low-cost, low-complexity, and small-form-factor monostatic backscatter reader. I introduce a novel, two-stage, tunable impedance network that provides the fine-grain control and coverage necessary to meet the required carrier cancellation target across the expected range of variation in antenna impedance.

FD LoRa Backscatter reader costs less than $28, and it can successfully communicate with a backscatter tag at distances of up to 300 feet in line of sight, which is a 6 $\times$ improvement over previous systems. Also, I demonstrate the efficacy of using this technology in medical devices by communicating with a contact-lens-form-factor tag, and in smart agriculture by attaching the reader to a quadcopter and communicate with the tags placed on the ground.

1.2 Improving Backscatter Reliability

Although full-duplex backscatter nodes make the deployment easier, but the fact is that there are many half-duplex radios around us right now. For example, most appliances, and many light bulbs are equipped with embedded radios that connect them to smart home networks. These radios can cooperate to form backscatter network and deliver low-cost wireless connectivity to many everyday objects. This would enable many new applications such are monitoring the temperature inside a pot or tracking human interactions with different objects in living spaces. While previous works have proved the "possibility" of bistatic backscatter communication with BLE, WiFi, LoRa, or other wireless standards, the question of reliability of these links is not investigated thoroughly.

In chapter 3, I explain why previous open-loop systems commonly used in conventional active communication standards, where transceivers follow pre-defined or fixed patterns for selecting communication parameters, are not suitable for backscatter links. I propose "Relacks", a closed-loop backscatter system where the results of previous communication attempts are used to filter communication parameters and deliver a reliable backscatter coverage over an entire area. Relacks exploits diversity sources such as communication fre-

quency and transceivers antennas based on the channel metrics to combat the spatial and frequency dependant multi-path loss and the high propagation loss in backscatter wireless channels. I prototype a backscatter system with Bluetooth Low Energy (BLE) transceivers and BLE compatible tags and show that the proposed algorithm for selecting communication parameters achieves an average 2.7 × success rate compared to the random selection.

1.3 Wide-Area Backscatter Networks

Backscatter systems suffer from a shorter communication range than conventional active radios, since the wireless signal has to propagate twice, from carrier source to the tag, and from tag to the receiver. Thus, a single receiver-transmitter system is insufficient to cover a multi-bedroom or multi-floor house at practical data rates. The limited coverage of backscatter systems complicates the user experience and limits their use cases. Multiple base units can be employed to extend the coverage of a wireless networks, as shown in cellular and WiFi networks. However, high propagation loss, strong interference, frequency-dependant operation and non-homogeneous base units complicates the deployment of a backscatter network with multiple base units. Furthermore, the battery-free sensor nodes have strict energy limitations, while the base units have higher computational and energy resources. This imbalance requires the system to push the network management tasks to the base units while keeping the sensor nodes as simple as possible.

In Chapter 4, I introduce "MultiScatter", the first wide-area and scalable backscatter network with multiple receivers and transmitters base units for communication with battery-free sensor nodes. MultiScatter circumvents the inherent limitations of backscatter systems -including the limited coverage area, frequency-dependent operability, and sensor node limitations in handling network tasks- by introducing several coordination techniques between the base units starting from a single RX-TX pair to networks with many RX and TX units. I also develop a deployment planning tool which helps in finding the optimum placement for the base units to maximize the coverage in indoor environments. The MultiScatter prototype includes the RX and TX base units, and battery-free sensor nodes equipped with tempera-

ture, humididty and iluminance sensors, camera and microphone. I deploy MultiScatter in different settings such as an apartment and a multi-floor educational complex, and use it for occupancy detection in a case study.

Chapter 2

SIMPLYFYING BACKSCATTER DEPLOYMENTS: FULL-DUPLEX LORA BACKSCATTER

2.1 Introduction

Recent advances [145, 125, 108, 206, 190, 163] have demonstrated the potential of backscatter to replace power-hungry, large, expensive radios with an orders of magnitude lower power, smaller-size, cheaper, potentially battery-free connectivity solution. This promise, however, has run into practical limitations in regard to existing backscatter infrastructure. Full-duplex (FD) RFID readers [34, 43] and other proprietary full-duplex systems [69, 60], in which a single reader communicates with tags are easy to deploy, but these existing readers are large, complex, expensive, and have limited range.

To address this, recent half-duplex (HD) backscatter systems have leveraged the economies of scales and ubiquity of industry-standard protocols such as WiFi [125, 206], Bluetooth [90, 208, 119], ZigBee [141, 208], and LoRa [190, 163] to reduce the cost, size, and complexity of reader infrastructure and achieve longer range. However, these systems suffer from deployment issues, as the half-duplex topology requires two physically-separated radio devices: one for transmitting the carrier, and another for receiving the backscattered data packet. The need to deploy multiple devices in different locations significantly limits the use cases for backscatter.

We present the first Full-Duplex LoRa Backscatter reader which combines the low-cost, long-range, and small-form-factor benefits of a standard-protocols-compliant backscatter system with the simple deployment of a full-duplex system. This addresses one of the remaining pain points of backscatter and opens backscatter to a plethora of applications. A low-cost, long-range, small-form-factor full-duplex reader could be easily integrated into ex-

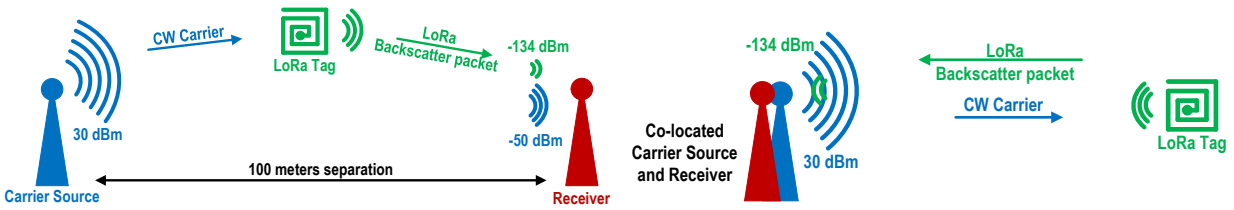

(a) **Half-Duplex deployment.** The carrier source and receiver are separated by 100m to mitigate carrier interference.

(b) **Full-Duplex deployment.** The carrier source and receiver are co-located and need 78 dB interference cancellation.

Figure 2.1: Overview of HD and FD Backscatter Deployments.

isting devices. This would enable peripheral, wearable, and medical devices such as pill bottles [65, 155], insulin pens [98, 131], smart glasses [130, 170], and contact lenses [110, 72] to use backscatter to directly communicate with a cellphone, tablet, or laptop. Similarly, in agriculture, aerial surveillance drones could be equipped with a backscatter reader to collect data from sensors distributed throughout a field.

To understand the challenge in building an FD LoRa Backscatter reader, consider the traditional HD LoRa backscatter system, shown in Fig. 2.1(a). The first radio transmits a single-tone carrier at power levels up to 30 dBm. A tag uses subcarrier modulation to backscatter a packet at an offset frequency, which is then received by the second radio, 100 m from the transmitter. The physical separation is necessary to attenuate the out-of-band carrier at the receiver to a level where it does not impact the sensitivity [190]. This illustrates the fundamental challenge in a FD LoRa Backscatter system, as shown in Fig. 2.1(b): The single-tone carrier needs at least 78 dB of suppression, a 63-million $\times$ reduction in signal strength, between the transmitter and a commodity LoRa receiver chipset, both integrated on the same PCB. This suppression must be implemented in the analog RF domain without substantially increasing the cost, complexity, or power consumption of the system. Furthermore, unlike path-loss attenuation, which is wide-band, typical cancellation techniques have a trade-off between cancellation depth and bandwidth [62, 132, 142]. If the

cancellation bandwidth is insufficient, the carrier phase noise will show up as in-band noise at the receiver. Therefore, a second requirement is to bring the phase noise of the carrier at the offset frequency to below the receiver's input noise level.

Existing FD cancellation techniques, including analog, digital, and hybrid designs used in full-duplex radios have different or more relaxed requirements and, as a consequence, are insufficient to meet the needs of our system. Analog and hybrid cancellation techniques require bulky and expensive RF components such as circulators [17], vector modulators [42], and phase shifters [44] to achieve sufficient cancellation, each of which increases cost and size. Digital cancellation techniques require access to IQ samples, which are unavailable on commodity radios, and instead use SDRs [62, 186, 69, 55], FPGAs [196], or DSPs [59], which are all prohibitively expensive. For a detailed analysis of why existing techniques are insufficient, see §2.8.

Our key idea is to leverage the ubiquity and economies of scale of existing LoRa transceivers and microcontrollers and add inexpensive passive components to fulfill the two requirements of full-duplex operation. This enables us to build a *low-cost, long-range, small-form-factor*, Full-Duplex LoRa Backscatter reader. We use a single-antenna topology with a hybrid coupler to interface the transmitter and the receiver with the antenna. The leakage from the transmitter to the receiver, i.e. self-interference, is a function of the impedance at the coupled port. A microcontroller adaptively tunes an impedance network, tracking variations in the antenna impedance and environmental reflections with the objective of minimizing interference at the receiver.

We introduce a *novel, two-stage, tunable impedance network* to achieve 78 dB suppression of carrier signal. The extent to which a carrier is suppressed is a function of how closely the tunable impedance can track the variations in antenna impedance, which in turn depends on the resolution of the impedance network. A single-stage network is limited by the step size of its digital capacitors and does not have a high enough resolution to reliably achieve 78 dB cancellation [114, 123, 142, 75]. Our two-stage network is built by cascading two stages, each consisting of four, 5-bit tunable capacitors and two fixed inductors with an attenuating

resistor network between the stages. The two-stage design provides the fine-grain control and coverage necessary to meet the 78 dB carrier cancellation target across the expected range of variation in antenna impedance. To achieve the second objective of bringing the phase noise of the carrier at the offset frequency below the noise floor of the receiver, while simultaneously obtaining 78 dB cancellation at the carrier frequency, is very challenging. There is a fundamental trade-off between the cancellation depth and bandwidth [62, 132, 142], and we prioritize the 78 dB cancellation requirement at the carrier frequency. We use a COTS synthesizer with low phase noise to relax the cancellation requirement at the offset frequency.

We implement the Full-Duplex LoRa Backscatter system using only COTS components, for a total cost of $27.54 at low volumes, only 10% more than the cost of two HD units. Our evaluation shows that the two-stage impedance network achieves $> 78\ dB$ carrier cancellation and $> 46\ dB$ of offset cancellation in practical scenarios with a tuning time overhead of less than 2.7%. Results are summarized below:

- The FD reader can communicate with tags at distances of up to 300 ft in line of sight. When placed in the corner of a 4,000 ft^2 office space with concrete, glass, and wood structures and walls, tags can operate within the entire space.
- We integrate a low-power configuration of the FD reader into portable devices. We attach the prototype to the back of a smartphone and show that the tags can communicate at distances beyond 50 ft at 20 dBm, 25 ft at 10 dBm, and up to 20 ft at 4 dBm.
- We build two proof-of-concept applications. We prototype a contact-lens-form-factor antenna tag and show that it can communicate with FD reader attached to a smartphone at distances of up to 22 ft and when the reader is inside a user's pocket. We also attach the FD reader to a quadcopter and fly it to 60 ft above a field. The reader is able to communicate with tags placed on the ground at a lateral distance of up to 50 ft, corresponding to an instantaneous coverage of 7,850 ft^2.

2.2 Background

Our work brings full-duplex operation to a LoRa Backscatter system. We start with a background on LoRa backscatter, followed by a primer on the full-duplex operation.

2.2.1 LoRa Backscatter Primer

Backscatter communication eliminates RF carrier generation at the tag and, instead, uses switches to reflect existing, ambient RF signals for data transmission. This drastically reduces the cost, size, and power consumption of wireless communication [125, 190, 60]. In HD backscatter deployment, as shown in Fig. 2.1(a), a radio source generates the single-tone carrier, a backscatter tag reflects the carrier to synthesize LoRa packets, then a receiver decodes the backscattered packets. However, the carrier signal also ends up as a strong source of interference at the receiver, which degrades the receiver's ability to decode packets. Backscatter systems use two key techniques to mitigate carrier interference [90, 208, 125, 108, 53, 213, 141, 190, 163, 106, 215, 176, 180, 113]. First, the tag uses subcarrier modulation to synthesize packets at a frequency offset from the carrier frequency. The receiver operates at the offset frequency, pushing the interference, i.e. the carrier signal, out of band at the receiver. Since receivers are designed to operate in the presence of out-of-band interference, the receiver can decode the backscattered packets with minimal loss in sensitivity. Second, the transmitter and receiver are physically separated to attenuate that carrier to a level where it does not affect the receiver's sensitivity. However, in full-duplex systems, by definition, the transmitter and receiver cannot be physically separated.

LoRa receivers have low sensitivity and high blocker tolerance, making them ideal candidates for long-range backscatter connectivity, as demonstrated by prior HD backscatter designs [190, 163]. LoRa has two key protocol parameters that can be used to trade off data rate with receive sensitivity: spreading factor and bandwidth. Since our system transmits up to 30 dBm, the FCC mandates frequency hoppingand a maximum channel dwell time of 400 ms [30]. So, we limit our system to protocols with packet lengths shorter than this limit,

which corresponds to a sensitivity of -134dBm. Longer packet lengths are incompatible with frequency hopping unless we implement intra-packet frequency hopping. Doing so would require tuning in the middle of packet reception, which is not feasible on commodity radio receivers.

2.2.2 Full-Duplex Primer

FD radios transmit and receive at the same time on a single device, allowing simultaneous communication between devices without delay. The main obstacle in achieving FD functionality is self-interference; the strong transmit signal leaks to the sensitive receiver and appears as interference, degrading its performance. Hence, the key is to suppress the interference before it reaches the receiver. Broadly speaking, there are two approaches to FD operation: out-of-band and in-band.

Cellular standards such as WCDMA and LTE implement out-of-band full-duplexing by using Frequency Division Duplexing (FDD), where two distinct fixed frequency bands are used for uplink and downlink. In FDD systems, the operating frequency and frequency offset are fixed, and a frequency selective duplexer is used to suppress the transmitter leakage in the receive band. At first glance, it may look like FD backscatter is similar, as the tag backscatters the data packet at a frequency offset, however, FDD systems use much higher offset frequencies, at least 40 MHz for WCDMA and LTE bands above 800 MHz [39], in line with the requirements of practical frequency duplexers and passive filters. Backscatter systems, in contrast, transmit the carrier and receive the packet within the same frequency band, keeping the frequency offset low to minimize the power consumption of the tag. For example, the LoRa backscatter system operating in the 902-928MHz ISM band uses an offset frequency of 2-4 MHz. With such a small offset, we cannot leverage passive filters or frequency duplexers used in FDD systems.

In recent years, researchers have demonstrated success with In-Band Full-Duplex (IBFD) radios [62, 132, 86, 69], where radios transmit and receive simultaneously on the same frequency. IBFD radios suppress self-interference by using a combination of analog and digital

cancellation techniques to bring the signal strength of the typically-wideband carrier below the noise floor of the receiver over the entire receive bandwidth. IBFD radios use isolation and analog cancellation techniques in the RF domain to first bring the carrier signal below the saturation level of the receiver front end. Next, digital cancellation techniques are used in the baseband to suppress the signal below the noise floor across the receiver bandwidth. Since the frequency offset in a backscatter system is small, an FD backscatter system can leverage SI suppression techniques similar to IBFD devices, such as isolation and analog cancellation. However, there are two key differences. First, the FD LoRa Backscatter system uses a single-tone signal as the carrier, so we need to suppress a very narrow-band signal. Second, unlike IBFD radios, the FD LoRa Backscatter system uses existing COTS radios, which do not provide access to signals in the digital baseband of the receiver. Hence, unlike IBFD systems, which use digital cancellation in addition to analog cancellation, we need to achieve 78 dB of SI cancellation entirely within the analog domain.

2.3 FD LoRa Backscatter Requirements

In this work, we focus on the cancellation requirements for a LoRa backscatter system, but the design techniques and architecture are not LoRa specific. They can be extended to build FD backscatter systems for other wireless standards such as WiFi, Zigbee, Bluetooth, SigFox, or NB-IoT that use a single-tone carrier and subcarrier modulation to synthesize backscatter packets [125, 90, 108]. However, these techniques are not directly applicable to systems which do not use sub-carrier modulation [60] or use wide-band Wi-Fi or LoRa packets as carrier [208, 163, 141].

We divide the cancellation requirements into two categories: carrier cancellation and offset cancellation.

2.3.1 Carrier Cancellation

We define carrier cancellation (CAN_{CR}) as the required cancellation of the carrier signal (the source of self-interference) at the center frequency. The carrier acts as a *blocker* i.e. a strong

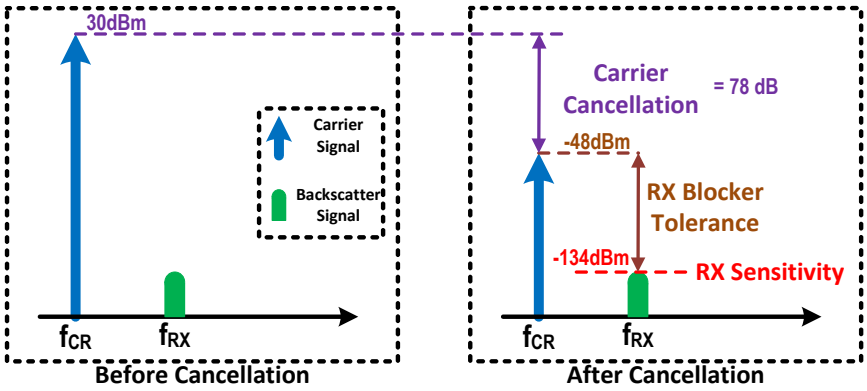

Figure 2.2: Carrier Cancellation. The 30 dBm single-tone carrier needs 78 dB of attenuation to meet the Rx blocker tolerance and ensure packet reception down to Rx sensitivity.

signal in the vicinity of the desired signal that can affect a receiver's performance and reduce its sensitivity. A strong blocker can saturate the LNA, forcing it to reduce gain and increase the noise floor. Secondly, post LNA, a blocker can mix with the receiver local-oscillator phase-noise and contribute to in-band noise. Finally, baseband filters have limited stopband attenuation, and even a small portion of the blocker passing through the filter reduces the signal-to-noise and -interference ratio.

We compute the minimum required carrier cancellation as

$$CAN_{CR} > P_{CR} - Rx_{Sen} - Rx_{BT} \tag{2.1}$$

where P_{CR} is the carrier power, Rx_{Sen} is the receiver sensitivity, and Rx_{BT} is the receiver blocker tolerance.

For example, as per the SX1276 datasheet, the blocker tolerance at a 2 MHz offset for BW=125 KHz, SF=12, -137 dBm sensitivity protocol is 94 dB [36]. Based on equation 2.1, for P_{CR} = 30 dBm, at least 73 dB of SI cancellation is required. However, the datasheet blocker specification assumes a 3 dB degradation in sensitivity, which is substantial for backscatter systems. Additionally, the datasheet provides blocker specifications for only a subset of frequency offsets and protocol parameters. To get a more comprehensive set of

requirements, we perform our own blocker experiments for a range of frequency offsets (2, 3, and 4 MHz) and protocol parameters (366 bps - 13.6 Kbps data rates). We connect a LoRa transmitter and a single-tone generator to two variable attenuators and combine their outputs at a LoRa receiver. First, we get a baseline sensitivity by turning off the single tone and increase the LoRa transmitter attenuation till we reach receiver sensitivity, defined by PER $< 10\%$. Next, we turn on the single-tone generator with maximum attenuation and reduce the attenuation, thereby increasing blocker power, until the PER exceeds 10%. We record the maximum tolerable interference power for different frequency offsets, receiver bandwidths, and spreading factors to achieve different data rates and conclude that 78 dB is the most stringent carrier-cancellation specification. As mentioned prior, the blocker performance of a receiver depends on both the RF front end and digital baseband. Our analysis shows that the SX1276 baseband has sufficient digital baseband filtering to suppress the blocker at the offset frequency, and additional filtering would not help in this specific case.

Fig. 2.2 illustrates the carrier cancellation requirement. Before cancellation, the carrier signal is much stronger, but after cancellation, the SI is dropped to a level that the receiver can tolerate. The difference between these levels is CAN_{CR}. Note that a lower cancellation may suffice for some data rates and frequency offsets, but our design supports all configurations.

2.3.2 Offset Cancellation

We define offset cancellation (CAN_{OFS}) as cancellation of the carrier signal at the offset frequency. We use a single-tone signal as the carrier. An ideal oscillator generates a pure sine wave, with the entire signal power concentrated at a single frequency. However, practical oscillators have phase-modulated noise components, which spreads the power to adjacent frequencies. This results in noise side bands [171] and is characterized by the source's phase noise, i.e. power spectral density (dBc/Hz) of the noise at a frequency offset from the center frequency. Since the receiver operates at a frequency offset from the carrier, the carrier phase

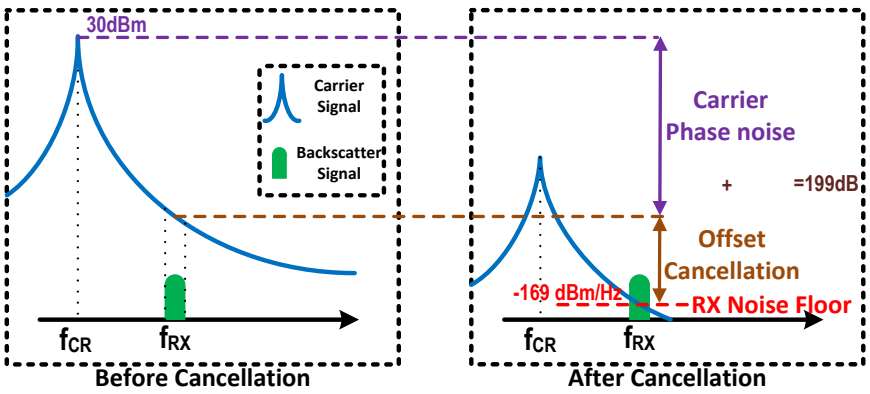

Figure 2.3: Offset Cancellation. The phase noise of the single-tone carrier at the frequency offset after cancellation should be less than the noise floor of the receiver.

noise shows up as in-band noise to the receiver. For optimal receiver performance, the SI signal after cancellation at the offset frequency should be less than the receiver noise floor. We compute the minimum required offset cancellation as

$$\begin{aligned} P_{CR} + \mathcal{L}_{CR(\Delta f)} + 10Log(B) - CAN_{OFS} &< 10Log(KTB) + Rx_{NF} \\ CAN_{OFS} - \mathcal{L}_{CR(\Delta f)} &> P_{CR} - 10Log(KT) - Rx_{NF} \end{aligned} \tag{2.2}$$

where $\mathcal{L}_{CR(\Delta f)}$ is the carrier phase noise at the offset frequency (Δf), B is the receiver bandwidth, K is the Boltzmann constant, T is temperature, and Rx_{NF} is receiver noise figure. We show this requirement in Fig. 2.3. Before cancellation, the backscattered signal is buried under the carrier phase noise, but, after cancellation, the carrier phase noise is pushed below the receiver noise floor.

As per the SX1276 datasheet $Rx_{NF} = 4.5$ dB, so for $P_{CR} = 30$ dBm, $CAN_{OFS} - \mathcal{L}_{CR(\Delta f)} > 199.5$ dB. The offset cancellation depends on transmit power, carrier phase noise, and receiver noise figure. Interestingly, since the channel bandwidth appears on both sides of equation 2.2, offset cancellation is independent of the receiver channel bandwidth. In other words, we can use the carrier phase noise per unit bandwidth and receiver noise floor per

unit bandwidth instead of the aggregate noise over the entire bandwidth.

In an HD system, the transmitter and receiver are physically separated, and the carrier attenuation via RF propagation does not significantly change with frequency. So, if the 78 dB carrier cancellation requirement is met, the phase noise at the offset frequency would also be attenuated by the same amount. However, cancellation networks do not have the same wide-band frequency characteristics [85, 172, 123, 142, 75]. The inequality shows that satisfying the offset cancellation requirement for an FD system requires a joint design of the carrier source and the cancellation network. If we use a high-phase-noise carrier, we would need high offset cancellation, whereas if we lower the phase noise of the carrier source, we can relax the offset cancellation requirements. Carrier and offset SI cancellation are functions of offset frequency, and both typically relax with an increase in offset frequency. However, an increase in offset frequency increases the tag power consumption. Thus, the frequency offset presents a trade-off between tag power consumption and SI cancellation requirements. 2-4 MHz is a reasonable compromise; we use a 3 MHz offset frequency in this work.

2.4 FD LoRa Backscatter Reader Design

The FD LoRa Backscatter system uses a single antenna and a hybrid coupler with a two-stage tunable impedance network to achieve carrier and offset cancellation. The cancellation network uses only passive components, minimizing cost, complexity, power consumption, and noise. Fig. 2.4 shows the block diagram of our design. The antenna is connected to the transmit and receive paths via a hybrid coupler. The fourth port of the coupler is connected to a tunable impedance network that tracks the antenna impedance to reflect and phase shift a portion of the single-tone carrier, suppressing the SI that flows to the receiver. The carrier signal is generated by a frequency synthesizer and fed to a power amplifier (PA) to transmit up to 30 dBm. An on-board microcontroller controls the synthesizer, PA, receiver radio, and digital tunable impedance network using a SPI interface. We use RSSI readings from the receiver to measure the SI there.

Below, we describe the principle of operation for the hybrid coupler. This is followed by

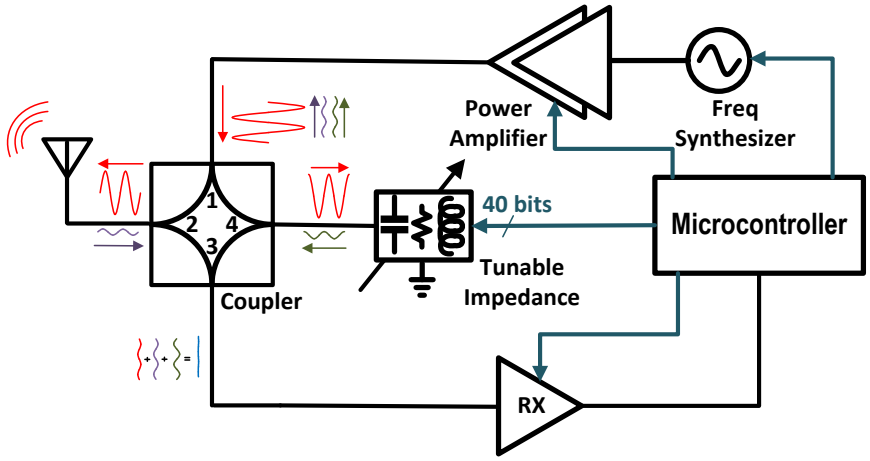

Figure 2.4: System Architecture. We use a single-antenna hybrid-coupler architecture with a two-stage tunable impedance network for cancellation. A microcontroller controls all components and implements the tuning algorithm.

the two-stage tunable impedance network design and the choice of carrier source to meet the carrier and offset cancellation requirements. Finally, we describe the tuning algorithm.

2.4.1 Coupler: Principle of Operation

Couplers are four-port devices that divide an incident signal between the output and coupled port while keeping the fourth port isolated [162, 166]; we use this property to isolate the transmitter and receiver. We connect the transmitter to the input port (1), the receiver to the isolated port (3), the antenna to the output port (2), and the tunable impedance network to the coupled port (4). The carrier signal is split between the antenna and coupled ports, leaving the receiver isolated. The received signal at the antenna port is split between the receiver and the transmitter, leaving the tunable impedance isolated. Couplers are reciprocal elements, meaning that the signal split described above is symmetrical. Ideally, we would want the entire PA output to go to the antenna (low TX insertion loss) and the entire received signal from the antenna to go to the receiver (low RX insertion loss). A

higher coupling factor would direct more of the PA output to the antenna at the cost of reducing signal transmission from the antenna to the receiver. Since our goal is to maximize the communication range, we must minimize the sum of the transmit and receive insertion losses. A hybrid, or 3 dB coupler, equally divides the input power between the output and coupled ports and minimizes total loss to 6 dB.

Two factors limit the practical SI cancellation of a hybrid coupler. First, every coupler has leakage: a typical COTS coupler provides $\sim$ 25 dB of isolation between the transmit and receive ports [28], far lower than our requirement. Second, and more important, is the effect of the antenna. Typical antennas, including low-cost PIFAs, are characterized by -10 dB return loss, and any reflection from the antenna port would couple to the receiver and further contribute to the SI.

Antenna Impedance Variation. Environmental variations affect antenna impedance, i.e. nearby objects can detune the antenna or create additional reflections that contribute to variation in its reflection coefficient. Since SI cancellation is dependent on antenna impedance, it is essential to characterize the expected variation. We design a 1.9 in $\times$ 0.8 in PIFA for our implementation and use this antenna to quantify impedance variation. We connect the PIFA to an Agilent 8753ES VNA [4] and subject it to environmental variations by placing the antenna upright on a table, and measure S_{11} as a hand and other objects approach it from different directions. Our results show that the magnitude of the reflection coefficient, $|\Gamma|$, reaches a maximum of 0.38, and we set expected $|\Gamma| < 0.4$ for the antenna.

2.4.2 Two-Stage Tunable Impedance Network

We use a tunable impedance at the coupled port [114, 123, 142] to negate SI leakage due to variation in antenna impedance. However, the cancellation depth is a function of how precisely we can tune this impedance. To achieve 78 dB carrier cancellation, we need a very fine resolution for the tunable impedance, which is not available in COTS digital capacitors. To solve this, we introduce a novel two-stage tunable impedance network that allows us to achieve deep cancellation, using only passive components.

To understand how the tunable impedance network improves the SI suppression from the coupler, follow the flow of signals in Fig. 2.4. The carrier (red) splits between the antenna port and the coupled port. The impedance at the coupled port is tuned such that the reflection from this port (green) cancels out both the leakage of the coupler and the reflection from the antenna port (purple) to achieve deep cancellation at the receive port (blue). In the worst case of a significantly detuned antenna, reflection from the antenna is much stronger than the leakage, and this should be canceled by the reflection from the tunable impedance.

We use a topology of two fixed inductors and four digitally tunable capacitors terminated with a resistor to cover the range of expected impedance values required to cancel strong reflections from the antenna [142]. We observe that in a tuning network terminated with a resistor, only a small portion of the signal is reflected, and most of it is dissipated. We replace the termination resistor with a resistive signal divider, followed by a second tunable impedance, as shown in Fig. 2.5(a). The signal reflected by the second stage flows through the resistive divider twice, effectively lowering the impact of impedance changes in the second stage on the overall reflected signal. This allows us to use the second stage to make much more fine changes in impedance, increasing the tuning resolution and enabling deep cancellation. However, the first stage still determines the tuning range and offset cancellation. The second stage provides the fine resolution to accurately match the reflection from the balanced port with the leakage and reflection from the antenna port. To eliminate dead zones, we choose the resistive divider such that the fine tuning network covers the step size of the coarse tuning network. This coarse and fine tuning approach is similar to using a hybrid coupler combined with an analog feed-forward path. The second stage effectively provides the functionality of a feed-forward path, but without additional noise and at a lower cost, lower complexity, and lower power.

We simulate the behavior of our tunable impedance network to demonstrate the efficacy of our approach. We plot the tuning network reflection coefficient at 915 MHz in Fig. 2.5 (c) for a step size of six LSBs for each capacitor in the first stage. For visibility, the plot only shows 1,296 impedance states out of more than 1 million first-stage impedance states

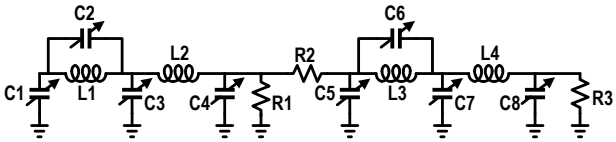

(a) Topology of the two stage impedance network.

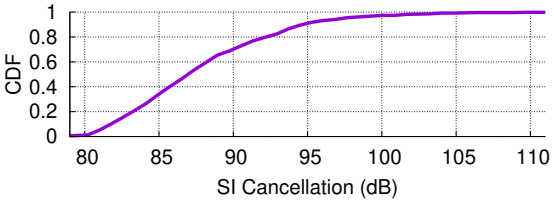

(b) Simulated SI cancellation for 400 random antenna impedance

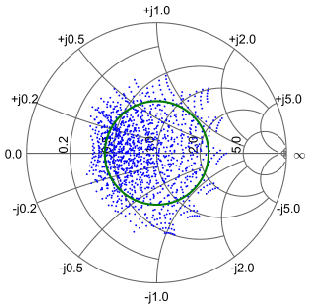

(c) Tunable impedance coverage (step size = 6 LSBs)

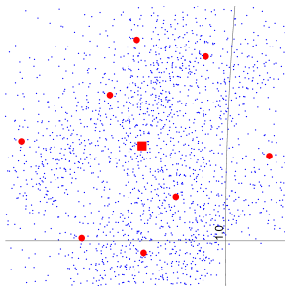

(d) Second stage fine tuning. (step size = 10 LSBs)

Figure 2.5: Two stage tunable impedance network used for SI cancellation and its simulation results.

and more than 1 trillion total states. The plot demonstrates that our design can cover the impedances corresponding to the antenna reflection coefficient circle of $|\Gamma| < 0.4$. Next, we show the fine tuning of the second stage in Fig. 2.5 (d). We select an initial state (the large, red square in the center) and change each capacitor in the first stage by one LSB to get the other eight red dots. Without the second stage, we would not be able to achieve any impedance between these dots. For each of these nine states, we use a step size of 10 LSBs for each capacitor in the second stage and show the resulting impedances in blue. The blue cloud shows the fine resolution control covering the dead zone between the first-stage steps. Finally, we simulate SI cancellation for 400 random points of antenna impedance inside the $|\Gamma| < 0.4$ circle and plot the cancellation CDF in Fig. 2.5 (b). Cancellation of > 80 dB is achieved for the 1st percentile, which satisfies our requirement.

2.4.3 Carrier Source Selection

The phase noise of the carrier source determines the required cancellation at the offset frequency, as shown in equation 2.2. In order to understand the requirements of the carrier

source, we first simulate SI cancellation at different frequency offsets. We tune the capacitors to achieve a minimum of 78 dB carrier cancellation and then sweep the operating frequency. Our results show that at 3 MHz frequency offset, 47 dB cancellation or more is achieved in 90% of the simulated cases. If we use SX1276 with a phase noise of -130 dBc at 3 MHz offset as our transmitter, then 47 dB of offset cancellation is insufficient.

The tuning network has multiple poles that can be optimized to increase cancellation bandwidth [142, 126]. However, doing so reduces the cancellation at the center frequency. This approach would also require a wide-band receiver to provide feedback on the SI power over the entire bandwidth to tune the capacitors, which is unavailable on the SX1276 (max. BW = 500 kHz). We need $>$ 78 dB of SI cancellation at the carrier frequency and prioritize this requirement. Instead of SX1276, we use ADF4351 [18] frequency synthesizer to generate the single tone carrier, which has a lower phase noise of -153 dBc at 3 MHz offset. Although the ADF4351 is slightly more expensive, it relaxes the offset cancellation requirement to 46.5 dB and eliminates the need for an additional wide-band receiver or a power detector, justifying the design choice.

2.4.4 Tuning Algorithm

Our design uses a two-stage impedance network with eight digital capacitors, each with five control bits; a total of 40 bits resulting in 2^{40} ($\sim$ 1-trillion) states for the impedance network. Multiple capacitor states can result in the impedance required for 78 dB cancellation, and any one of those is acceptable. As it is impossible to search across such a vast space in real-time, there is a need for an efficient tuning algorithm that can run on a commodity ARM Cortex-M4 microcontroller.

We use a simulated annealing algorithm to tune the capacitors in each stage separately [197]. Simulated annealing is based on the physical process of heating, and then slowly cooling, a material to minimize defects in its structure. For every temperature value, we take ten steps. At each step, we add a random value bounded by a maximum step size to each capacitor and measure the SI using receiver RSSI measurement. We accept the new

capacitor values if the SI decreases, or with a temperature-dependent probability when the SI increases. We start with a temperature equal to 512 and divide it by two each round until it reaches one. We set predefined cancellation thresholds for each stage and stop the tuning once the thresholds are met. If the first stage reaches the threshold (set to 50 dB), but the second stage fails to do so, we repeat the tuning until either it converges or reaches a timeout.

2.5 Implementation

We implement the FD LoRa Backscatter reader for operation in 902-928 MHz on a 3.8 in $\times$ 1.9 in, 4-layer, FR4 PCB. We place the RF components, including antenna, transmitter, receiver, and cancellation network, on the top side of the PCB, and microcontroller and power management on the bottom. We use the SX1276 as the LoRa receiver [36]. The cancellation circuit consists of the X3C09P1 90° hybrid coupler [28] and a two-stage tunable impedance network, shown in Fig. 2.5 (a). Variable capacitors C_1-C_8 are implemented by pSemi PE64906 tunable capacitors, with 32 linear steps from 0.9 pF - 4.6 pF [20]. We set inductors L_1, L_3 to 3.9 nH and L_2, L_4 to 3.6 nH. We set resistors R_1, R_2, and R_3 to 62 Ω, 240 Ω, and 50 Ω respectively. We use the ADF4351 synthesizer to generate the single-tone carrier, which has 23 dB better phase noise at 3 MHz offset compared to the SX1276. The carrier output power can be amplified up to 30 dBm using the SKY65313-21 power amplifier [21]. Our cancellation technique has an expected loss of 7-8 dB; 6 dB of which is the theoretical loss due to hybrid coupler architecture, the rest is due to component non-idealities.

We design a custom coplanar inverted-F PCB antenna. The radiating element of the antenna measures 1.9 in $\times$ 0.8 in and leverages the existing ground plane for omnidirectional radiation. We measure the performance of the antenna in an anechoic chamber, and results show a peak gain of 1.2 dB, half-power beam-width of 80°, and cumulative efficiency of 78%. The transmitter, receiver, and cancellation network are controlled using a SPI interface by an on-board ARM Cortex-M4 STM32F4 microcontroller [22]. The microcontroller implements

a state machine in C to transition between tuning, downlink, and uplink operating modes. In the tuning mode, the microcontroller first configures the center frequency and power of the carrier and then tunes the impedance network to minimize SI using the simulated annealing algorithm described in §2.4.4. After the tuning phase, the MCU sends the downlink OOK message to wake up the backscatter tag. Then, it transitions to the uplink mode where it configures the receiver with the appropriate LoRa protocol parameters to decode backscattered packets. The MCU then repeats this cycle for the next frequency.

2.5.1 FD Reader Configurations

We configure the FD LoRa Backscatter reader for two different use cases; a 'base-station' setup and a 'mobile' setup. Below we describe each configuration.

Base-Station Configuration: The base-station configuration of the FD LoRa Backscatter reader uses a 8 dBc high gain patch antenna [49]. The synthesizer and PA are set to transmit at 30 dBm. These settings maximize operating range and we use this configuration for the line-of-sight and non-line-of-sight range testing. In the base-station setup method, the power amplifier, synthesizer, receiver, and MCU consume 2,580 mW, 380 mW, 40 mW, and 40 mW, respectively, resulting in total power consumption of 3.04 W. 3.04 W is not a limitation for a plugged-in device such as a smart speaker or WiFi router, but is too high for a portable device.

Mobile Configuration: For applications with lower power consumption and smaller size requirements, we configured the system as a 'mobile' version. We use the on-board antenna and configure the synthesizer and PA to transmit at lower power levels of 4 dBm, 10 dBm, and 20 dBm. Since the PA and synthesizer dominate power consumption, reducing transmit power greatly reduces power consumption. In this mobile configuration, power consumption is low enough to draw from conventional portable power sources like a USB battery or a laptop. It is also small enough that, if desired, we are able to attach it to an iPhone 11 Pro without increasing the phone's footprint, shown in Fig. 2.11(a).

Table 2.1: Estimated Power Consumption of FD LoRa Backscatter Reader

TX Power	Applications	Peak Power
30 dBm	Plugged-in devices	3,040 mW[+]
20 dBm	Laptops, Tablets	675 mW
10 dBm	Phones, Battery Packs	149 mW
4 dBm	Phones, Battery Packs	112 mW

[+] Measured result.

Lower transmit powers relax cancellation requirements (see §2.3.2), which can be leveraged to further reduce the power consumption of the synthesizer and the power amplifier. For 20 dBm output power, we can instead use an LMX2571 [15] as the synthesizer which has higher phase noise, but lower power consumption. We can also use a CC1910 [7] as the PA which operates efficiently at 20 dBm output power. Similarly, for output powers of 4 dBm and 10 dBm, we can use a CC1310 [24] as the synthesizer and eliminate the PA. These optimizations would reduce power consumption to levels shown in Table 2.1. Since we built our system for maximum output power and range, we did not make these hardware changes in this work, but we wish to outline the available design choices for use-cases demanding lower power consumption.

2.5.2 Cost Analysis

The FD LoRa Backscatter reader is designed with the goal of simplifying the deployment of backscatter technology to unleash the untapped potential of backscatter. Cost plays a critical role in achieving this objective. Table 2.2 outlines the cost structure of the different components of the system and compares it with a legacy HD LoRa backscatter reader. Our analysis using pricing data from Octopart [1] shows that at low volumes of 1,000 units, the FD reader costs $27.54, only 10% more than the cost of two HD readers. We believe that

Table 2.2: Cost Analysis of FD & HD Backscatter Hardware

Components	FD Cost	(2×) HD Cost
Transceiver	$4.16	(2×) $4.16
Synthesizer	$7.15	N/A
Power Amplifier	$1.33	(2×) $1.33
Cancellation Network	$5.78	N/A
MCU	$1.70	(2×) $1.30
Power Management	$2.25	(2×) $1.95
Passives	$2.52	(2×) $1.54
PCB fabrication [2]	$1.07	(2×) $0.79
Assembly [2]	$1.58	(2×) $1.38
Total	**$27.54**	**$24.90**

further optimization and leveraging economies of scale, coupled with the reuse of radios and processing power upon integration with existing devices such as IoT gateways, smartphones, and tablets, can further reduce the solution cost.

2.5.3 LoRa Backscatter Tag

The LoRa backscatter tag used in this work is based on the design proposed in [190]. The LoRa baseband and subcarrier chirp-spread-spectrum-modulated packets are generated using Direct Digital Synthesis (DDS) on an AGLN250 Igloo Nano FPGA [9]. The output of the FPGA is connected to SP4T ADG904 RF switch [11] to synthesize single-side-band backscatter packets. The backscatter tag design also incorporates an On-Off Keying (OOK) based wake-on radio with sensitivity down to -55 dBm and an ADG919 [12] SPDT switch to multiplex a 0 dBi omnidirectional PIFA between the receiver and the backscatter switching network. The total loss in the RF path (SPDT + SP4T) for backscatter is $\sim$ 5 dB.

2.6 Evaluation

First, we validate our cancellation approach by measuring the carrier and offset cancellation of our novel two-stage impedance tuning network. Then, we measure the time overhead incurred by our tuning approach. Next, we evaluate the FD LoRa Backscatter system performance in a wired setup to neutralize multi-path effects, followed by line-of-sight and non-line-of-sight wireless deployments. Finally, we measure the performance of the mobile version of our system.

Unless mentioned otherwise, we set the subcarrier modulation frequency to 3 MHz, and configure the tag to transmit 1,000 packets with SF=12, BW=250 KHz, (8,4) Hamming Code with an 8-byte payload, a sequence number for calculating PER, and a 2-byte CRC. Additionally, we initiate uplink by sending a downlink OOK-modulated packet at 2 kbps to wake up the tag and align the tag's backscatter operation to the carrier. Downlink also enables channel arbitration between multiple tags, sending acknowledgments, packet re-transmissions, and other functionalities [190, 125]. The evaluation of these features is beyond the scope of this work.

2.6.1 Cancellation Network

The cancellation network performance depends on the antenna impedance, which is sensitive to environmental variations (see §2.3.2). To demonstrate that our system can achieve the required cancellation across a range of expected antenna impedances, we simulate antenna impedances with custom circuit boards with an 0402 footprint and an SMA connector. We populate the pads with discrete passives to represent antenna impedances with $0 \leq |\Gamma| \leq 0.4$. We test seven antenna impedances, as shown on the smith chart in Fig. 2.6 (a).

To measure cancellation, we attach a board representing an antenna impedance to the antenna port of our FD LoRa Backscatter reader with a Murata measurement probe [25]. We disconnect the receiver and attach the receiver input to a spectrum analyzer using another

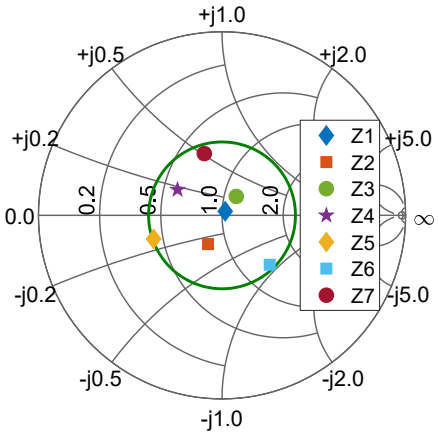

(a) Selected impedances.

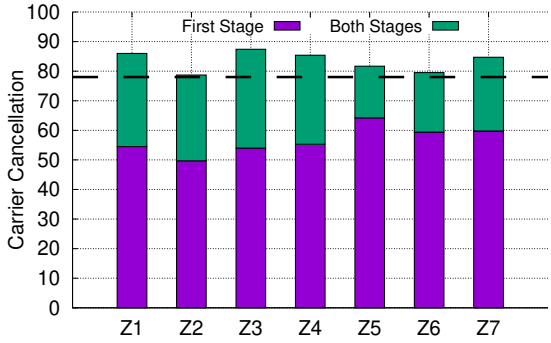

(b) First and second stage carrier cancellation.

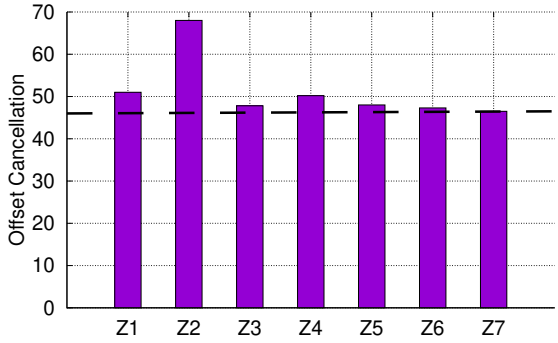

(c) Cancellation at 3MHz subcarrier offset.

Figure 2.6: SI cancellation as a function of variation in antenna impedance.

RF probe. We set the transmitter to 915 MHz and 30 dBm output power. Since the receiver is disconnected, we cannot measure RSSI and, therefore, cannot utilize the tuning algorithm. We manually set the capacitor states in a two-step process similar to the tuning algorithm. First, we fix the second-stage capacitors and manually tune the first stage for the best SI cancellation, then, we manually tune the second stage. Fig. 2.6(b) shows the SI carrier cancellation results for one- and two-stage tunable impedance networks. Results show that a single stage is insufficient to achieve 78 dB carrier cancellation, whereas the two-stage design meets the specification. Next, we measure offset cancellation by keeping

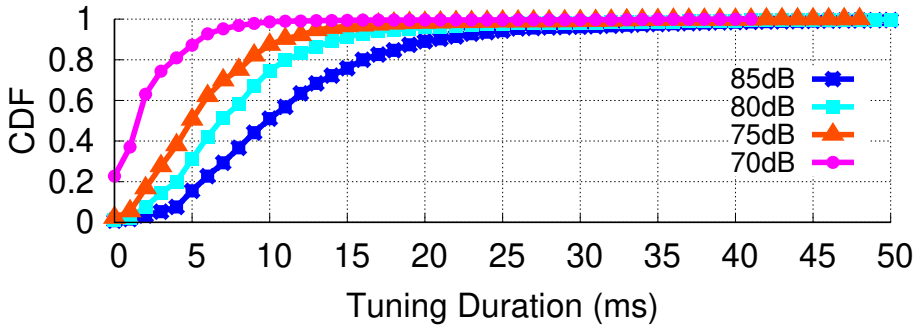

Figure 2.7: Tuning algorithm overhead measured over 10000 packets.

the same capacitor configuration and sweeping the carrier source between 905 - 925 MHz in 100 KHz frequency increments. Fig.2.6(c) shows the offset cancellation for different antenna impedances at 3 MHz offset. Our results show that we achieve our target of 46.5 dB offset cancellation for all antenna impedances.

2.6.2 Tuning Overhead

To measure the performance of our tuning algorithm, we place the FD LoRa Backscatter reader with the PIFA on a table in a typical office environment. We collect 10,000 packets from a tag placed 20 ft away over the course of 80 minutes with multiple people sitting nearby and walking in the vicinity of the system. We modify the target SI cancellation threshold in the tuning algorithm to 70, 75, 80, and 85 dB and run experiments to measure the time required for tuning. The tuning algorithm was able to achieve the target SI in 99% cases. We plot the CDF of tuning overhead for different cancellation thresholds in Fig. 2.7. As expected, the tuning duration increases with the target threshold. For a threshold of 80 dB, the average tuning duration is 8.3 ms, corresponding to an overhead of 2.7%. The RSSI measurements from the SX1276 chipset are noisy, and we take the mean over 8 readings for each tuning step, which is the key limitation. Each tuning step takes about 0.5 ms, dominated by the SPI transactions and settling time of the receiver. An RF power detector, which is beyond the scope of this work, can be used to provide faster feedback at the expense of increased cost.

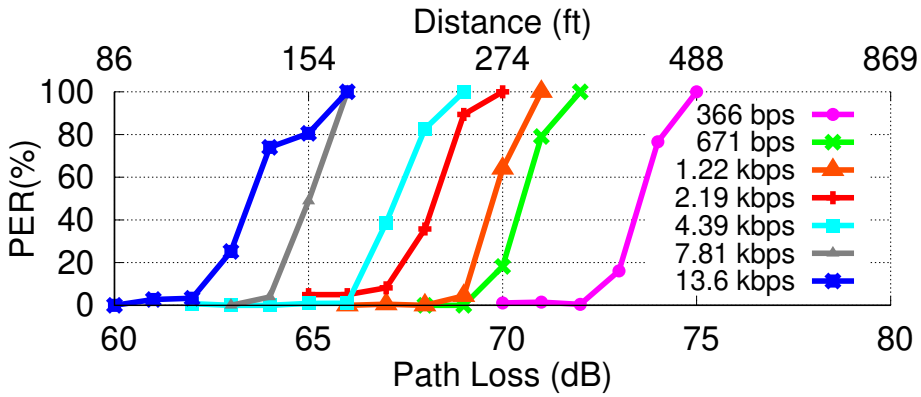

Figure 2.8: Receiver Sensitivity Analysis. We plot the PER as a function of path loss for different data rates.

2.6.3 Receiver Sensitivity Analysis

To evaluate the receive sensitivity of the FD LoRa Backscatter system without the effect of multi-path signal propagation, we create an equivalent wired setup. We use RF cables and a variable attenuator to connect the antenna port of the FD LoRa Backscatter reader to a LoRa backscatter tag. We vary the in-line attenuator to simulate path loss, corresponding to different operating distances between the reader and the tag. We start with an attenuator value at which we receive all packets and then slowly increase the attenuation until no packets are received. We configure the SF and BW parameters to cover a range of sensitivity and data rates.

Fig. 2.8 plots PER as a function of path loss in a wired setup for different data rates. Since sensitivity is inversely proportional to data rate, lower data rates can operate at higher path loss, which translates to longer operating distances. For a $PER \leq 10\%$, the expected LOS range at the lowest data-rate of 366 bps (SF=12, BW=250 KHz) is 340 ft, with the range decreasing successively for higher bit rates, down to 110 ft for 13.6 Kbps (SF=7, BW=500 KHz).

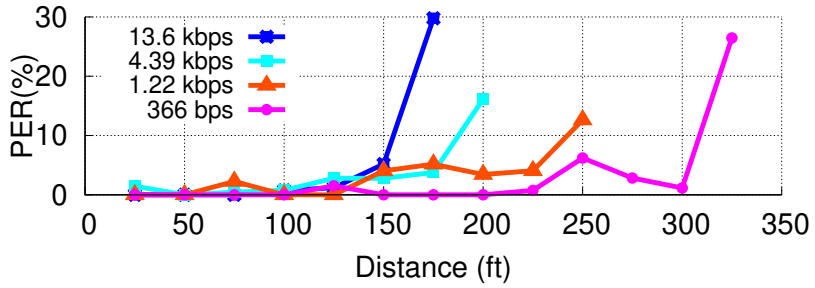

(a) PER vs Distance for various data-rates.

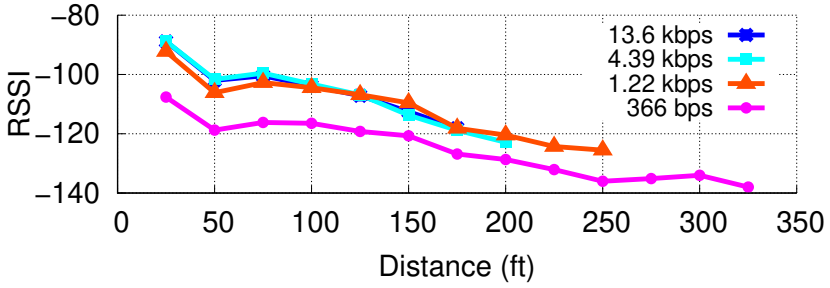

(b) RSSI vs Distance for various data-rates.

Figure 2.9: Line-of-Sight Wireless Tests. We move the backscatter tag away from the reader in line of sight.

2.6.4 Line-of-Sight (LOS) Wireless Testing

We deploy the FD LoRa Backscatter system in a nearby park to measure LOS performance. For best performance, we configure the reader as a base-station (see §2.5) by connecting an 8 dBiC circularly polarized patch antenna [49], placed on a 5 ft tall stand, to the antenna port and set transmit power to 30 dBm. We place the tag at the same height and move it away in 25 ft increments. Fig. 2.9 plots PER and RSSI as a function of distance for four different data rates. Our results show that, for $PER < 10\%$, at the lowest data rate, the system can operate at a distance of up to 300 ft with a reported RSSI of -134 dBm. For the highest data rate, the operating distance was 150 ft at -112 dBm RSSI.

A prior HD LoRa backscatter system reported a range of 475 m between the two ra-

dios [190]; this corresponds to a range of 780 ft for an FD system. Our FD system achieves a shorter range and this can be attributed to two factors. First, the HD system evaluation uses a -143 dBm sensitivity protocol at 45 bps versus the -134 dBm sensitivity at 366 bps used in this work. The 45 bps packets are 2.4 sec long, 6 $\times$ the FCC maximum channel dwell time (see §2.2.1). Additionally, the FD system uses a hybrid coupler architecture. This reduces cost, but incurs a 7 dB loss (see §2.5). So, in total, our link budget is reduced by 16 dB. This translates to a 2.5 $\times$ range reduction, close to the 300 ft range of our system.

2.6.5 Non-Line-of-Sight (NLOS) Wireless Tests

Next, we set up in a 100 ft $\times$ 40 ft office building to evaluate performance in a more realistic NLOS scenario. We place the base-station reader in one corner of the building and move the tag to ten locations to measure performance through cubicles,multiple concrete and glass walls, and down hallways. The floor plan of the building is shown in Fig.2.10(a). The blue star in the lower-right corner indicates the position of the FD reader, and the red dots indicate the different locations of the tag throughout the office space. We transmit 1,000 packets at each location, and a CDF of the aggregated RSSI data from the test is shown in Fig.2.10(b). We observed a median RSSI of -120 dBm and PER of less than 10% at all the locations demonstrating that the FD LoRa Backscatter system is fully operational in the office space with a coverage area of 4,000 ft^2.

2.6.6 Integration with Mobile Devices

Finally, we evaluate the performance of the mobile version (see §2.5) of the FD reader. We attach the mobile reader to the back of an iPhone 11 Pro, as shown in Fig. 2.11(a) and configure the reader to transmit at 4 dBm, 10 dBm, and 20 dBm to resemble the transmit power of mobile devices. We move a backscatter tag away from the reader in 5 ft increments until $PER > 10\%$. Fig. 2.11(b) plots the RSSI of the received packets as a function of distance. The plots show that at 4 dBm, the mobile reader operates up to 20 ft and the range increases beyond 50 ft (the length of the room and limit of our testing) for a transmit

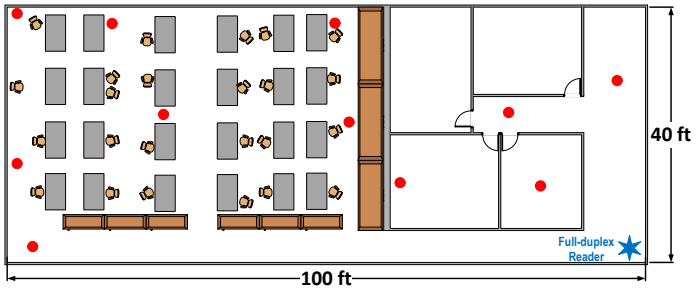

(a) Floor plan of the 4,000 ft^2 office space.

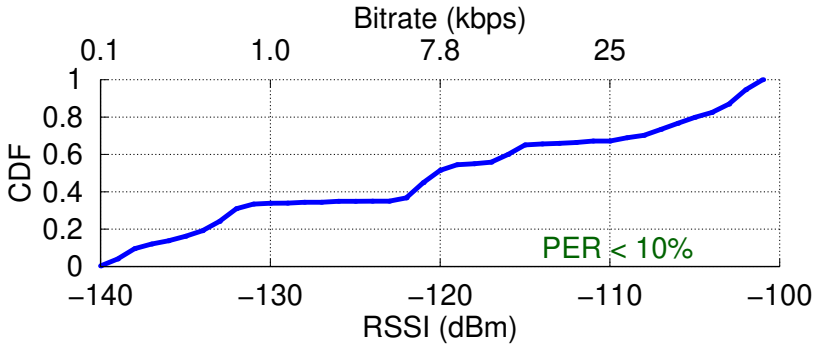

(b) RSSI of all measurements in the office space.

Figure 2.10: Non-Line-of-Sight Wireless Tests. We place the backscatter tag at 10 locations shown as red dots.

power of 20 dBm. These distances are sufficient for connecting peripheral, wearable, and medical devices to a smartphone using backscatter at extremely low cost, small size, and low power consumption. These experiments were done in an uncontrolled wireless environment and the variation in signal strength at different locations is due to multi-path effects, which is typical of practical wireless testing.

To demonstrate that our system can adapt to variations in environment and antenna impedance, we place the FD LoRa Backscatter enabled smartphone in a subject's pocket and set the transmit power to 4 dBm. We place a tag at the center of an 11 ft $\times$ 6 ft table, and the subject walks around the perimeter of the table, receiving more than 1,000 packets. The performance is reliable with PER $<$ 10%, which demonstrates the efficacy of our tuning

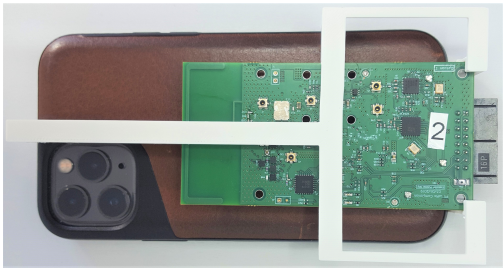

(a) FD LoRa Backscatter on the back of a smartphone.

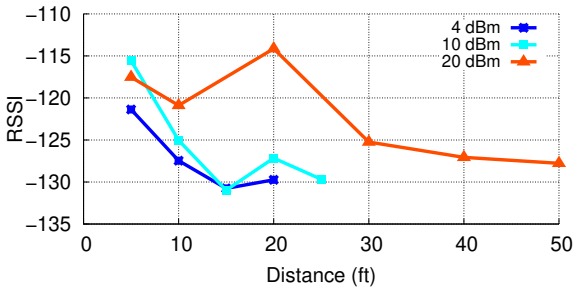

(b) RSSI vs Distance for line-of-sight testing in mobile configuration.

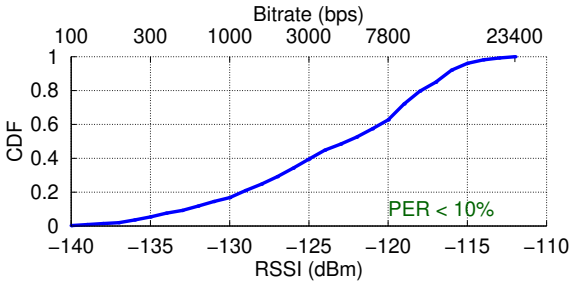

(c) Packet RSSI with the mobile reader in a user's pocket moving around a table.

Figure 2.11: Integration with Mobile Devices.

algorithm. Fig. 2.11(c) plots the CDF of RSSI for all the packets. The backscatter tag measures 2 in $\times$ $1\frac{1}{2}$ in, resembling the size of a pill bottle. This demonstrates that a mobile smartphone can use backscatter to communicate with a prescription pill bottle or insulin pen, allowing tracking of medication and drug delivery.

2.7 Applications

We demonstrate two applications for our FD system. First, we show how a mobile reader can collect data from a smart contact lens, a particularly challenging RF environment. Next, we demonstrate a precision agriculture application by mounting the reader to the bottom of a drone, which can be flown over farms and use backscatter to collect data from sensors distributed in a field. The use of a single reader coupled with a highly sensitive long-range backscatter protocol enables these applications, even in these challenging deployments.

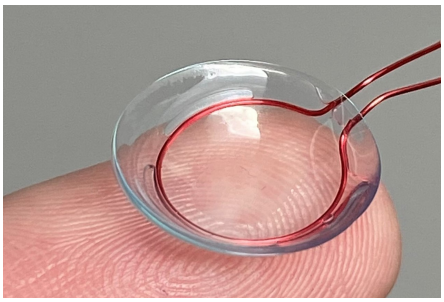

(a) Contact lens antenna prototype.

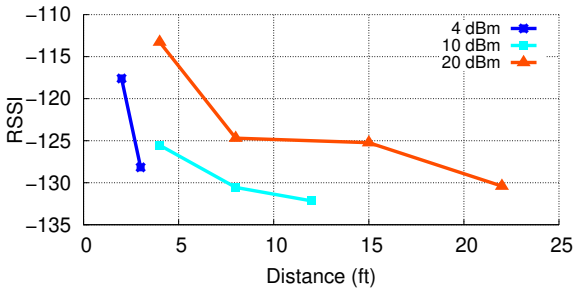

(b) RSSI vs Distance for different transmit powers.

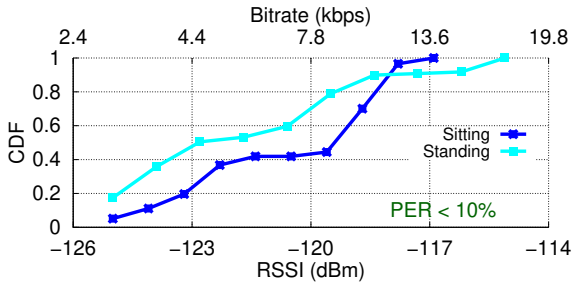

(c) RSSI when reader is inside a user's pocket.

Figure 2.12: A mobile FD LoRa Backscatter reader communicating with a contact lens prototype.

2.7.1 Contact Lens

We use the mobile FD LoRa Backscatter system mounted on the back of a smartphone to communicate with a backscatter tag equipped with a smart-contact-lens-form-factor antenna. We use the same backscatter endpoint as with other tests, but we cut off the original PIFA and replace it with a small loop antenna of 1 cm diameter made with 30 AWG enameled wire. The antenna is encapsulated in two contact lenses and filled with contact lens solution to simulate the RF environment of an eye-ball, as shown in Fig. 2.12(a). Due to its small size and the ionic environment of the contact solution, the loop antenna has an expected loss of 15 - 20 dB.

We place the smartphone on a table and configure the mobile reader to transmit at 4, 10, and 20 dBm and move the contact lens backscatter prototype away from the smartphone. Fig. 2.12(b) shows the RSSI as a function of distance for various transmit powers. We show that the mobile reader at 10 dBm and 20 dBm transmit power can communicate with the contact lens at distances of 12 ft and 22 ft respectively for PER $< 10\%$. Next, we put the mobile reader transmitting at 4 dBm in a 6 ft tall subject's pocket and hold the contact lens prototype near the subject's eye to simulate a realistic use case. Fig. 2.12(b) plots the CDF of the RSSI of decoded packets when the user was standing and sitting on a chair. The plot shows reliable performance with PER $< 10\%$ and a mean RSSI of -125 dBm. This demonstrates the feasibility of using backscatter to provide continuous connectivity between a user's phone and a smart contact lens. This RF-challenged application was made possible even at such a low transmit power due to the high receive sensitivity of the system.

2.7.2 Drone with an FD Backscatter Reader

Drones are extensively used for aerial surveillance in precision agriculture [200]. We demonstrate how one can augment a drone's functionality by adding a FD LoRa Backscatter reader to communicate with sensors distributed in a field using backscatter. We attach the mobile version of our reader to the bottom of a low-cost, commercially-available Parrot AR.Drone 2.0 quadcopter (<$80) [47], as shown in Fig.2.13(a). We power the reader from the drone's battery using a USB connector to demonstrate the ease of integrating our system. We set the transmit power to 20 dBm to reduce the burden on 7.5 Whr battery of the cheap drone. We place the tag on the ground simulating an agriculture sensor and fly the drone at a height of 60 ft. Due to practical challenges in accurately positioning the drone, we allow the drone to fly laterally during the test up to 50 ft from the center, which results in 80 ft maximum separation from the tag. This corresponds to an instantaneous coverage area of 7,850 ft^2. We collect more than 400 packets over 4 minutes with the drone flying around the coverage zone while keeping its altitude constant.

Fig.2.13(b) plots CDF of the RSSI of the packets received by the drone over the entire

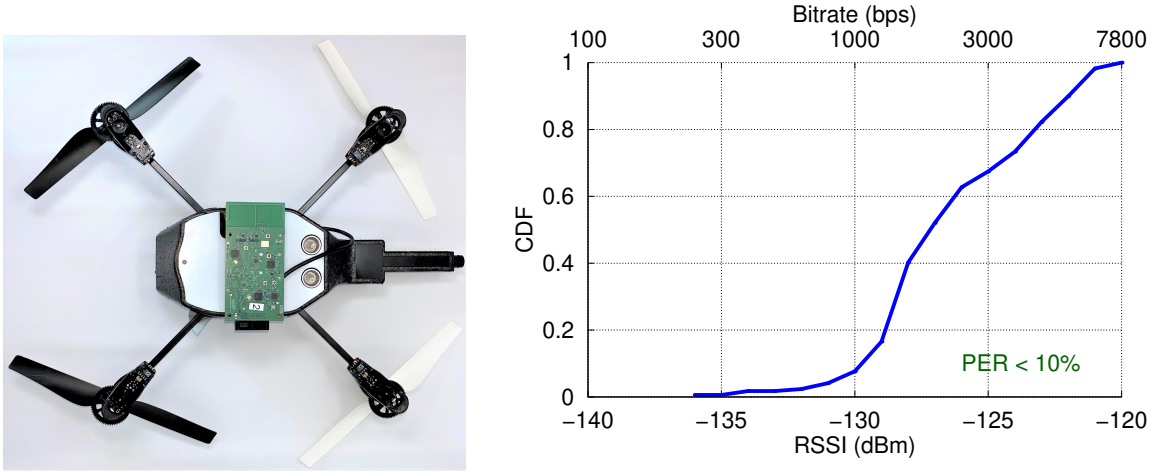

(a) Reader mounted on the drone.

(b) RSSI when drone is at 60 ft altitude.

Figure 2.13: Backscatter enabled Low-Cost Drone.

duration of the test for a $PER < 10\%$. With a minimum of -136 dBm and median of -128 dBm, this demonstrates good performance for the area tested. With a flight time of 15 min and a top speed of 11 m/s, our cheap drone could, in theory, cover an area greater than 60 acres on a single charge. With a more powerful drone with higher payload capacity and longer flight time, one could integrate a higher gain antenna and transmit at higher power. This would result in a greater instantaneous coverage area and, with longer flight time, could achieve many times greater coverage on a single charge.

2.8 Related Work

Our work is related to prior efforts in HD backscatter, FD backscatter, and in-band FD communication.

Half-Duplex Backscatter. Our work builds on recent efforts in developing backscatter solutions that are compatible with existing wireless standards such as Bluetooth [90, 108, 208, 119], WiFi [125, 108, 53, 213, 208, 209], Zigbee [141], and LoRa [190, 163] using half-duplex architectures. The backscatter endpoint is based on prior LoRa backscatter design [190], but

we take the next step of integrating the single-tone carrier source and LoRa receiver into a single device.

In addition to standards-compliant backscatter, proprietary-protocol communications [106, 215, 176, 177] (to improve data rates and throughput), applications such as wireless video streaming [180, 113], indoor localization [159, 149, 148], and human activity recognition [178, 54, 66] have been realized with HD deployments. The techniques presented in this work can be extended to build an FD version of these systems.

Full-Duplex Backscatter. A BLE monostatic/FD backscatter system was introduced in [88] that uses a 20 dB coupler, phase shifter, and variable attenuator for SI cancellation. However, due to additional losses in the coupler and limited cancellation depth, the communication range was limited to 3 m, even with 33 dBm of output power. In [60], an FD backscatter system using an SDR platform with analog and digital cancellation was introduced where WiFi packets are used as the carrier and the tag backscatters proprietary BPSK, QPSK, and 16-PSK modulated packets which were decoded by the SDR up to a distance of 7 m. Due to the wide-band nature of WiFi carrier signals, [60] needs wide-band SI cancellation. A circulator and a 10 cm $\times$ 10 cm custom PCB with 16 variable-gain delay lines are added to the SDR platform for wide-band analog cancellation, increasing both the solution cost and size. In contrast, the FD LoRa Backscatter system uses commodity LoRa radios and passive components for cancellation and can receive standard LoRa packets up to a distance of 300 ft.

RFID readers are also full-duplex devices that transmit a single-tone carrier and receive backscattered packets from RFID tags. However, EPC Gen2 readers are bulky, expensive [34, 43], and cannot compete with economies of scale of standard protocols. The operating range of passive RFID readers is determined by the power-harvesting sensitivity, not by the backscatter communication link. RFID readers operate at relatively short distances, even if the tag is powered from an alternative energy source [115], due to poor receive sensitivity (-90 dBm) [43, 34]. In contrast, our FD LoRa Backscatter system achieves much longer operating distances at significantly lower cost by leveraging a highly sensitive commodity

LoRa receiver, cheap passive components, and a microcontroller for deep SI cancellation. Low-cost RFID readers based on directional couplers have also been investigated [114, 123], but they suffer from high Rx insertion loss and lower SI cancellation depth, which reduces range. In [151], a full-duplex drone relay is presented to extend the range of a fixed RFID reader. The topology requires an additional relay on a drone to extend the fixed RFID reader range to 50 m. In contrast, our FD reader can be mounted on a flying drone to cover a significantly larger area.

In-Band Full-Duplex Radios. In-band full-duplex (IBFD) radios simultaneously transmit and receive at the same frequency. Recent works have used a combination of isolation, analog cancellation, and digital cancellation techniques to suppress SI below the receiver noise floor [62, 133, 86, 69].

Existing isolation techniques use two or more physically-separated antennas [92, 86, 85, 135], discrete circulators [62, 133, 211, 126, 69], integrated circulators [172, 81], or hybrid junctions [142, 75] to isolate transmitter and receiver. The use of multiple antennas increases form factor while achieving limited isolation. Discrete circulators [17] are bulky and expensive. While recent advances in integrated circulators [172, 81] are promising, these devices are unable to handle the 30 dBm output-power requirement. Hybrid junctions, realized using couplers [114, 123] (such as the 3 dB coupler used in this work) or electrical balance duplexers (EBD) [142, 75], incur a loss, but result in small-form-factor and inexpensive solutions. However, existing solutions with COTS components cannot achieve 78 dB of SI cancellation [114, 88, 123], whereas our proposed two-stage impedance tuning network can be used to achieve this deep cancellation required for building a cheap, low-complexity, long-range FD reader. Furthermore, [142, 75] show a path towards further reducing the cost and size at high volumes by integrating the hybrid junction in silicon.

Analog feed-forward cancellers can be combined with isolation techniques to enhance SI cancellation depth and bandwidth. Various feed-forward PCB and ASIC implementations based on vector modulation [64], finite impulse response filters [62, 133, 211, 75], frequency domain equalization based RF filters [69], N-path filters [217], and Hilbert transform equal-

Table 2.3: Comparison of State of the Art Analog SI Cancellation Techniques

Ref.	Cancellation Technique	TX Signal	RX Signal	Analog Can.	TX Power	Active Comp.[+]	Size	Cost
[86]	Multiple antenna + auxiliary can. path	WiFi Packet	WiFi Packet	65 dB	8 dBm	Yes	37 cm Ant. Separation	High
[69]	Circulator + 2 tap freq. domain equalization	WiFi Packet	WiFi Packet	52 dB	10 dBm	Yes	1.5 × 4.0 cm^2	High
[133]	Circulator + 3 complex-tap analog FIR filter	WiFi Packet	WiFi Packet	68 dB	8 dBm	Yes	N.A.	High
[75]	EBD + Double RF adaptive filter	General	General	72 dB	12 dBm	Yes	Custom ASIC[*]	
[172]	Magnetic-free N-path filter-based Circulator	General	General	40 dB	8 dBm	No	Custom ASIC[*]	
[142]	EBD + passive tuning network	General	General	75 dB	27 dBm	No	Custom ASIC[*]	
[60]	Circulator + 16 tap analog FIR filter	WiFi Packet	WiFi Backscatter	60 dB	20 dBm	No	10 × 10 cm^2	High
[88]	20dB Coupler + Active tuning network	CW	BLE Backscatter	50 dB	33 dBm	Yes	N.A.	High
[124]	10dB Coupler + Atten. + passive tuning network	CW	EPC Gen 2	60 dB	26 dBm	No	2.7 × 2.0 cm^2	Low
This Work	Hybrid Coupler + passive tuning network	CW	LoRa Backscatter	78 dB	30 dBm	No	2.5 × 0.8 cm^2	Low

[+] Active components include phase shifters, vector modulators, amplifiers and transconductance amplifiers which can contribute additional noise.

[*] Custom ASICs are incompatible with COTS transceivers and are only viable and cost-efficient at scale.

ization [183] have been proposed. However, these techniques require additional active circuitry, which has a limited power-handling capability and generates noise that increases the receiver noise floor [74]. Furthermore, COTS phase shifters [44] and vector modulators [42] are bulky and expensive, which substantially increases cost, complexity, and form factor. In

this work, we utilize the two-stage tunable impedance network architecture to achieve the required 78 dB cancellation depth. Since the transmitter carrier signal is only single-tone, we do not need the feed-forward paths to improve the bandwidth.

In Table 2.3, we summarize the state-of-the-art techniques used for analog SI cancellation and compare them with our approach in terms of cancellation depth, transmit power-handling capability, size, and cost.

Finally, digital cancellers are often used to further suppress the SI below the receiver noise floor [62, 132, 127, 69] using both linear and non-linear cancellation techniques [118]. Digital cancellation requires access to baseband IQ samples. This function is not available on commodity radio chipsets and is typically implemented on SDRs [62, 186, 69, 55], FPGAs [196], or DSPs [59], which are prohibitively expensive. Instead, since our interference is a single-tone at a frequency offset from the receive channel, we leverage the inherent baseband filtering capabilities of the commodity receiver to suppress the SI at the offset frequency.

2.9 Conclusion

We present the first low-cost, long-range, small-form-factor Full-Duplex LoRa Backscatter design. We use a single-antenna, hybrid-coupler-based architecture and introduce a novel two-stage tunable impedance network to meet the stringent SI-cancellation requirements using only passive components and a microcontroller. We build hardware using COTS components and prototype proof-of-concept applications for a smart contact lens and backscatter enabled drone.

Chapter 3

RELACKS: RELIABLE BACKSCATTER COMMUNICATION IN INDOOR ENVIRONMENTS

3.1 Introduction

The recent wave of wirelessly connected devices in homes provides an excellent opportunity to bring low-cost connectivity to billions of objects around us. For example, the embedded transceivers in the dishwasher, oven stove, and range hood could collaborate and form backscatter links to communicate with smaller or non-plugged objects around the kitchen -such as a cooking pot, a kitchen knife, or cabinets- equipped with low-cost backscatter tags. Fig. 3.1 depicts this vision where the backscatter communication helps to realize new applications such as reading the temperature inside the cooking pot, detecting human interactions with different objects around the kitchen, and many more. We need to satisfy two main requirements to realize this vision. First, the backscatter communication should use the same transceiver(TRX) as the embedded radio to minimize the additional cost. Second, the backscatter system should reliably cover every point in the room by overcoming frequency and spatial dependent fading in indoor environments.

Previous works in backscatter communication have shown backscatter systems with physical layer compatibility to current wireless standards and measured the maximum communication range and throughputs of their implementation. However, methods and techniques to evaluate and improve bistatic backscatter systems reliability, especially in dynamic multipath rich indoor environments with moving objects, is less investigated. Backscatter systems suffer from high propagation loss due to two consecutive propagations and have to operate on narrower link budget margin compare to active radios. Furthermore, increasing RF excitation power does not necessarily improve the communication reliability of bistatic backscatter

Figure 3.1: Our vision for future connected indoor environments, where plugged-in devices use the same embedded radios to connect to the home network and to enable backscatter communication with the smaller objects [48].

systems, since it increases the backscatter signal strength and excitation interference to the receiver at the same time. Thus, selecting proper communication parameters is vital for achieving reliable backscatter communication.

One of the challenges in addressing multipath fading in a bistatic backscatter system arises from the distributed nature of these systems. The transceiver that provides the excitation signal can not detect whether a backscatter packet is formed and received or not. Only the receiver can determine the link quality based on the strength of the reflected signal. To solve this issue, we present *Relacks*, a closed-loop system where the link quality metrics are shared between the two base units and used to avoid low-quality links, as shown in Fig. 3.2. We achieve high reliability by exploiting frequency, antenna, and wake-up source diversity in real-time with the optimum communication parameters selected based on the history of the previous communications.

To investigate the effects of closed-loop parameter selection on the backscatter link performance, we design and prototype a backscatter system that uses BLE backscatter nodes to communicate with commercial off the shelf BLE transceivers. Backscatter tags are capable of

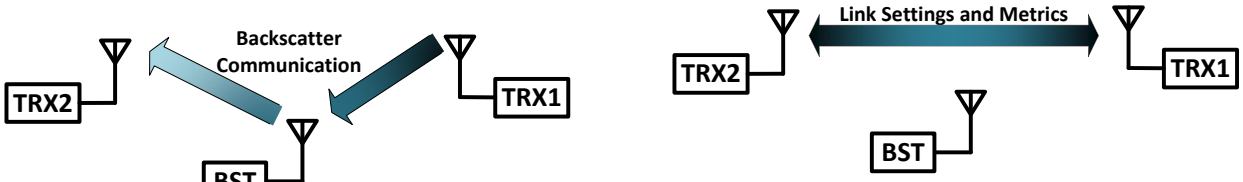

(a) The TRX boards follow the defined settings to communicate with the tag.

(b) The TRX boards share link settings and metrics to avoid using low quality links for future backscatter communications.

Figure 3.2: Closed-loop backscatter system. The transceivers share link settings and metrics after the backscatter communication to improve link reliability.

generating BLE v5.0 coded PHY packets to achieve a better sensitivity and communication range. The tags use the backscatter link to transmit data to base units and are equipped with ultra-low-power wake-up receivers to receive command and data from the base units. BLE TRX base units are designed with off the shelf components and can generate wake up patterns to activate and communicate with the tags. We test the *Relacks* backscatter communication system in multiple indoor environments. The results show that the system achieves a uniform coverage for any point in several indoor environments with areas up to 60 m^2 while the excitation power is 18 dBm. We evaluate the system not only when the tag lies between the two TRXs, but also when the tag is placed on the corners of an area, which are the worst-case arrangement for covering a room.

The main technical contributions of this work are:

1) We propose a closed-loop backscatter system, where link parameters are shared between the two TRXs to improve link reliability. We show the effect of frequency, antenna, and wake up source diversity on the backscatter link reliability and implement a real-time algorithm to enhance communication reliability by using these diversities effectively.

2) We prototype a complete backscatter system with backscatter tags and BLE transceiver units and use them in our evaluations. We design tags with backscatter packets compatible with BLE 5.0 coded and 1M PHYs for uplink and ultra-low-power OOK based packets for downlink. We design transceiver units with commercial BLE transceivers, each one is capable

of communicating with the tag, generating RF excitation signal, and receiving backscatter packets.

3) We evaluate the system performance intensively at multiple locations in several indoor environments. Also, we characterize the effect of several variables such as tag antenna orientation and different human interactions on the system performance.

3.2 Backscatter System Design

The first step in designing a backscatter system is to select the communication standard. We target smart home applications, and we would like to use the same transceiver used in connecting to the smart home network for communicating with backscatter tags. Several standards, such as Zigbee, Z-Wave, Thread, BLE, and WiFi, are competing for market share with no one dominating the market at the moment [154, 79]. Bluetooth is a major contender in the battle for smart home protocol dominance with more than 4 Billion devices shipped in 2019 [27], high compatibility between devices, and availability in smartphones. Bluetooth v5.0 has introduced improved mesh capabilities, long-range, and high data rate modes to address some of the shortcomings of the previous versions. While we have chosen to use BLE for this implementation, the techniques that we describe in section 3.3 can be applied to any backscatter system to improve the reliability.

To increase the communication range of a wireless system, one can increase transmit power. Increasing the RF source power increases the interference to other users and limits the overall throughput. By limiting the scope of the backscatter communication to a room, we do not need to overcome the signal loss through the walls, and we can lower the RF source excitation power to minimize the interference to the other wireless systems in the area. Since floor plan and room sizes of each house can be very different [189, 33], we target to cover a 50 m^2 area with the backscatter system in this work. The coverage would be enough for most bedrooms, bathrooms, laundry rooms, kitchens, dining rooms, and living rooms in homes less than 3000 ft^2 (278 m^2) [87].

3.2.1 Bluetooth Low Energy v5.0 Primer

BLE v5.0 standard defines two modulation schemes, a mandatory 1MSym/s and an optional 2MSym/s. Although the 2Msym/s achieves a higher data rate, we stick to the mandatory one since the data rate is enough for most IoT applications, and it consumes less power due to operating with a lower clock rate. The 1Msym/s modulation scheme uses a binary frequency modulation, where a binary '1' represented by a positive frequency deviation and a binary '0' represented by a negative frequency deviation. The minimum frequency deviation shall never be less than 185 KHz at 1Msym/s. The maximum output power level for BLE v5.0 devices is 20 dBm [13].

The 1MSym/s modulation supports two PHYs, LE 1M uncoded PHY with 1Mbps data rate, and LE coded with 125kbps or 500kbps data rates. While both PHYs perform CRC generation and whitening on the incoming bitstream, the coded PHY takes two additional steps of FEC encoding and pattern mapping. FEC encoding uses a non-systematic, non-recursive, rate 1/2 code with constraint length equal to 4 to map each incoming bit to two bits. Pattern mapper is only used in the 125kbps coded PHY and converts each output bit of the FEC encoder to four bits, '0011' for zeros and '1100' for ones [13]. By performing these additional coding steps, the coded PHY receivers achieve lower sensitivity (i.e., longer communication range) and better interference handling at the expense of lower data rates. In this work, we focus on the 125 Kbps coded PHY and 1Mbps uncoded PHY.

3.2.2 BLE Tag

We design the tag to be a complete transceiver with a BLE v5.0 compatible backscatter uplink and an ultra-low-power amplitude modulation based downlink. The uplink and downlink share one antenna using time-division multiplexing. In receive mode, the antenna is connected to the receiver through a SKY13317 three-to-one RF switch. Once a wake-up request is detected, the receiver enables the controller. The controller is a low power MSP430FR2311 microcontroller (MCU), and it controls the backscatter uplink. In transmit mode, the an-

tenna switches between the other two ports of the RF switch, where one connected to GND through a 47pF capacitor and the other one left open. The block diagram of the tag and the fabricated prototype board are shown in Fig. 3.3(a) and Fig. 3.3(c) respectively.

BLE5 Compatible Backscatter. The backscatter uplink includes an ICE40UP low power FPGA and a 12 MHz SiT8021 MEMS oscillator. The FPGA and the oscillator remain in an idle mode until the controller enables them. Once enabled, the FPGA receives the data from the MCU and performs all the packet processing steps required for BLE packet generation in coded or uncoded PHYs. The bit generation logic operates at a 1MHz clock rate and outputs one bit each microsecond. The 1MHz clock is generated inside FPGA by dividing the input clock to 12.

To mitigate the RF source interference effect on the receiver, we should modulate the backscatter data with a subcarrier to shift the tag output spectrum respect to the RF source. Considering the 185 KHz minimum frequency deviation in the BLE standard, we need to generate two frequencies that are at least 370 KHz apart. Higher subcarrier frequency increases the frequency separation between the RF source and backscatter packet, but it also increases the tag power consumption. In this work, we use a 12 MHz reference clock and the lower sideband of the reflected spectrum. Turning the RF switches on and off at 4 MHz and 3MHz represents bits '0' and '1' respectively, which means a 3.5 MHz subcarrier frequency modulation and 500 KHz frequency deviation. The two frequencies are generated from the 12 MHz reference clock and satisfy the BLE standard requirements. Since the BLE standard specifies receiver interference performance for adjacent interferers up to 3 MHz [13], increasing the subcarrier frequency beyond 3 MHz does not provide any guaranteed performance boost. Furthermore, the selected frequencies are integer multiples of the bit rate, which eliminates any undesired glitch in switching between consecutive bits.

Wake up Receiver. Despite the recent advances in the low power wake up radio architectures [164, 201, 153, 116], there are few commercial-off-the-shelf components available for this task at the moment. We use AS3933 in this work, which is a low-power, low-frequency receiver IC with wake-up pattern recognition. The receiver consumes only 2.3 µA

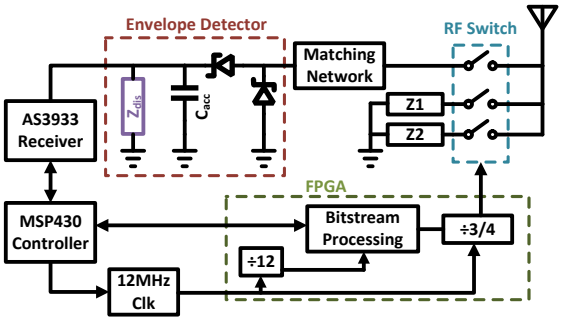

(a) BLE tag block diagram.

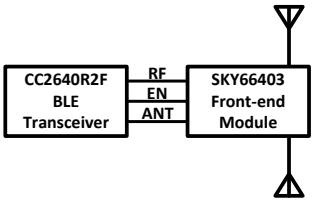

(b) BLE transceiver units block diagram.

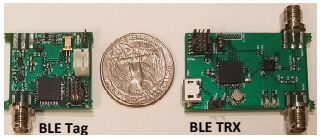

(c) Prototype tag and TRX boards.

Figure 3.3: BLE tag and BLE transceiver prototypes.

in listening mode, which is essential to preserve energy in power harvesting systems or enable multi-year operation on a single battery in battery powered-systems. Each tag is individually addressable using a 16 bit ID. The AS3933 reports the received signal strength (RSS) after each wake up as a number between 0 and 31, and we later use this feature for enhancing system reliability in section 3.3.

The receiver operates at 125 KHz with a Manchester coded 4.16 Kbps data rate. In Manchester coding, '01' and '10' bit sequences represent symbols '0' and '1' respectively. The incoming RF signal at 2.4 GHz is amplitude modulated with a 125 KHz waveform, which itself is modulated with a Manchester coded 4.16 Kbps data stream. We use a passive envelope detector with SMS7621 RF diodes after the matching network to extract the 125 KHz waveform from the incoming RF signal. The envelope detector circuit diagram is shown in Fig. 3.3(a). In the presence of the RF signal, the charge accumulates on capacitor C_{acc} and the output voltage rises. In the absence of the RF signal, the capacitor is discharged through Z_{dis} and the output voltage falls. Each charge and discharge cycle should take 8 us to create a 125 KHz waveform.

There is a trade-off in selecting the Z_{dis} resistance. For strong RF inputs, the resistor should be small enough to discharge the capacitor in 4us. For weak inputs, the resistor should be large enough to allow the output voltage to rise during the 4us charge cycle. To solve this issue, we design a non-linear voltage-dependent resistance by combing diodes and

resistors. We use a 10M ohm resistor, a schotkey diode (V_{on} = 0.2 V) in series with a 10K ohm resistor, and a general-purpose diode (V_{on} = 0.7 V) in series with a 1K ohm resistor to form the discharge network. At lower capacitor voltages, the diodes are off, and only the largest resistor is discharging the capacitor. For stronger inputs, the equivalent resistance decreases as the capacitor voltage rises, and the diodes turn on. We successfully test the receiver with input powers between 10 dBm and -43 dBm.

Power Consumption To measure the tag power consumption in backscatter mode, we set the tag to generate and send backscatter packets continuously. The total measured power consumption is 1.6 mW when the tag transmits 520 coded PHY packets per second. (Each packet is 1.44 millisecond long.) The 12 MHz oscillator is kept on constantly during the test and consumes 627 µW from a 2.5V supply. The FPGA core consumes 192 µW from a 1.2 V supply to generate BLE packets. The FPGA I/Os consume 620 µW from a 2.5 V supply to drive the RF switches, and the MCU consumes an average 50 µW from a 2.5 V supply to wake up between packets and transfer next packet data to the FPGA. The power consumption in digital circuits is proportional to CfV_{dd}^2 where C is the load capacitance, f is the frequency of the operation, and V_{dd} is the supply voltage. The power consumption of the tag in backscatter mode is dominated by the 12 MHz oscillator and RF switches drive since high-frequency signals are routed on the printed circuit board from one chip to another and experience a large pad and parasitic capacitance. In order to achieve the true low power capabilities of the backscatter communication, all the blocks must be integrated inside one IC to minimize the operating voltage and load capacitance.

IC Design We simulate our BLE backscatter tag design in the TSMC 65nm LP CMOS process using industry-standard EDA tools. Our simulated IC receives payload data and BLE PHY setting and generates a BLE packet by following the packet processing steps as described in 3.2.1. We use the Design Compiler by Synopsis to convert the Verilog code implemented on the FPGA to transistor-level implementation. We use RF transistors to implement backscatter switches. Our backscatter tag baseband consumes 22 µW from a 1.0 V supply to generate BLE packets. We need a 12 MHz reference clock in this design. [125]

simulates a ring oscillator based PLL that consume 5.6 µW to generate an 11 MHz clock. However, practical oscillators require additional circuitry to ensure proper operation over process, voltage, and temperature variation. [91] prototypes a 10 MHz oscillator in 65nm, which consumes 23.6 µW in steady-state operation using precisely timed energy injection technique. We estimate a practical 12 MHz oscillator with the same technique consumes 28 µW, which brings the total backscatter tag power consumption to 50 µW. This power consumption is low enough to be harvested from a variety of sources inside a building [212].

3.2.3 BLE Transceivers

We use commercial-off-the-shelf BLE transceivers in the TRX boards to generate the RF excitation signal or receive packets in backscatter communication. The boards are symmetrical and have both transmit and receive functionalities. The goal is to use the same transceivers to connect to the home network and support backscatter communication, with minimum added components.

Based on the communication protocol and target coverage area, we can calculate the required RF excitation power. Equation 3.1 expresses the received power at the receiver antenna port in backscatter communication.

$$P_{RX} = P_{TX} + G_{TX} + 20Log(\frac{\lambda}{4\pi d_1}) + CG_{tag} + 2G_{tag} + 20Log(\frac{\lambda}{4\pi d_2}) + G_{RX} - mp_{tx-tag} - mp_{tag-rx} \tag{3.1}$$

where P_{RX} is the received power at receiver antenna, P_{TX} is the transmitted power at the RF source, $G_{TX}, G_{tag}, and G_{RX}$ are the RF source, tag, and receiver antenna gains respectively, CG_{tag} is the tag conversion gain, λ is the signal wavelength, d_1 and d_2 are the distance between the tag and two TRXs, and mp_{tx-tag} and mp_{tag-rx} are the multipath loss between TRX1-tag and tag-TRX2 respectively.

In this work, we use CC2640R2F BLE transceivers with -103 dBm sensitivity for BLE coded PHY. We assume 0 dBi antenna gain for RF source, tag, and receiver. Tag conversion gain is measured as -4 dB,-3 dB due to dividing the incident power in upper and lower

frequency sidebands and an additional 1 dB loss through the RF switch. λ is 0.123 meters at 2.440 GHz. We would like to cover $50m^2$, so $d_1 \times d_2$ is equal to 50. By substituting these numbers in equation 3.1, while assuming no multipath loss, the minimum required RF source power is 15.3 dBm. Since this output power is beyond the maximum output power of the selected BLE transceiver, we use the SKY66403 BLE front end module to amplify the BLE TRX output power. The front end module supports two antennas, which we discuss how it can be used to improve link reliability in section 3.3. The front end module requires eight passive capacitors, and the total added cost is less than $1.5 for each TRX board. The TRX board consumes 12 mA from a 3V supply in receive mode and 90 mA in transmit mode when the RF output power is 18 dBm.

The AS3933 receiver uses amplitude modulation, but the selected transceiver only supports frequency modulation. To generate amplitude modulated waveform with the TRX boards, we turn the front end module power amplifier on and off. We use the CC2640R2F SPI interface to control the power amplifier in order to guarantee accurate timing in generating the 125 KHz waveform. The BLE transceiver also selects which antenna must be activated. The BLE TRX board block diagram, and the prototype BLE TRX board are shown in Fig. 3.3(b) and Fig. 3.3(c) respectively.

3.3 Improving Backscatter Reliability

Active radio links typically enjoy much higher link budget margins compared to the backscatter ones. To better understand this difference, we simulate and compare the received signal strength for an active and a backscatter wireless link using the free space signal propagation model. Fig. 3.4(a) shows the received signal strength when the transmitter is placed on the contour lines for an active transmitter with 0 dBm output power. If we assume a BLE receiver with better than -95 dBm sensitivity [19, 26] and a transmitter 50 meters away from the receiver, the received signal strength calculated by the free space path loss model is 21 dB above the receiver sensitivity. BLE is known as a short-range standard with a practical range of 10-50 meters, so the additional margin makes the system more reliable against frequency-

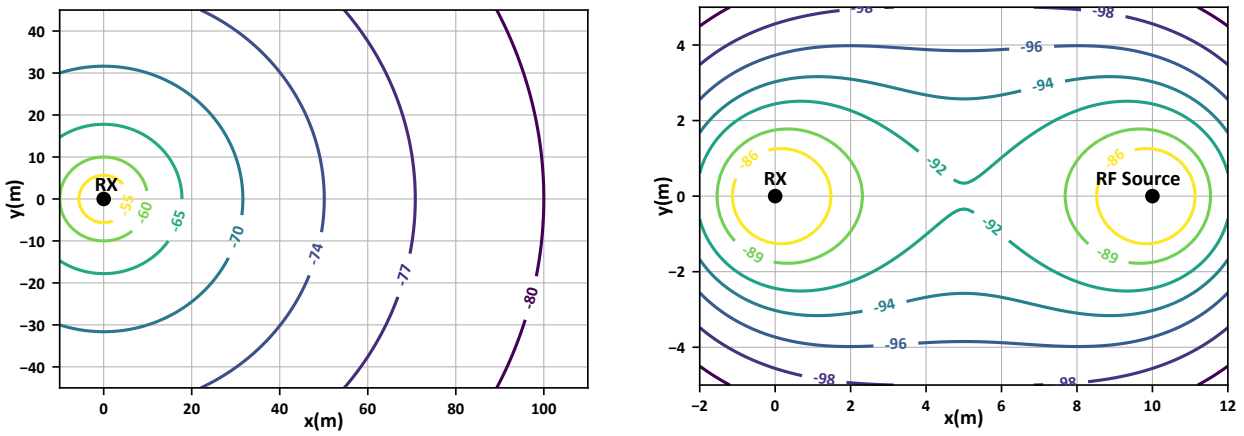

(a) Active link with a 0 dBm active transmitter.

(b) Backscatter link with 20 dBm carrier source power and 4 dB loss in tag.

Figure 3.4: Comparing received signal strength for an active link and a backscatter link based on the free space path loss model. The backscatter link has to operate on a much narrower margin to receiver sensitivity.

selective multipath fading and non-line-of-sight scenarios. Fig. 3.4(b) shows the received signal strength when the backscatter tag is placed on the contour lines based on equation 3.1 where RF excitation source is placed 10 meters away from the receiver, $P_{TX} = 20$ dBm, $CG_{tag} = -4$ dB, all the antennas have 0 dBi gain, and 0 dB multipath loss is assumed. The simulation shows that even with 100 times higher transmit power and five times shorter distance between the RF source and receiver, the backscatter signal power at the receiver is substantially lower than the active radio for most of the points in the environment. We use free space models with no multipath fading for these simulations. However, the propagation from RF source to tag and tag to RX might also experience fading in real scenarios, which further attenuates the received signal power. Thus, it is vitally important to minimize propagation losses to achieve reliable backscatter communication.

Previous studies have looked at the effect of multipath in indoor environments and methods to overcome it for active radios [193, 76, 95, 136, 128, 102, 63, 78, 188]. Multipath fading is frequency- and spatial-selective; for a specific point in the environment, the multipath loss

varies in different frequencies. Similarly, for a specific frequency, the loss varies at different points. Thus, we can use frequency and spatial diversity to minimize the multipath effect.

The backscatter system that we described in section 3.2 operates over 2.4 GHz ISM band with 80 MHz bandwidth, and each TRX board has two antennas. So the question is how to select the frequency and antennas to avoid high loss channels. Assuming 2 MHz frequency spacing between channels similar to the BLE standard, there are 38 frequency options (RF source and receiver frequency both have to be between 2402 MHz and 2480 MHz, and they are 3.5 MHz apart) and four antenna options. Also, we need to select which device is going to wake up the tag before the start of backscatter communication. We call each set of parameters that has to be fixed before the communication a *configuration*. Thus, we have 304 possible configurations in this system.

To gain a better understanding of the channel variation in a backscatter system, we perform the following experiment: We place two TRX boards on two sides of a 6.4 m $\times$ 10.3 m room, 9.4 m away from each other, and place the tag on 14 different points inside the room as shown in Fig. 3.5(a). At each point, we transmit 50 coded PHY backscatter packets with every possible configuration and calculate the backscatter success rate by dividing the ratio of successfully received backscatter packets to 50. The success rate heatmap plots are shown in Fig. 3.5(b) for each point where each square shows the success rate for one specific configuration. A brighter square means that the channel specified by that configuration has a better quality. The average plot in the bottom right corner shows the average success rate for each configuration at the 14 measured points. It is more uniform than any of the individual heat maps, which highlights the fact that each configuration might have good or poor quality in different points, and there is no single configuration that achieves a high success rate at all the locations.

Frequency Diversity. The frequency diversity is the most important source of diversity that we can exploit to achieve higher reliability. Each row on the heatmaps in Fig. 3.5(b) demonstrates the effect of frequency diversity while the other parameters are fixed. On each row, some frequencies are entirely dark, which means they experience a high loss, and no

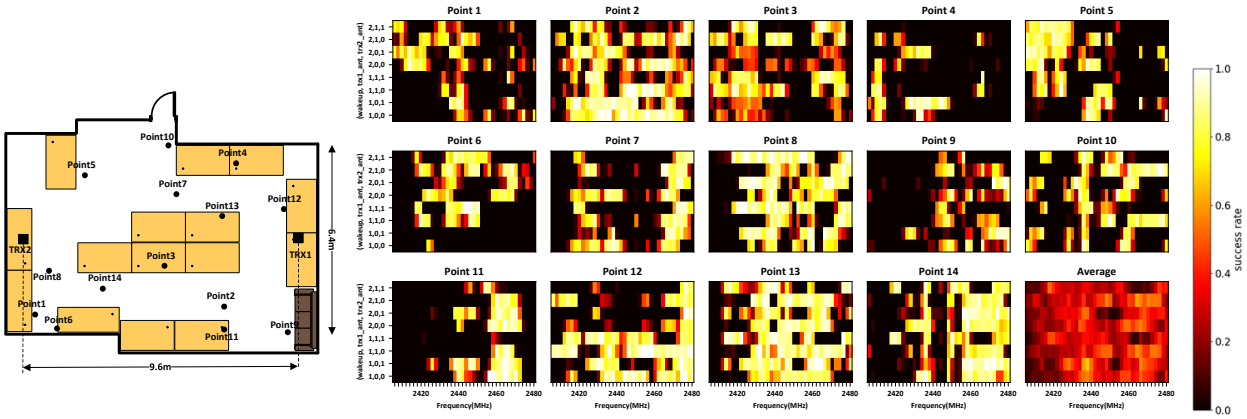

(a) Test environment.

(b) Success rate variation by using different configurations (frequency, antenna, and wake-up source) at different points.

Figure 3.5: Diversity effect on backscatter communication success rate.

packet is received at those frequencies. On the other hand, some frequencies are bright, which means most of the packets are successfully received at those frequencies. The bright and dark squares are packed together in most cases. In other words, although multipath fading is frequency selective, it changes slowly as the frequency changes. The average success rate over the 14 points shown in Fig. 3.5 is 30.9% with random configuration selection, but it increases to 91.9% by selecting the best frequency in each case.

Antenna Diversity. Antenna diversity is another way to improve the reliability of the communication link. In these experiments, we use omnidirectional dipole antennas with -0.6dBi average gain [23], and the two antennas on each transceiver are fixed 8 cm apart. The channel variation over antenna changes from point to point; for example, points 4, 6, and 7 show higher channel variations compared to points 12, 13, and 14. The importance of antenna diversity is highlighted for points 4 and 6, where one antenna shows poor quality links (TRX1 antenna 1 for point 4, TRX1 antenna 0 for point 6). In contrast, the other antenna has a high success rate over some frequencies. The average success rate over the 14 points further increases from 91.9% to 95.7% by choosing the best frequency and antenna combination.

Wake up Diversity. We have to specify one of the transceivers to wake-up the tag since they will interfere with each other if they both transmit the wake-up pattern. Ideally, we would like the closer transceiver to do the job, but we do not have the tag location information. The effect of wake-up source selection on overall performance is more evident when the tag is closer to one of the transceivers, such as points 4 and 12, where the TRX1 shows a clear advantage for wake up over TRX2. The average success rate over the 14 points increases from 95.7% to 99.2% by choosing the best frequency, antenna, and wake up source.

3.3.1 Closed-loop Configuration Selection System

In this section, we explain the closed-loop control system that selects a configuration for each backscatter communication. Our system includes one central controller, two TRX boards, and one or several backscatter tags. Each tag has a unique 16 bit ID.

The closed-loop process is shown in Fig. 3.6. The central controller is a laptop or a single-board computer that can run python scripts. It is connected to one of the TRXs through the UART interface. We name the TRX connected to the controller receiver and the other TRX transmitter. The controller sends a communication request to the receiver. The communication request sets the tag ID, frequency, each TRX antenna, and the wake-up source. Upon the reception of this request, the receiver sends an active BLE packet to the transmitter and shares this information. This packet also helps to maintain time synchronization between the two TRX boards through the rest of the operation. Next, the TRX board responsible for wake-up generates and transmits the wake-up pattern for the specified tag ID, while the other TRX waits. Once the wake-up is transmitted, the backscatter phase begins.

In the backscatter phase, the transmitter sends out the continuous wave excitation signal at its specified frequency, and the receiver is listening for the backscatter packet at its specified frequency. Upon wake up, the tag MCU reads the wake-up RSS from the AS3933 radio and enables the 12 MHz clock and the FPGA. After a 2 ms settling time, the MCU sends out the data, including a two-byte sequence number and the wake-up RSS, to the FPGA and

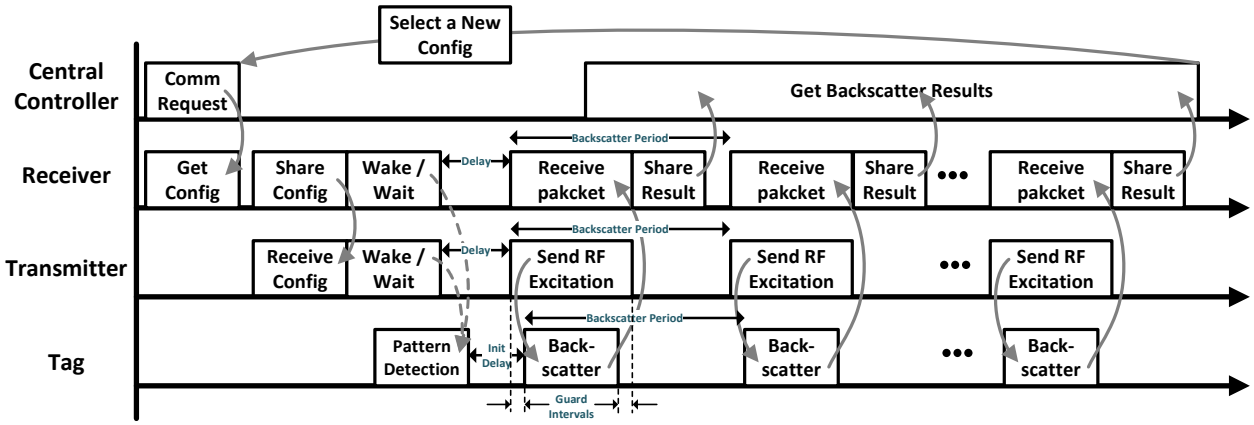

Figure 3.6: Closed-loop configuration selection system. Each cycle starts when the controller sends a communication request to the receiver. The TRXs and tag follow the timings to avoid any timing mismatch. The backscatter results are returned to the controller and used to select future configurations.

the FPGA creates a BLE packet with the data and transfers it by modulating the impedance connected to the tag antenna through the RF switch. To ensure time synchronization during backscatter operation, the receiver and transmitter keep a 300 us guard interval before the backscatter process starts and after it finishes. Once the backscatter communication is completed, the receiver shares the result with the central controller. The result includes whether the communication was successful or not, the backscatter RSS, the wake-up RSS, the tag sequence number, and the rest of the tag data. If the devices are programmed to transfer more than one backscatter packet per wake-up, this process repeats for a pre-specified number of times. All the delays in receiving wireless signals depend on the internal architecture of the ICs we use in our implementation and are constant over time. We measure these delays accurately and add delay to the operation of other devices wherever necessary to ensure proper timing between all the devices. We successfully receive up to 40 backscatter packets with one wake up without any timing mismatch.

The central controller saves each backscatter result and selects a new configuration for the next backscatter communication phase based on this information. The same process

starts again when the controller sends a new communication request to the receiver.

3.3.2 Real-time Configuration Selection Algorithm

The goal of the configuration selection algorithm is to use the channel metrics to select the configuration with the highest success probability. An ideal configuration selection algorithm should have several characteristics. First, it should find and converge to the optimum configuration with the highest success probability. Second, the algorithm should have a low response time. After the initial start, it should find the best configuration as fast as possible. Finally, it should track environment variations. If a change in the environment happens, for example, a door opens or closes, the algorithm should re-adapt to reflect the change.

In order to find the best configuration, we keep a score vector (S) for each tag over all possible configurations, where each entry is the score for a specific configuration. To assign a score to a configuration, we first need to define a score for one backscatter communication event. We define the backscatter communication event score as equation 3.2.

$$score = \begin{cases} sqrt(rss_{wake} * rss_{bs}) & \text{if packet is received} \\ 0 & \text{otherwise} \end{cases} \tag{3.2}$$

where rss_{wake} is the received signal strength reported by the tag wake-up receiver, and rss_{bs} is the backscatter packet received signal strength reported by the receiver minus the receiver sensitivity. The defined score prevents high interference channels by assigning a score of 0 to failed communications. Channels with higher margins from the link sensitivities get a higher score based on both wake-up and backscatter signal strengths.

After assigning a score to each backscatter communication, we update the score for the configuration used in that communication by equation 3.3:

$$S_{new}[config] = S_{old}[config] * \alpha + score_{bs} * (1 - \alpha) \tag{3.3}$$

where $S_{new}[config]$ is the new score for the used configuration, $S_{old}[config]$ is the old score, $score_{bs}$ is the backscatter score based on equation 3.2 and α is a smoothing factor. The

smoothing factor controls how many packets the system keeps in memory. For example, it takes 23 dropped packets to cut a score in half if the smoothing factor is equal to 0.97, while it takes only two packets if the smoothing factor is 0.7. Longer smoothing factors keep the previously learned results for longer periods and can handle temporary channel variations; for example, when someone enters a room and leaves it quickly. On the other hand, a smaller smoothing factor is more suitable to respond to permanent channel variations; for example, someone enters a room and sits behind a desk.

To break this trade-off, we keep two separate score vectors with two different smoothing factors and use the same formula as equation 3.3 to update them separately. We pick one of the two vectors randomly to report the scores. This approach ensures that at least one of the score vectors is on the right track to respond to the change in the environment, and since both vectors are updated each time with the same backscatter score, they converge to the same scores after a transient period.

Finally, we need to pick a configuration for the next communication based on the tag score vector. Initially, the score vector is filled with zeros, and all configurations have the same score. So, the algorithm picks a configuration randomly until the first successful packet is received, which causes one entry in the score vector to increment from zero. However, there is no guarantee that this is the best possible configuration. Thus, we need to explore other possible high-score configurations. At the same time, we do not want to waste resources by trying low-score configurations over and over again. So, we propose a success rate dependent exploration rate. We calculate the success rate over a fixed-length window of previous backscatter events, and use it as a confidence number for the score vector. A high success rate means that the score vector is suggesting high-quality channels and there is less need for exploration, while a low success rate means that we should keep looking for possibly better configurations. For example, if the success rate is equal to 0, we would like to reject the score vector suggestions altogether and set the exploration rate to 1. On the other hand, if the success rate is 1, we do not need to explore, and the exploration rate should be equal to zero. In this work, we use past 100 backscatter communications to calculate the success rate

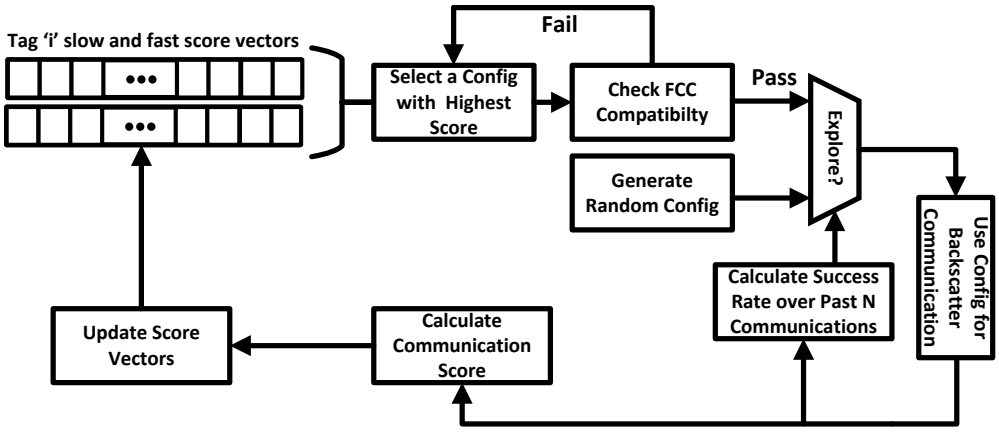

Figure 3.7: The proposed configuration selection algorithm. The score vectors keep a ranking of all possible configurations. On each iteration, the configurations with the highest scores are checked for FCC compatibility, and one is selected. The exploration rate is set based on previous communication results and forces a random configuration if exploration is needed.

and define the probability of exploration as $1 - tanh(3 * successrate)/tanh(3)$.

The proposed configuration selection algorithm is implemented in python and runs on the central controller. Fig. 3.7 shows the algorithm block diagram.

3.3.3 Frequency Hopping

FCC has specific regulations for the devices operating in the 2.4 GHz ISM band, which limits the maximum output power of devices depending on their operating conditions. A frequency hopping device can transmit up to 0.125 W (21 dBm) if it pseudo-randomly switches between 15 non-overlapping hopping channels, and up to 1 W (30 dBm) if it uses 75 such channels [30].

Our proposed system picks configurations based on their success rates, and it is likely to suggest the same frequency each time. To solve this issue, we keep a list of the last 15 used frequencies and check the suggested configuration with the highest score against this list. If we have already used the frequency in one of the last 15 tries, we move to the next configuration with the highest score. If configurations with 15 distinct frequencies

are suggested, and all rejected because they were in the used frequencies list, we pick the configuration with the frequency equal to the first entry in the list.

Selecting 15 frequencies out of the 40 BLE channels could degrade the system reliability since it forces the system to use channels with higher loss. Based on the FCC regulation, hopping channel carrier frequencies separation shall be equal to the 20 dB bandwidth of the hopping channel or 25 KHz, whichever is greater. Also, the system receivers shall have input bandwidths that match the hopping channel bandwidths [30]. Since our BLE receiver bandwidth is 1 MHz, we set the hopping channel carrier frequencies separation to 1 MHz. This change increases the number of possible frequencies from 38 to 75 and the number of possible configurations from 304 to 600, which potentially also increases the number of low loss configurations. Our BLE transceivers support much smaller frequency resolution, so this change does not affect the system cost.

3.3.4 BLE Compatibility

BLE standard uses a pseudo-random hopping pattern of the 37 frequencies in the ISM band. The hopping pattern can be adapted to exclude frequencies that experience high interference to improve co-existence with the non-hopping devices. Once the BLE devices are connected, the channel hopping occurs at the start of each connection event [13].

Unlike BLE that uses frequency hopping to avoid interference from non-hopping devices, the proposed configuration selection algorithm relies on frequency hopping to avoid high loss channels. As discussed earlier, backscatter links suffer from high propagation loss due to two consecutive propagations, and it is vitally important to use channels with a lower loss to make reliable communication. Furthermore, the proposed algorithm is not in a connection state with any of the tags. The backscatter tags stay in low power mode until they are woken up by the TRXs. One could consider using a hopping pattern similar to BLE for periodic backscatter packet exchange in a static environment in a future implementation.

Although the frequency hopping objective and algorithm are different in the BLE standard compared to the proposed backscatter system, our backscatter system uses the same

packet format and PHY specifications as the BLE standard. The proposed frequency hopping is implemented using off the shelf BLE transceivers, which shows that it does not require any hardware changes or add to the system cost.

3.3.5 Synchronization

The transceivers and the backscatter tag have to be synchronized in time and frequency to make a successful backscatter communication. Time synchronization means that the RF excitation signal must be available, and the receiver must be in receive mode before the tag starts to send out its data. Frequency synchronization means that assuming the tag uses a f_{sub} subcarrier frequency, the two TRXs frequencies must differ from each other by the same f_{sub}.

In this work, we use two wireless packets to synchronize the devices before the backscatter phase, as explained in section 3.3.1. The first one is an active BLE packet from the receiver to the transmitter that shares the configuration information and sets the start of the operation. The second one is the wake-up packet that one of the TRXs sends to the tag to bring it out of low power sleep mode and signal the presence of RF excitation to the tag. We repeat the synchronization process before each backscatter communication phase. This scheme uses the same packets for synchronization and sharing configuration and provides maximum flexibility in modifying the configuration settings for backscatter communication.

The proposed synchronization process takes a fixed duration. The packet between the TRXs and the wake-up packet is 144 µs and 4 ms long, respectively. So, the synchronization overhead depends on the length and number of backscatter packets that are transmitted in the backscatter phase. For example, a BLE coded PHY packet with 22 bytes of payload takes 2 ms. Thus the synchronization overhead is 67% if the tag transmits only one backscatter packet, and it drops to 5% if the tag transmits 40 backscatter packets in each wake-up.

In order to reduce this overhead in a future implementation, the synchronization and configuration sharing packets can be separated from each other. The devices can be set to maintain their synchronization by periodically exchanging packets between them once they

are synchronized. Such implementation can still benefit from the performance boost resulted from using low-loss channels, but it has to rely on separate packets for that purpose.

In monostatic backscatter systems[107, 122], where one device provides the RF excitation signal and receives the tag reflections, no wireless packet is needed to synchronize the RF excitation source and receiver. These devices could still benefit from the configuration selection algorithm.

3.4 System Evaluations

We evaluate the *Relacks* system in indoor environments with rich multipath reflections. For all the measurements, the tags and transceivers are placed on tripods 1.6 m above the ground. We use omnidirectional dipole antennas with -0.6 dBi average gain and maximum 0.5 dBi gain in the X-Y plane [23].

3.4.1 Communication Range

First, we evaluate the system communication range for the BLE 1 Mbps uncoded PHY and the 125 Kbps coded PHY packet formats. We run the test in a long corridor following the timing described in section 3.3.1. We set the tag to send one packet upon each wake-up, and the RF excitation power is set to 18 dBm. To measure the maximum range, we fix the TRX1 position and place the tag at different distances from it. Next, we move the TRX2 away from the tag on a straight line until the link is broken. The acceptance criteria for the maximum range is to receive at least 70 percent of the packets successfully over a 5 second period. The results are shown in Fig. 3.8.

To calculate the free space model base line, we rearrange equation 3.1 as:

$$\begin{aligned} Log(d_1) + Log(d_2) = \frac{1}{20}[P_{TX} + G_{TX} - CG_{tag} + 2G_{tag} + G_{RX} + \\ 40Log(\frac{\lambda}{4\pi}) + -mp_{tx-tag} - mp_{tag-rx} - P_{RX}] \end{aligned} \tag{3.4}$$

Everything on the right side of the equation is known in our experiments. The free space models are calculated by placing 18 dBm for P_{TX}, 0 dBi for antenna gains, 4 dB for CG_{tag},

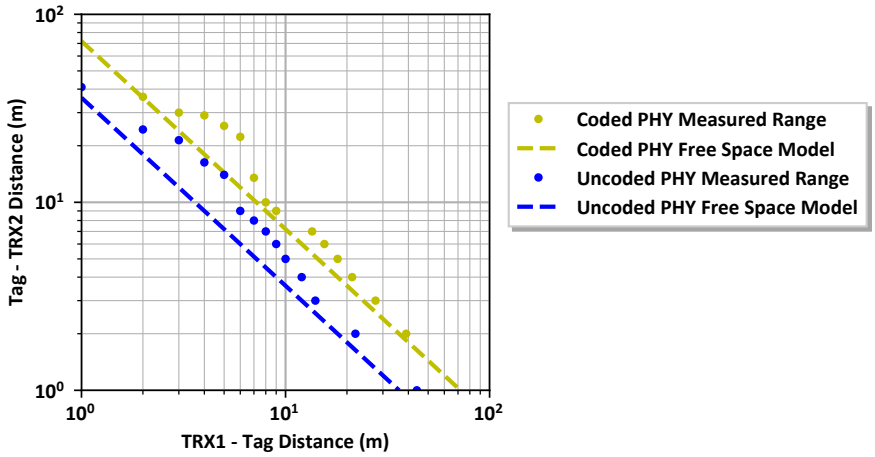

Figure 3.8: Communication range of the backscatter system in the line of sight.

-80 dB for $40Log(\frac{\lambda}{4\pi})$, 0 dBi for mp_{tx-tag} and mp_{tag-rx} and the receiver sensitivity for P_{RX} (-103 dBm for coded PHY and -97 dBm for uncoded PHY).

The backscatter system achieves an average 42.5 m communication range when the tag is 1m away from one of the TRXs using uncoded PHY, and an average 37.5 m range when the tag is 2 m away from one of the TRXs using coded PHY. Both PHYs follow the trend predicted by the free space model. We observe an average 1.79 × range improvement by using the coded PHY compared to the uncoded PHY, which complies with our expected 2 × improvement due to the 6dB better receiver sensitivity in the coded PHY. Furthermore, we observe that our system achieves a better communication range compared to the free space model baseline at every measured point. We should note that the multipath reflections in indoor environments can combine at the receiver antenna constructively or destructively. A constructive combination of the reflected signals would expand the communication range because the power of the reflected signals adds up together. Since our system dynamically searches for frequencies and antenna pairs that work best, it exploits the constructive multipath to achieve a slightly better communication range than what the free space model predicts.

Equation 3.4 shows the clear connection between the RF source output power and the backscatter coverage area ($d_1 \times d_2$). Reducing the RF source output power by 6 dB would

effectively reduce the coverage area by half. For example, if we use 0 dBm RF source output power instead of 18 dBm, we expect to achieve $\frac{1}{8}$ of the measured maximum range and coverage.

3.4.2 Backscatter Success Rate

To test the reliability of the system in covering an entire room and to verify the performance of the configuration selection algorithm, we measure the backscatter success rates at the same 14 points shown in Fig. 3.5(a). At each point, we tried both coded and uncoded PHYs, with three different configuration selection algorithms: random, the proposed algorithm with antenna diversity disabled, or enabled. When the antenna diversity is disabled, we limit both TRXs to one of their antennas. (Left antenna on TRX1 and right antenna on TRX2.) In total, we perform six different measurements at each point. For each measurement, the TRXs are set to communicate with tag 3000 times. We consider the first 500 packets as the start-up period and calculate the backscatter success rate among the last 2500 packets. Each communication follows the timing diagram shown in Fig. 3.6 with one backscatter packet communicated per cycle. As explained in section 3.3.5, the successful reception of the backscatter packet relies on the two synchronization packets. In other words, if the active BLE link between the two transceivers, the wake-up link between one TRX and tag, and the backscatter link between the two TRXs and tag have individual packet error rates equal to α, β and γ the overall backscatter success rate would be equal to $(1-\alpha)(1-\beta)(1-\gamma)$. Fig. 3.9 shows the backscatter success rates for each measurement.

The measurement with the coded PHY packet structure, the proposed configuration selection algorithm, and antenna diversity enabled achieves an average 81.2% backscatter success rate over the 14 tested points inside the room, which shows 2.67 $\times$ improvement in success rate compared to random configuration selection. The minimum backscatter success rate is 72.2%, which highlights the uniform and reliable coverage inside the room. The measurement with the coded PHY packet structure, the proposed configuration selection algorithm, and antenna diversity disabled results in an average 78.0% backscatter success

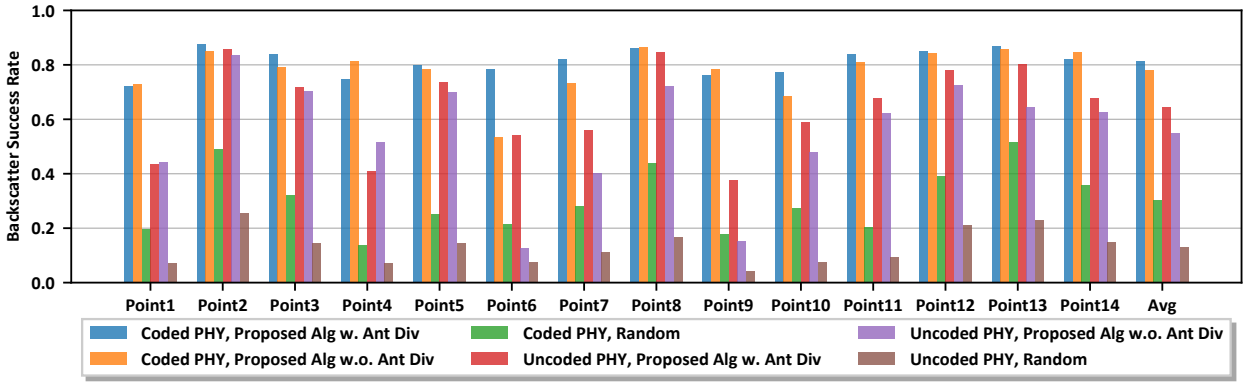

Figure 3.9: Backscatter success rate in 14 different points in a 6.4m x 9.4m area for different PHYs and configuration selection algorithms.

rate. It shows similar performance to the case with antenna diversity enabled. The exception is point 6, where the single antenna system achieves only 53.4% compared to 78.3% success rate of the system with antenna diversity. The result shows the importance of using antenna diversity to provide reliable coverage for every location.

Similarly, the measurements with the uncoded PHY packet structure and the proposed configuration selection algorithm achieve an average 61.5% and 53.2% backscatter success rates with and without antenna diversity respectively, compared to 13.1% backscatter success rate for random configuration selection. The uncoded PHY shows a higher variation in success rate, with three locations (points 1, 4, and 9) have success rates below 50%. On the other hand, the uncoded PHY achieves a similar backscatter success rate to the coded PHY at several locations (Points 2, 8, 12, and 13) with eight times data rate. Our current backscatter tag uses a physical switch on the circuit board to switch between coded and uncoded PHYs. However, in a future system, one can send commands from the TRX units to the tags to set the PHY format and trade data rate for reliability.

Consecutive dropped packets. In many applications, we would like to collect the sensor data on fixed intervals, for example, each second or minute. To ensure that our backscatter system could hand over the information on each interval, we not only need to test the system's average success rate but also the distribution of the dropped packets. We analyzed

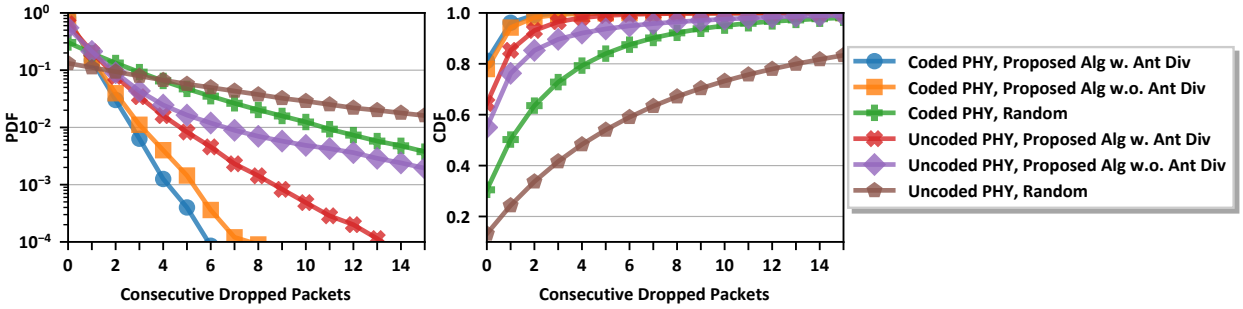

Figure 3.10: Probability distribution function and cumulative distribution function for the number of consecutive dropped packets. (Value '0' implies a successfully received packet.)

the result of the measurements at 14 different points to gain a better understanding of the dropped packets distribution. For each packet, we counted the number of dropped packets till the next successfully received backscatter packet (For successful packet, the number is equal to zero). The probability distribution function and cumulative distribution function of the consecutive dropped packets for both PHYs and all the configuration selection algorithms are plotted in Fig. 3.10. The plot shows that the likelihood of receiving a backscatter packet on the first try is 81% for the coded PHY packets with antenna diversity enabled and proposed algorithm. Furthermore, the likelihood of one dropped packet followed by a successfully received packet is 15%, and the likelihood of 5 consecutive dropped packets before a successful packet is less than 0.1%. We can use the CDF plot to calculate the number of required backscatter packets to make sure at least one packet is received with a given confidence number. For example, if the tag sends out three coded PHY packets while the system is using the proposed configuration selection algorithm, higher than 99% likelihood that at least one will be received successfully.

Delay interval effect on success rate. In previous experiments, we have received an average of 70 backscatter packets from the tags each second, which means 14 ms interval between packets. We increase the time interval between packets by introducing 0.1s, 0.3s, and 1s delay intervals on the controller to investigate its effect on the backscatter success rate. The tag and the TRXs are placed at fixed points during the test. The measured backscatter

success rates for the coded PHY packets with the proposed configuration selection algorithm are 83.0%, 83.1%, 83.6%, and 84.6% for 14ms, 0.1s, 0.3s, and 1s delay respectively. For the uncoded PHY packets, the backscatter success rates are 65.5%, 69.7%, 68.6%, and 66.3% for similar algorithms and delays between packets. We conclude that the delay interval between packets does not have a direct effect on the backscatter success rate.

Random exploration effect on success rate. Our proposed algorithm relies on random configuration selection to find the configurations with the highest success rates. To investigate the effect of this random exploration on the measured results, we fix the tag and TRXs position and run the same measurement ten times. In each run, we collect 10000 packets. The average backscatter success rate over the ten measurements is 73%, and the standard deviation of the success rates is 2.6%. The low standard deviation implies that our measurements are repeatable, and the random exploration has a limited impact on the overall performance.

3.4.3 Tag Antenna Orientation

Backscatter tags depend on reflecting the RF excitation signal to transfer their data. Antenna orientation mismatch between the tag and TRXs could affect the RF signal available at the tag antenna, and limit the communication range and reliability. To quantify the effects of the antenna orientation mismatch on our backscatter system, we set both TRXs antennas as shown in Fig. 3.11(a) and change tag antenna orientation in the XZ and YZ planes in 45 degrees step, as shown in Fig. 3.11(b) and Fig. 3.11(c) respectively. At each orientation, we collect 3000 coded PHY packets by following three different settings, as described in section 3.4.1. The backscatter success rates are shown in Fig. 3.11(d) and Fig. 3.11(e) for the XZ and YZ planes respectively. The proposed algorithm with antenna diversity maintains an average backscatter success rate of 72% and 75% in the XZ and YZ planes and show small variation with the tag antenna orientation. However, when we disable the antenna diversity and limit each TRX to one antenna, the backscatter success rate drops substantially at certain orientations. These tests clearly show the importance of antenna

(a) Base units antenna orientation for the test.

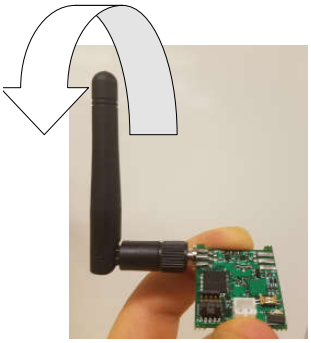

(b) Tag antenna rotation in the XZ plane.

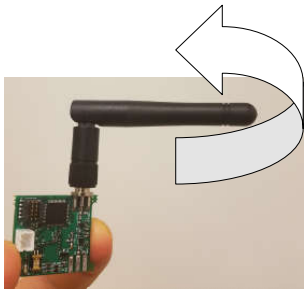

(c) Tag antenna rotation in the YZ plane.

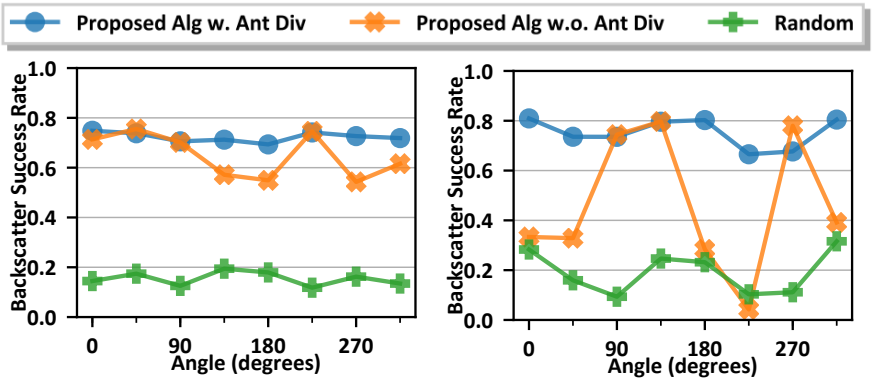

(d) Backscatter success rate dependence on tag antenna orientation in the XZ plane.

(e) Backscatter success rate dependence on tag antenna orientation in the YZ plane.

Figure 3.11: Tag antenna orientation effect on the backscatter success rate.

diversity in handling random tag antenna orientation.

Unlike frequency diversity and wake-up diversity, antenna diversity requires hardware changes. Increasing the number of antennas increases the number of independent channels and the likelihood of successful communication. However, as the number of antennas increases, the returns from adding one more antenna is diminishing [99]. Our results show that although one antenna on each TRX with frequency diversity can improve the backscatter success rate, a second antenna on each TRX quadruples the number of independent

channels and helps to make the system immune to variation in tag antenna orientation. We achieve a higher than 70% success rate at every tested point and antenna orientation, as shown in Fig. 3.9 and Fig. 3.11, so we expect marginal improvements by increasing the antennas on each TRX beyond two.

3.4.4 Environmental Variations

Our configuration selection algorithm ranks all the possible configurations based on their score in the previous communications and uses this ranking to suggest a configuration for next backscatter communication. So, the underlying assumption for this algorithm is that the configuration scores do not change rapidly over time. The configuration scores depend on the reflection characteristics of the objects in the environment surrounding the radio units and would change as the objects in the environment move. We perform six different tests to gain a better understanding of the effect of different environmental changes on the quality of the backscatter link. In each test, we let the system run for one minute. Then, we introduce a series of changes in the environment over the next minute and record the backscatter success rates over every second. The results are shown in Fig. 3.12.

In the first experiment (Fig. 3.12(a)), we ask two individuals to walk randomly in the space between TRXs and the tag. The average success rate before the event at the tag location is 75.2%, and it falls to 50% after the individuals have started to walk. We do not see any improvement over the next minute. The result is still better than a random configuration selection (24.3%). A possible explanation for the outcome is that the random movement blocks some signal paths at each instance of time while some other ones remain unaffected. In the second experiment (Fig. 3.12(b)), two persons block the line of sight between the tag and TRX1 by standing 50 cm away in front of the tag and TRX1 antennas. We observe a fall in the success rate to 40%, which is caused by the higher propagation loss due to blocking the line of sight signal path. In the third experiment (Fig. 3.12(c)), we move the tag 10cm at t= 2 s and return it to its place at t= 32 s. We see sharp drops in the success rate following each movement, but the system adapts to the new environment

following each event. In the fourth experiment (Fig. 3.12(d)), a person waves 10 cm away from the receiver antenna. The effect is similar to the first experiment, but since the moving object is smaller (a person's hand), we see a smaller drop in the backscatter success rate. In the fifth experiment (Fig. 3.12(e)), we place two laptops 1 meter away from the receiver antenna and set them to stream full HD videos using their WiFi cards. We use laptops that only support the 2.4 GHz ISM band. The access point is 2 meters above the receiver. We can see an initial drop in the success rate due to added interference affecting some of the good configurations, which have frequency overlap with the access point frequency band. The system recovers from this and maintains an average 70% success rate over the next 50 seconds of the test. In the final test (Fig. 3.12(f)), we turn the tag on and off every 5 seconds. The system quickly achieves a high success rate following each turn on, which demonstrates that the system could maintain the configuration ranking for short blockage events. These experiments were only a small fraction of all the possible environmental changes that can happen in real environments. The system continues to receive backscatter packets in all cases, which shows its resilience to environmental variations.

As we discussed earlier, the *Relacks* backscatter system relies on channels with lower propagation loss for backscatter communication. In section 3.4.2, we show that increasing the time duration between backscatter packets does not change the system performance in a static environment. In such cases, a fixed set of configurations can be used, and the TRXs do not need to share channel metrics very often. However, Fig. 3.12 shows the channel metrics could change very quickly by a small environmental variation, such as moving the tag by a few centimeters or people walking in the vicinity. In such scenarios, the TRXs have to look for low-loss channels and update configuration constantly. Thus, different backscatter deployments might have very different dynamics, and the optimum rate to share channel metrics has to be selected based on the application and deployment requirements. Increasing the configuration selection update rate increases the overhead. At the same time, it increases the likelihood of successful communication. A unified approach that provides the optimum update rate for a variety of different environment variations is a subject for future research.

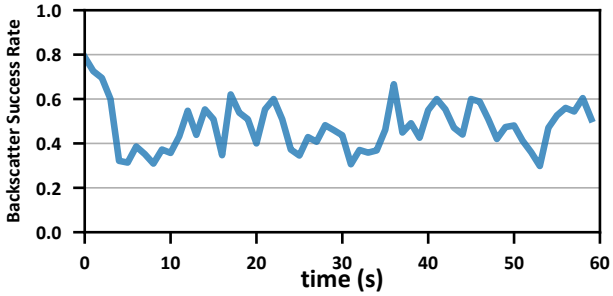

(a) Two individuals walk randomly between TRX1, tag, and TRX2..

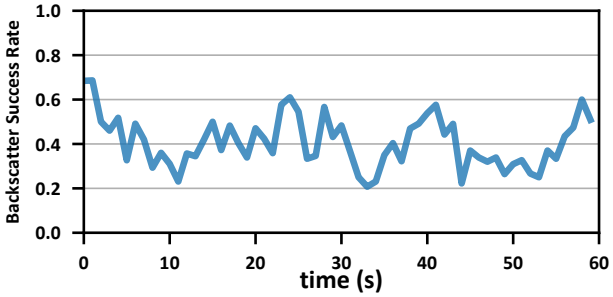

(b) Two indivisuals stand 50cm away from tag and TRX1.

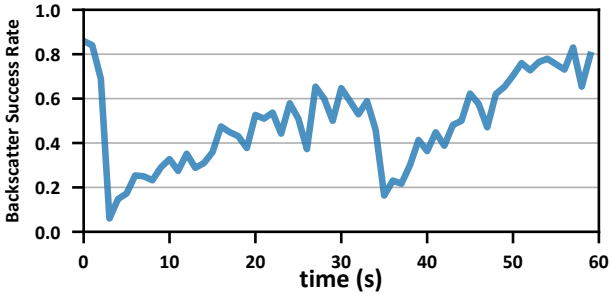

(c) Tag is moved 10cm at t=2s and returned to its place at t=32s.

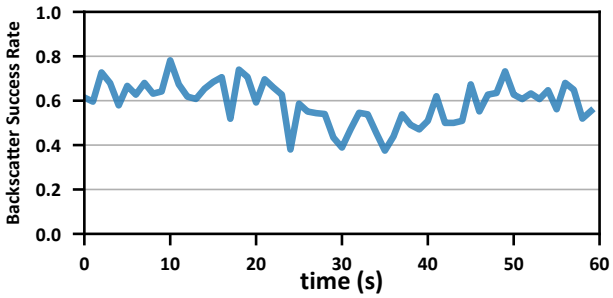

(d) A person waves 10cm away from the receiver antenna

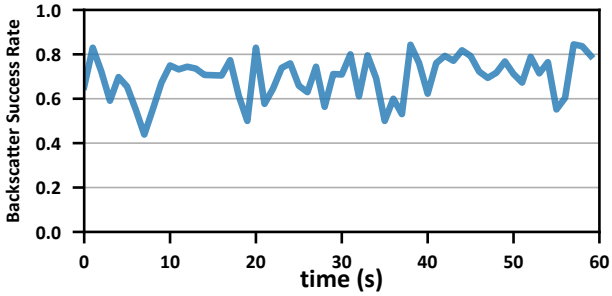

(e) Two full HD videos are streamed to devices 1m away from the receiver.

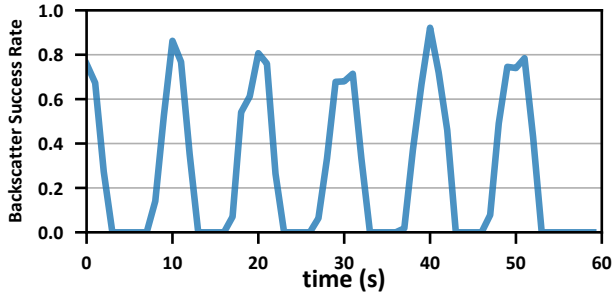

(f) Tag is turned on and turned off periodically every 5 seconds.

Figure 3.12: Effect of six different environmental variations on the backscatter success rate.

3.4.5 Long Term Case Study

We set up a day-long test to evaluate the effect of everyday activities on the reliability of the system. We place three tags in the room shown in Fig. 3.5(a) and program the controller

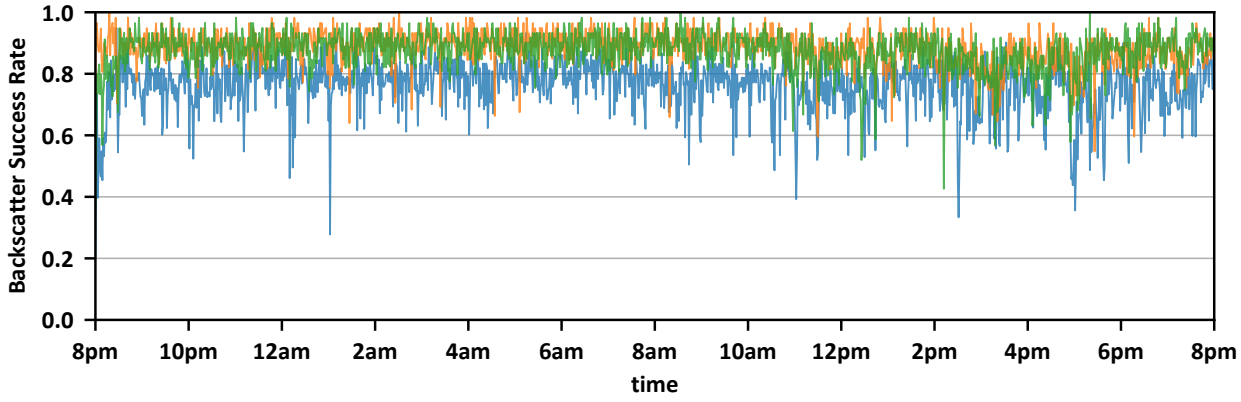

(a) The average backscatter success rate at each minute.

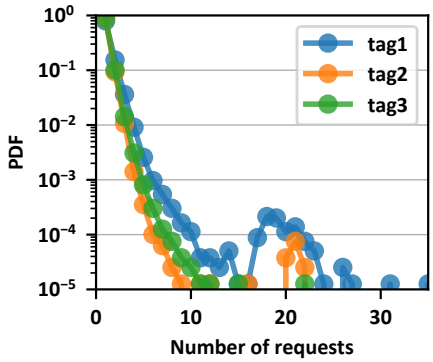

(b) Distribution of communication attempts before receiving one successful backscatter packet.

Figure 3.13: Results of a day-long backscatter communication test with three tags in a 6.4m x 9.4m area.

to send a communication request to TRX1 as described in section 3.3 till it receives one successful backscatter packet from each tag. Once the controller receives one packet from each tag, it waits for one second and repeats the operation after that. We start the test at 8 pm and end it at 8 pm the next day. The room is shared between several people, with 4 people present in the room on average between 8 am to 7 pm. People walk in and out, listen to music on WiFi, and use a microwave oven in the room several times during the test. We use coded PHY packets with the proposed configuration selection algorithm.

The average backscatter success rate at every minute of the test for each tag is plotted in Fig. 3.13(a). Tag 1, 2, and 3 have average success rates equal to 77.1%, 88.8%, and 87.2%,

respectively. We see multiple sudden drops in the minute by minute success rate for each tag. The drops are more frequent during the day than the night, which suggests they could be related to human activities. The system recovers and continues to operate at high success rates shortly after each drop. Fig. 3.13(b) shows the number of communications requests the controller sends out to get one successful packet. The average number of requests to get one successfully received packet is 1.297, 1.124, and 1.146 for tags 1, 2, and 3 respectively, with 99% of packets received with in the first three attempts. We can identify a second peak at around 20 requests for tag 1 and 2 that has happened multiple times during the test. The source of this second peak is not clear to us.

3.4.6 Multiple Test Locations

We test the *Relacks* backscatter system in several different indoor environments, including a $48m^2$ build space, a $50m^2$ classroom and a $45m^2$ conference room, to ensure its proper operation in different conditions. In each room, we place the TRXs on two opposite sides of the room, and the test procedures are as described in section 3.4.1. The average backscatter success rate for both PHYs and three different configuration selection algorithms is plotted in Fig. 3.14.

The proposed configuration selection algorithm using both antennas on each TRX and coded PHY packets achieves 83% backscatter success rate across all three environments with an average 6% standard deviation. The low standard deviation highlights uniform coverage over the entire area. By limiting each TRX to one antenna, we see a slight drop in the average backscatter success rate and an increase in the standard deviation in two of the three environments. Similar to the results discussed in section 3.4.1, the uncoded PHY measurements on average have lower success rates with a higher variation. In the three tested environments, we see a 2.7 $\times$ boost in the backscatter success rate by following the proposed configuration policy compared to random selection for coded PHY and a 3.67 $\times$ improvement for uncoded PHY.

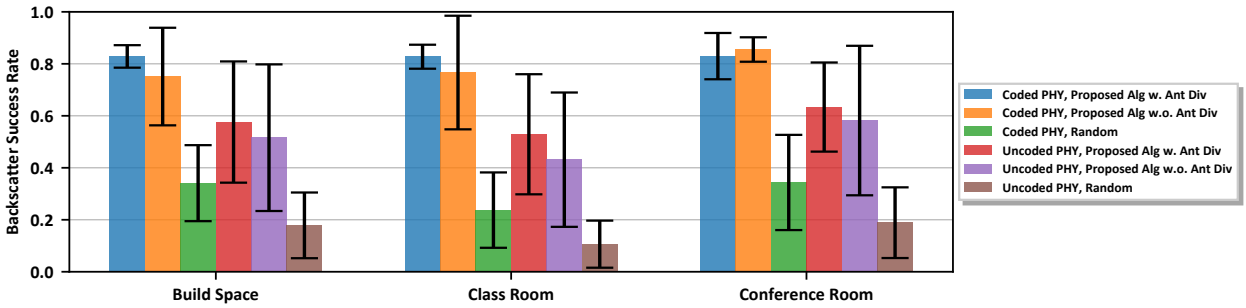

Figure 3.14: Testing the Relacks backscatter system in 3 different locations.

3.4.7 Application Deployment

Backscatter tags are cheaper than active radios [190] and can bring low-cost wireless connectivity to billions of devices around us to make many new applications possible. We show one sample application using the *Relacks* backscatter communication system. We connect an LMT86 temperature sensor to our tag and read the temperature inside a boiling pot. The data is useful to introduce new cooking recipes or add safety features to the pots. The BLE TRXs are placed on a refrigerator and a home assistant device 2 and 4 meters away from the pot. The pot is filled with water and placed on top of an electric stove. The tag is connected to the pot lid outside the pot. The temperature sensor is inside the pot, and it is connected to the tag with three wires, as shown in Fig. 3.15(a). We program the controller to send communication requests until it receives a successful backscatter packet. Then it waits for 1 second and repeats the same procedure. We continue the test until all the water inside the pot evaporates, and the temperature rises to 105 degrees Celsius. At this point, we manually turn off the electric stove. The temperature continues to rise to 118 degrees and falls after that. The measured temperature inside the pot is plotted in Fig. 3.15(b). We measure an average 73.2% packet success rate while two persons freely move around the kitchen during the test.

We compare the average energy required to transmit one successful packet with CC2640R2F BLE transceiver [19], our prototype BLE backscatter tag, and the simulated IC design for BLE backscatter tag in Fig. 3.15(c). We use equation 3.5 to calculate the energy per suc-

(a) Pot with temperature sensor and BLE tag.

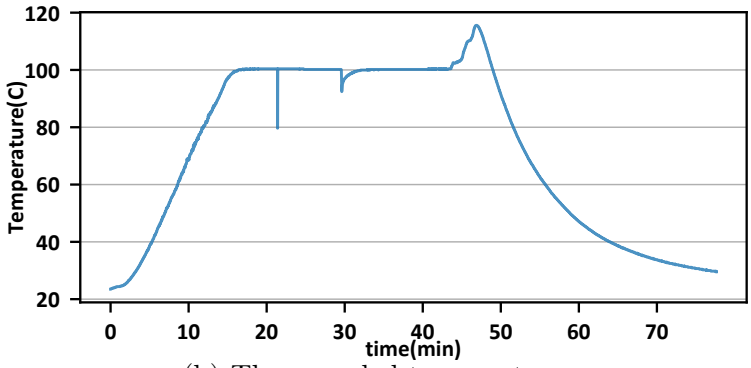

(b) The recorded temperature.

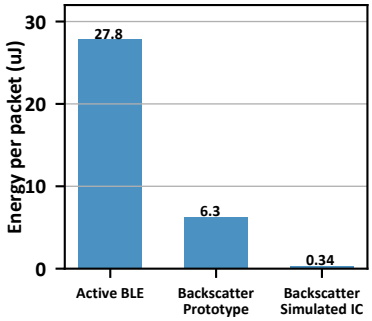

(c) Comparing energy per successful packet.

Figure 3.15: Measuring the temperature inside a boiling pot with the BLE backscatter tag.

cessful packet.

$$E_{tot} = P_{tx} * T_{tx} * \frac{1}{successrate} \tag{3.5}$$

We set the CC2640R2F to read the LMT86 temperature sensor and transmit one BLE 1M PHY packet. The entire process to exit sleep mode, activate the sensor, read the output with ADC, and transmit a BLE packet takes 2.9 ms. The average measured current consumption is 3.2 mA from a 3V supply. We assume a success rate equal to 1 for the active BLE packet, which brings the total energy consumption to 27.8 µj. Our prototype backscatter tag consumes an average 1.1 mW over 4.2 ms to send one BLE coded PHY packet. The average power consumption is lower than what measured in section 3.2 because the backscatter communication only takes 1 ms, and the remaining time is spent on waiting for the oscillator to settle. We use the same success rate as calculated in our measurement. The total energy

consumption to transmit one backscatter packet with our prototype is 6.3 µj. Based on the simulations, we project the BLE backscatter integrated circuit consumes 60 µW over the same period with equal success rate to our prototype. Thus, we expect 0.344 µj total energy consumption, which is 80 times less than the active radio.

3.5 Related Works

This work is related to prior efforts on backscatter communication systems. Long-range backscatter systems with communication range beyond hundred meters are introduced in [190, 163, 198] to cover an entire house or office using a single transmitter and receiver. These works achieve an extended communication range due to the lower sensitivity of the receiver and favorable propagation characteristics in the 900 MHz frequency band. In this work, we limit the scope of the backscatter system to a single room, which allows us to operate with a lower excitation power and a higher data rate at 2.4 GHz ISM band. Backscatter systems based on 2.4 GHz ISM band standards such as Bluetooth [90, 108, 208], WiFi [125, 108, 53, 213, 208, 209] and Zigbee [141] have introduced and achieved room level communication ranges. In this work, we extend the application of such systems by adding a method for reliable backscatter communication in a multipath-rich indoor environment.

The fading effect in indoor environments is a well-known issue [193, 76, 95]. Since we are dealing with two consecutive propagations in backscatter communication, the multipath fading could severely limit the reliable communication range. [136, 128, 102] provide detailed measurement results on the effect of multipath fading on backscatter links in 900 MHz, 2.4 GHz, and 5.8 GHz ISM bands. [111] exploits a multi-carrier backscatter system and channel diversity to communicate with multiple tags in parallel and increase the throughput. It uses a software-defined-radio based transmitter and receiver for that purpose. [207] and [100] use link metrics, bitrate selection, and channel selection algorithms to increase the throughput of the backscatter RFID system. These works are limited to RFID applications, where a single base unit provides the excitation signal and receives the reflections. [175] highlights the multipath fading issue for backscatter communication inside an animal cage

environment and relies on a one-time calibration and frequency planning between three BLE channels to improve the link reliability. Although [175] shows the importance of frequency diversity, it does not present a dynamic approach to handle environmental variation in a larger space. [198] uses multiple transmitters and receivers at different frequencies to overcome the frequency-selective multipath. This architecture occupies multiple channels and requires an additional set of transmitters and receivers for each added frequency diversity.

3.6 Conclusion

We present an efficient backscatter system that can provide reliable coverage in indoor environments. The backscatter system relies on a closed-loop configuration selection algorithm that uses frequency, antenna, and wake-up source diversity to maximize the success rate of backscatter packets. We prototype a complete backscatter system with BLE transceivers and BLE compatible tags and use them in evaluating our system. We discuss FCC compatibility, BLE compatibility, and synchronization overhead of the proposed method. The measurement results show more than 80% average backscatter success rate over the tested points inside multiple indoor environments, 2.7 times improvements over random selection baseline. We show that the proposed method is resilient against environmental variation and tag antenna orientation. Finally, we test our system for an extended period and provide a sample application to show its performance in real-life scenarios.

Chapter 4

MULTISCATTER: MULTISTATIC BACKSCATTER NETWORKING FOR BATTERY-FREE SENSORS

4.1 Introduction

Recent advances in energy harvesting, physical sensors, wireless networks, data processing, and machine intelligence picture a future where billions of everyday objects turn into smart, connected devices that can sense their surroundings, communicate their data, and react to human interactions and other environmental stimuli. This vision, however, has run into practical limitations of wireless communication networks.

An ideal wireless technology for a battery-free or self-powered sensor network should possess two essential qualifications: the sensor nodes should consume very little energy since the harvested energy is scarce, and the infrastructure to communicate with the sensor nodes should be low-cost to make widespread adaptation feasible. Current commercial wireless technologies do not satisfy these two objectives simultaneously. While recent works have demonstrated battery-free BLE [82, 185, 205, 68], Sub-GHz [96], and LoRa [147] networks, these radios may consume too much energy to support applications demanding update rates of multiple packets per second [192]. On the other hand, passive RFID readers are expensive and suffer from a short communication range, resulting in high infrastructure cost to cover a practical setting with passive RFID readers [77]. In addition, RFID does not typically support the use of arbitrary sensors such as cameras and microphones.

Recent bistatic backscatter systems [106, 119, 125, 163] have shown promise to find a middle-ground to this challenge by employing the backscatter technology to reduce the energy burden of wireless communication, while leveraging the economies of scales and ubiquity of industry-standard protocols such as WiFi, Bluetooth, ZigBee, and LoRa to reduce the cost of

reader infrastructure. Bistatic backscatter systems still suffer from a shorter communication range than conventional active radios, and a single receiver (RX)-transmitter (TX) pair is insufficient to cover a multi-bedroom or multi-floor house at practical data rates. The limited coverage of backscatter systems complicates the user experience and limits their use cases.

To extend the coverage of a wireless network, the idea of using multiple base units is suggested and implemented in cellular [165, 56] and WiFi [161, 80] networks for a long time. However, high propagation loss, strong interference, frequency-dependant operation and non-homogeneous base units complicates the deployment of a backscatter network with multiple base units (see §4.2 for a primer on backscatter systems).

Furthermore, the battery-free sensor nodes have strict energy limitations, while the base units have higher computational and energy resources. This imbalance requires the system to push the network management tasks to the base units while keeping the sensor nodes as simple as possible.

We notice that unlike a cellular base station that covers a circle around itself, the coverage area of the bistatic backscatter system is almost entirely limited to the area between the TX and RX units (see Fig. 4.2). This difference means that we do not need another TX-RX pair to double the coverage area of a bistatic backscatter system. We only need to add a second TX unit and share one RX unit between the two TX units (or vice versa). We extend this idea of sharing TX units and RX units among one another, to form a multistatic network of many TX and RX units that covers more extensive areas, as shown in Fig. 4.1. This solution still uses backscatter to communicate with the sensor nodes, which reduces the energy harvesting barrier for a practical solution. Although this solution needs multiple base units similar to an RFID solution, each TX or RX base unit is significantly cheaper than an RFID reader.

4.1.1 MultiScatter

In this chapter, we present MultiScatter, the first multistatic backscatter network for battery-free sensing, where a network of multiple RX and TX base units is employed to deliver

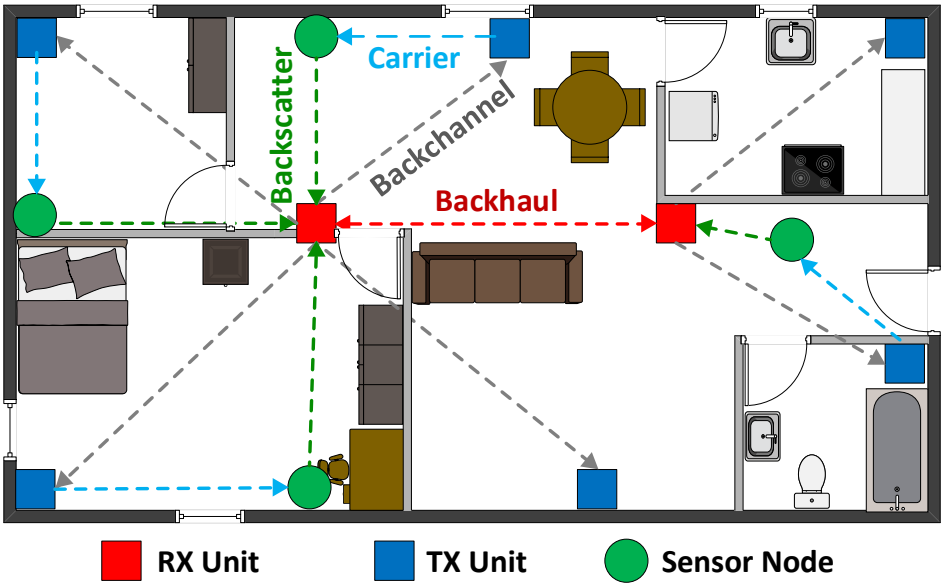

Figure 4.1: MultiScatter System Architecture. We deploy multiple RX (red squares) and TX (blue squares) base units and introduce several coordination techniques to extend the coverage of low-cost backscatter networks and deliver seamless connectivity to battery-free sensor nodes (green circles).

backscatter connectivity to many battery-free sensor nodes over a wide area. We extend the idea of bistatic backscatter with a single RX-TX pair to multistatic backscatter with multiple RX and TX base units, where any RX-TX pair can communicate with any sensor node in its vicinity. We introduce a MAC layer for the multiscatter backscatter network that performs two critical tasks: first, it selects the best RX-TX pair, carrier power, and frequency in communicating with each sensor node to maximize the throughput, and second, it handles the handover between base units as the sensor node moves inside the coverage area. This seamless connectivity addresses one of the remaining challenges in using backscatter systems and creates many new opportunities in smart homes and smart buildings by enabling peripheral, wearable, and medical devices such as pill bottles [155] and insulin pens [131] to use backscatter to transfer data to the cloud.

Summary of architecture

Fig. 4.1 shows the architecture of the system. The RX units manage the operation of the TX units and sensor nodes. We make this design choice since, unlike the TX units, the RX units have direct access to the backscatter channel state information.

The RX units support three different wireless communication interfaces. They can receive backscattered packets from the sensor nodes (dashed green line in Fig. 4.1). The RX units can also actively send packets to the TX units; we call this the backchannel link (dashed gray line). The RX units use the backchannel link to activate the best TX unit for each sensor node and set TX parameters like carrier frequency and power. Finally, a backhaul link (dashed red line) allows RX units to communicate with other RX units to share network state information, including the sensor nodes' connection states.

The TX units support two wireless interfaces: they receive active packets from the RX units, and transmit the commands and carrier signal to the sensor nodes (dashed blue line).

Deployment design support tool

To handle the complex coverage scenarios of a multistatic backscatter system in indoor environments, we develop a deployment planning tool to assist us in finding the optimum placement of RX and TX base units. While using two different base unit types is a major factor in lowering the cost of backscatter infrastructure, it complicates the deployment. The backscatter coverage depends on several factors, including the carrier source power, receiver sensitivity, and receiver blocker tolerance [121], and the objects and obstacles in indoor environments further complicate the coverage of a multistatic backscatter system. Our tool takes into account the backscatter range equations, attenuation through obstacles in indoor environments, and possible base unit coordinates and suggests the best spots for RX and TX units.

Improved Power-Coverage-Data rate trade off

Our system design provides high data rate and wide coverage area for sensor nodes that power low enough to operate from harvested energy. The power reduction is achieved by using backscatter communication. Previous work has demonstrated battery-free microphones [191] and cameras [180, 105, 181]. However, these early results are not general: they relied on special-purpose analog modulation schemes that were custom designed for the specific sensor data. This work presents a general-purpose sensor node platform that can backscatter arbitrary digital sensor data as 802.15.4g-compliant packets. The demonstrated sensors include cameras and microphones, as well as sensors for temperature, humidity, and illuminance. Our sensor nodes are equipped with an ultra low power radio to wake them from sleep mode and receive commands. The sensor nodes can operate entirely on the energy harvested from a $2in^2$ solar cell under indoor light intensity levels.

Previous long-range backscatter deployments such as [190, 198, 163, 106] used a single TX-RX pair and extended the communication range by using very sensitive, low data rate protocols. However, this technique is not scalable. The coverage area of one base unit has an upper limit, and one would need more than one base unit to extend the coverage beyond that. In this work, we provide wide area backscatter deployment coverage using a larger number of multi-statically defined small cells, which allows us to maintain higher data rates for the battery-free sensor nodes.

4.1.2 Contributions

Our main contributions are summarized below:

• We present the first multistatic backscatter network for battery-free sensing. Our system relies on three different wireless links and uses several coordination techniques between the base units to deliver a high throughput seamless connectivity over a wide area to battery-free backscatter sensor nodes. Our MAC layer implementation selects the best RX-TX pair in communicating with each sensor node to maximize the throughput and handles the handover

between base units as the sensor node moves inside the coverage area.

• We develop a deployment planning tool to assist us in finding the optimum placement for RX and TX base units to maximize the coverage in indoor environments. Our tool considers the backscatter range equations, attenuation through obstacles in indoor environments, and potential base unit coordinates and suggests the locations for RX and TX units.

• We build the MultiScatter system, including the RX and TX base units, and sensor nodes and evaluate it in different scenarios. Our evaluations show that the MultiScatter can cover a 23400 ft^2 educational complex using 5 RX units and 20 TX units for a total cost of $569. Furthermore, the aggregate throughput of the backscatter network increases by using more RX units. Using 5 RX units, our backscatter network collects data from multiple sensors at an aggregate rate of 375 Kbps, 4.17 times faster than a single sensor node throughput.

Platform availability. MultiScatter's design files are publicly available at [3].

4.2 Bistatic Backscatter Coverage

Unlike conventional wireless networks where the communication happens between two devices- an access point and a mobile device- three devices are involved in a bistatic backscatter communication; a TX unit that generates the carrier signal, a backscatter sensor node that modulates and reflects the carrier, and an RX unit that listens to, and decodes the sensor node data.

One of the main challenges in backscatter systems is the strong interference at the receiver due to the carrier signal. Bistatic, or half-duplex, backscatter systems rely on physical separation of the TX and RX units to reduce the carrier interference [125, 119, 190], while monostatic, or full-duplex, backscatter systems rely on self-interference cancellation circuits for this purpose [122, 61, 88]. Another popular technique to mitigate the carrier interference is using sub-carrier modulation at the sensor node [125, 119, 190, 122, 88, 209, 198, 108] to generate the backscatter packet at a frequency offset from the carrier signal. This technique pushes the carrier signal out of the desired band at the receiver and reduces the receiver's

sensitivity loss, since receivers can tolerate out-of-band interference.

The coverage of a bistatic backscatter system depends on the relative distance of the RX and TX units and characteristics such as receiver sensitivity and blocker tolerance, transmitter output power, backscatter node conversion gain and antenna gain as described in [125, 121].

Receiver sensitivity determines the weakest signal power level detectable by the receiver. In other words, if the receiver sensitivity and desired signal power at the receiver are Sen_{RX} and P_{RX} respectively, the receiver sensitivity criterion to detect the incoming signal is $P_{RX} > Sen_{RX}$. For a backscatter link, P_{RX} can be calculated from equation (4.1) [93].

$$\begin{aligned} P_{RX} =& P_{TX} + 10n\log_{10}\left(\frac{\lambda}{4\pi d_1}\right) + 10n\log_{10}\left(\frac{\lambda}{4\pi d_2}\right) \\ &+ G_{TX} + G_{RX} + 2G_{tag} - Loss_{tag} \end{aligned} \tag{4.1}$$

where P_{TX} is the transmitted power at the RF source, λ is the signal wavelength, n is the path loss exponent, d_1 and d_2 are the TX-tag, and tag-RX distances, $Loss_{tag}$ is the RF loss in tag, G_{TX}, G_{RX}, and G_{tag} are the transmitter, receiver, and tag antenna gains, respectively.

In addition to the receiver sensitivity, its selectivity adds another limitation to the operating range of the backscatter communication systems. If the RF excitation signal power at the receiver is $P_{TX@RX}$ and the receiver selectively is Sel_{RX}, the selectivity criterion for the receiver can be expressed as $P_{TX@RX}$ - $P_{RX} < Sel_{RX}$. Equation (4.2) relates $P_{TX@RX}$ to the link parameters [93].

$$P_{TX@RX} = P_{TX} + 10n\log_{10}\left(\frac{\lambda}{4\pi d_3}\right) + G_{TX} + G_{RX} \tag{4.2}$$

where d_3 is the distance between the transmitter and receiver.

We combine equations (4.1), (4.2) and the sensitivity and selectivity criteria to model the system communication range:

$$d_1 d_2 < (\frac{\lambda}{4\pi})^2 \times \quad 10^{[\frac{1}{10n}(P_{TX}+G_{TX}+G_{RX}+2G_{tag}-Loss_{tag}-Sen_{RX})]} \tag{4.3}$$

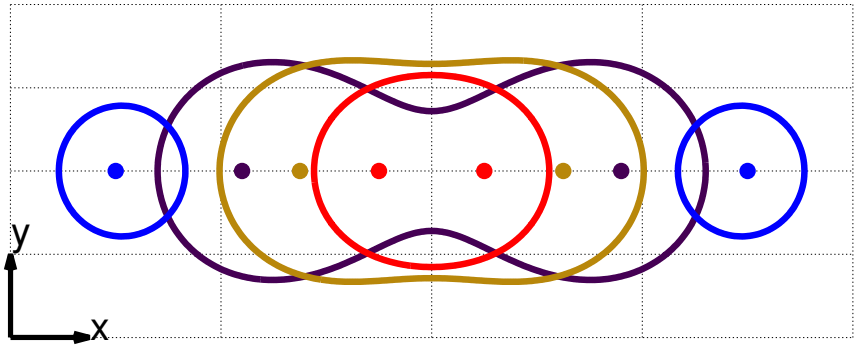

Figure 4.2: Backscatter coverage dependance on the RX-TX distance. Placing the RX-TX too close (red) or too far (purple and blue) results in non-optimal coverage scenarios.

$$\frac{d_1 d_2}{d_3} < (\frac{\lambda}{4\pi}) \times 10^{[\frac{1}{10n}(2G_{tag} - Loss_{tag} + Sel_{RX})]} \tag{4.4}$$

Unlike an active radio link where the communication range is determined by one number -the distance of the two devices-, the communication range should be defined by the relative distance of all three devices for a backscatter link. Equation (4.3) relates the tag-RX and tag-TX distances to the receiver sensitivity, and equation (4.4) brings the TX-RX distance into the picture and relates the relative distance of all three devices to the receiver selectivity. To derive these equations, we assume that the transmitter and receiver antenna gains are equivalent in different directions. One should consider the antenna gain differences if this assumption is not valid. Based on the equations, lower sensitivity or a higher selectivity expand the communication range.

We use the two equations to plot the backscatter coverage in four different cases in Fig. 4.2. The RX and TX locations are shown with circles of the same color in each case. When the TX and RX are too close to each other, they completely cover the area between themselves, but the carrier interference limits the coverage area (red plot). As the RX-TX distance increases, the coverage area expands to reach its maximum (brown plot). If we further increase the RX-TX distance, first, the coverage width at the center starts to shrink

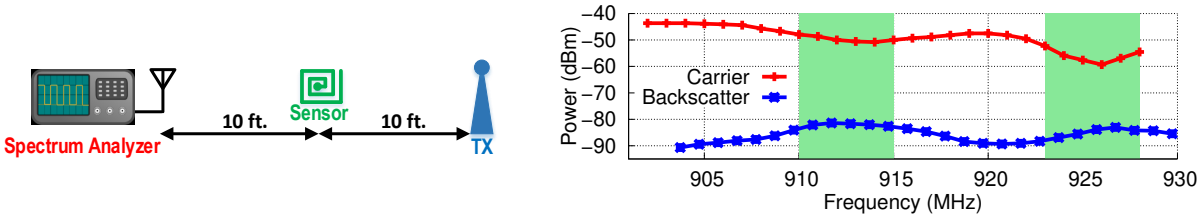

(a) Multi-path fading experiment setup.

(b) Carrier and backscatter signal power at the RX.

Figure 4.3: Effect of multi-path fading on backscatter link.

(purple plot), and finally, we lose the coverage at the center and the coverage map becomes disjoint (blue plot). Although we use a hypothetical backscatter system and the free-space propagation model in this analysis, the coverage variation trend is similar in all bistatic backscatter systems, and it highlights the importance of RX and TX units placement in covering large spaces with backscatter connectivity.

In this analysis, we used free-space path loss models to calculate the backscatter and interference powers at the receiver. However, the wireless propagation in indoor environments is subject to multipath fading. To show the effect of the multipath fading, we perform a simple experiment. We set a transmitter to generate a continuous wave carrier signal, and a backscatter node, placed 10 ft away from the TX, to reflect the TX signal at 1.7 MHz offset frequency, as shown in Fig. 4.3(a). We use a spectrum analyzer, placed 10 ft away from the backscatter node, to measure the carrier and corresponding backscatter signal powers. Fig. 4.3(b) shows the carrier and backscatter signal power as we sweep the carrier frequency from 902 MHz to 928 MHz. The backscatter (i.e., desired) signal power varies 10 dB in this experiment, while the carrier (i.e., interference) signal power varies 15 dB. The two signal powers are independent of each other, and their peaks and valleys happen at different frequencies. The best frequency bands for backscatter communication are the ones with maximum backscatter signal power and minimum carrier power as shown in Fig. 4.3(b) with green strips.

4.3 System Design

This section describes the backscatter network architecture used to cover a wide area and communicate with many sensor nodes. We start with one RX-TX pair and extend the coverage first by adding more TX units and finally by including more RX units. Throughout this section, we assume that each sensor node has a unique identification number (ID), and the backscatter network has prior knowledge of the sensor nodes' IDs.

4.3.1 Single RX - Single TX

In the simplest form, a bistatic backscatter system consists of one RX unit, one TX unit, and one or several sensor nodes. The RX and TX should coordinate with one another to achieve three main functionalities: improving the link reliability, time-frequency alignment, and handling retransmissions. We use a wireless backchannel between the RX and TX units to communicate and coordinate between the two devices.

The communication cycle of the system is shown in Fig. 4.4. It starts with selecting the optimum parameters for the frequency channel and carrier power to maximize link throughput and minimize the error rate in communicating with the specified sensor node. The RX uses scores calculated based on the results of previous communication cycles for this purpose. The RX selects the frequency channel with the highest score that satisfies the frequency hopping requirements of the regulatory mandates. It also finds the carrier power with the highest success rate and uses it as the center of probability distribution to select the carrier power (Fig. 4.4(a)). After selecting the communication parameters, the RX shares them with the TX unit. The TX unit has been in listening mode until it receives an activation packet from the RX unit on the backchannel. The activation packet also specifies the duration of the carrier signal that the TX unit has to generate, as well as the sensor node identification number and the command for the sensor node (Fig. 4.4(b)). Once the TX unit receives the activation packet, it sends a packet to the sensor node, which contains the sensor node ID and the requested command, to wake the sensor node (Fig. 4.4(c)). Finally, the sensor node

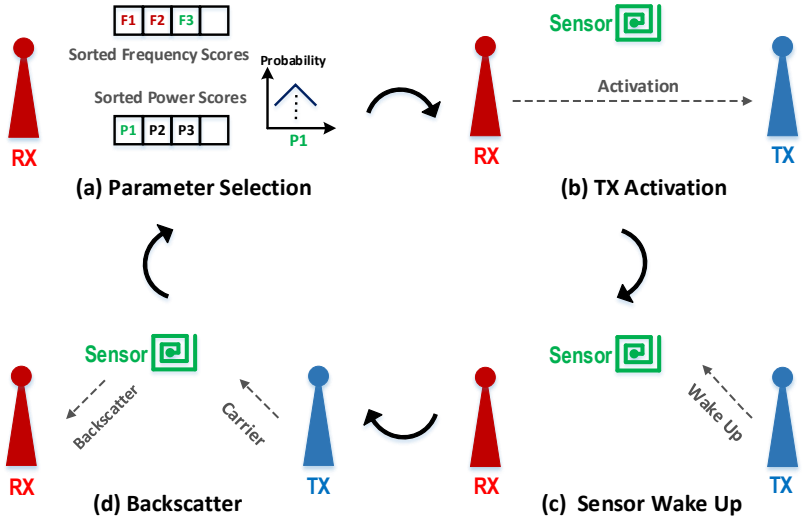

Figure 4.4: Proposed Communication cycle.

wakes up, receives the command, and responds appropriately by transmitting one or several backscatter packets. During this period, the TX generates the carrier signal, and the RX listens for the backscatter packets (Fig. 4.4(d)). When the backscatter duration is over, the RX unit analyzes the received packets based on the command issued to the sensor node and decides whether retransmission is required or not. It also updates the frequency and power score vectors based on the communication cycle results. The devices follow the same cycle for the subsequent communications between them.

The first step of the communication cycle is to select backscatter frequency and power level. This step is vital to improve the overall throughput and reliability of the system since backscatter and carrier signal strengths at the receiver vary significantly at different frequency channels due to the multipath in indoor environments, as mentioned in Sec. 4.2. Similarly, the carrier power could affect the performance of the backscatter communication too. Increasing carrier power increases both the backscatter signal power and TX carrier interference at the RX unit at the same time, and might improve or deteriorate the performance of the backscatter link [121]. We assign a success score to each communication cycle based on the

ratio of the successfully received packets to the total expected packets, and update the score for the frequency channel and power level used in the cycle with a moving average formula. To explore the entire space of possible frequency and power values, we set an exploration probability based on the error rate over a predefined number of previous communication cycles. In exploration mode, we select the two parameters randomly [119].

The communication cycle allows the RX unit to control the TX carrier frequency, start time and duration through the activation packet. This control is essential for two reasons. First, the TX unit can not generate the carrier signal indefinitely since it would waste energy and generate too much interference for other wireless users in the vicinity. The TX unit should only generate the carrier when required by the sensor node, which means the devices should be time-aligned to utilize the spectrum and energy resources efficiently. Furthermore, the TX has to hop between different frequencies in the ISM band to satisfy regulatory mandates [30]. Since the desired signal frequency at the RX is equal to the TX frequency plus the subcarrier modulation frequency of the sensor node [125, 119, 190], the RX needs to know these two values in order to frequency align itself with other devices. Using the activation packet to initiate and control the TX operation guarantees time and frequency alignment between the devices.

In the proposed communication cycle, the RX unit sends the sensor node command to the TX unit, and the TX unit passes the command to the sensor. Thus, the data communication effectively happens between the RX unit and the sensor, with the TX unit facilitating the data transfer between them. The two base units have different capabilities in a bistatic backscatter network. The RX unit demodulates the backscatter signal and detects whether the desired packet is successfully received or failed, and the TX unit can communicate with the sensor node. By using the TX unit as a relay, the RX unit has complete control to ask for retransmissions.

4.3.2 Single RX - Multiple TX

The system described in Sec. 4.3.1 highlights the fact that the data exchange happens between the RX unit and the sensor nodes. Thus, adding more TX units to the system improves the backscatter system coverage without significantly affecting the system architecture. One approach to developing such a network with multiple TX units is to command all units simultaneously to generate a carrier signal at a specific frequency. However, this method faces two major challenges: first, using multiple transmitters would not guarantee better performance because signals from different transmitters might combine destructively and decrease the backscatter signal power at the receiver. Second, it would increase the system energy consumption and interference to other wireless systems in the vicinity. Thus, the communication system must select one TX unit for each communication cycle to maximize the throughput. We use the RX unit to control the system's operation and set the TX unit at the start of each cycle.

To compare the performance of different TX nodes in communicating with each sensor node, we assign a confidence score to each TX unit. The confidence scores are initialized to 1 and updated with an exponential moving average formula using the cycle success rate each time the TX unit-sensor node combination is used. Fig. 4.5 shows sample confidence tables in the single RX - multiple TX arrangement for two sensor nodes. The frequency and power score vectors depend on the geometrical placement of the devices with respect to each other and change based on the selection of the TX unit. Thus, the RX unit needs to record one set of these score vectors for each TX unit-sensor node combination.

We follow the following procedure to select a TX unit based on the confidence table at the start of the communication cycle. First, we select the TX units with confidence scores higher than 0.9. If the set has more than one member, we use a weighted random selection to select one of them. If the set has no member, we filter out the TX units with confidence scores less than 0.2 times of the maximum confidence score, and use a weighted random selection to select one of the remaining TX units. Once the TX unit is selected, we follow

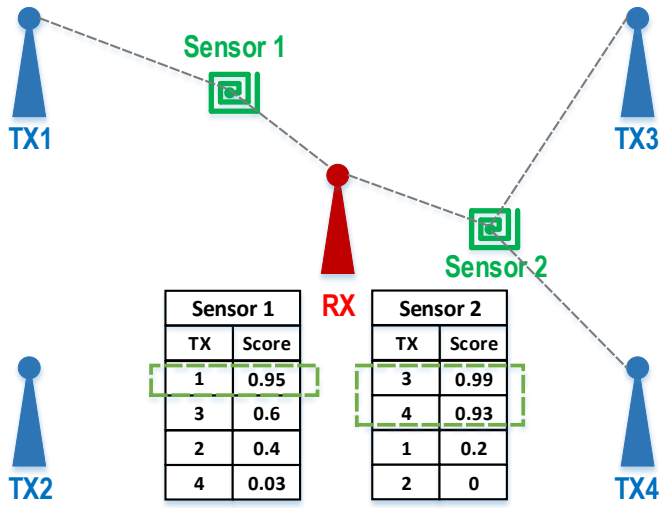

Figure 4.5: TX unit selection in a single RX - multiple TX scenario based on assigned confidence scores.

the communication cycle, as explained in Sec. 4.3.1, with the selected TX unit. We assign a unique ID to each TX unit and include the transmitter ID in the activation packet.

Similar to the single RX-single TX architecture, the TX units are in listening mode until they receive the activation packet. The TX units only move forward with transmitting the carrier if their ID is matched to the one in the activation packet. Otherwise, they discard the activation packet and return to the listening mode.

4.3.3 Multiple RX - Multiple TX

Increasing the number of TX units around one RX unit allows us to expand the backscatter coverage around the RX unit in different directions. However, we can only achieve a truly scalable system and cover areas beyond the reach of a single RX-TX pair by employing more than one RX unit. In the Multiple RX - Multiple TX arrangement, we break the area that we need to cover into several sections and use one RX unit with one or multiple TX units to cover each section. Similar to cellular networks, a sensor node might move between these

sections. Since the backscatter sensor nodes do not have the hardware or energy resources to determine the link quality metrics, the base units have to handle the handover. We add a server role to the network that assigns the sensor nodes to the RX units and updates these assignments as the sensor nodes move. The server could be one of the RX units, or a separate device. We equip the RX units with WiFi and use it as the backhaul link to communicate with the server.

Once a sensor node moves from section A to section B, we need to change its assigned RX unit. For this purpose, first, the RX_A must alarm that the sensor node is missing, and then, the RX_B must search for the sensor node and successfully communicate with it. A sensor node could move to any other section between two communication cycles in a backscatter network, since the sections are small and the time interval between communication attempts could be long.

We use the number of consecutively dropped packets as the metric to detect a sensor node is disconnected from its assigned RX unit since once a sensor node leaves a given section, all backscatter communication attempts with that sensor would fail.

We define the re-assignment cost ($Cost_{RA}$) as the average number of communication cycles that the system needs to correctly assign a new RX unit to a relocated sensor node. We can calculate the re-assignment cost in number of communication cycles using equation 4.5:

$$Cost_{RA} \ = \ (Thr_{drops} \ + \ 0.5 \ \times \ N_{TX} \ \times \ N_{ch}) \ \times \ (\frac{1}{1 \ - \ PFA}) \tag{4.5}$$

where Thr_{drops} is the threshold for consecutive dropped packets that is used to flag a missing node, N_{TX} is the number of TX units in the network, N_{ch} is the number of communication cycles that an RX-TX pair needs to search for the sensor node, and PFA is the probability of false alarm. There is a trade-off in selecting the threshold to announce the disconnection to the server. Higher thresholds waste network resources by trying to communicate with a sensor node that has left the section. On the other hand, lower thresholds increase the probability of false alarm. To select the optimum threshold that minimizes the cost, we need to know the N_{ch} for a reliable search procedure and model the probability of false alarm at

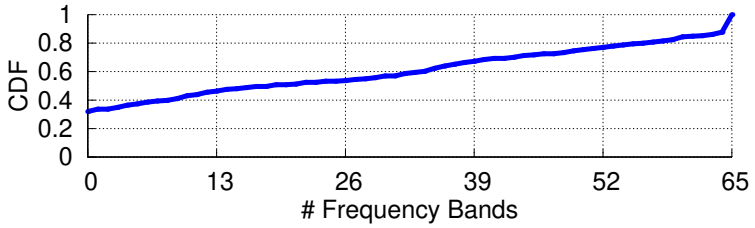

(a) Distribution of number of operative bands at 240 locations.

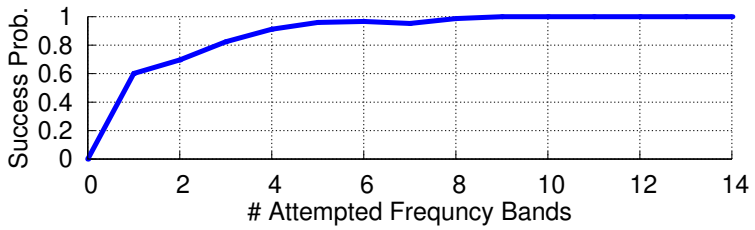

(b) Probability of communication with a sensor node based on number of equal-distant frequency bands attempted.

Figure 4.6: Selecting the number of frequency bands for the search procedure.

different Thr_{drops} values.

Search Procedure (N_{ch} selection). An ideal search procedure should be fast and accurate. Due to the lack of existing knowledge about channel properties, the RX units have to try different frequency channels to increase the likelihood of successful communication with the sensor node at the new location. However, increasing the number of frequency channels in the search procedure would increase the search duration (N_{ch}). Previous studies [136, 128] show that the multipath fading loss in indoor environments becomes uncorrelated as the frequency separation increases. To find the optimum number of frequency bands for the search procedure, we set up TX-RX base units at 12 different locations with 20 sensor node testing points (240 total) around them. For each setup, we set the carrier power at the maximum and try all the frequency bands between 902 MHz and 928 MHz with 400 KHz channel spacing to communicate with the sensor node at each point.

Fig 4.6(a) shows the distribution of number of operative bands over the 240 points, with

35% of the points not responding at any frequency and 13% of the points responding at all of them. We consider the points which respond at least at 10% of the frequency bands (150 points) as the target group and plot the probability of communicating with the sensor at these target points based on the number of attempted frequency channels in Fig 4.6(b). The figure shows that trying 9 channels results in 99% search accuracy. We consider some margin for errors in these experimental results and use 12 equally spaced frequencies in our search routine, which means the search procedure takes 12 commutation cycles.

Threshold Selection. The probability of false alarm (PFA) is the ratio of false alarms to total alarms. The main cause of successive dropped packets that leads to a missing node alarm is the movement of the sensor nodes. Ideally, we would like the RX unit to generate an alarm only when the sensor node is moved to a different section. However, moving the sensor within the boundaries of a section could result in multiple consecutive dropped packets, too, since the RX units have to re-tune the score vectors for the new sensor location as described in Sec. 4.3.1. This further complicates the threshold selection. We can calculate the false alarm rate using equation 4.6:

$$PFA \;=\; P_{inside} \;\times\; PFA_{inside} \;+\; P_{outside} \;\times\; PFA_{outside} \tag{4.6}$$

where P_{inside} and $P_{outside}$ are the probability of a sensor moving inside and outside of a given section respectively, and the PFA_{inside} and $PFA_{outside}$ are the probability of generating an alarm as a result of those moves. Based on our definition, any alarm generated when the sensor moves outside the section is true, and hence, $PFA_{outside}$ is equal to zero. Also, we assume an 80%-20% split between the probabilities of moving inside and outside a section. Thus, to estimate the PFA, we must model the probability of false alarm caused by moving a sensor inside a section for different thresholds.

We perform an experiment by moving the sensor node within the boundaries of one section 100 times in 5 different environments. Fig. 4.7 (blue line) shows the probability of generating an alarm for different thresholds in these experiments. If we apply these probabilities to equation 4.6 and assume N_{TX} and N_{ch} are equal to 10 and 12 in equation 4.5, we can

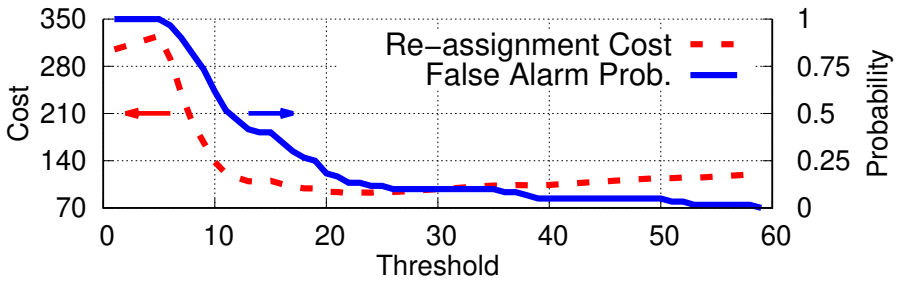

Figure 4.7: Probability of false alarm (blue) and the overall re-assignment cost in communication cycles (dashed red) for different consecutive dropped packets thresholds.

calculate the re-assignment cost for different threshold levels as shown in Fig. 4.7 (red line). Based on this plot, the optimum threshold of consecutive dropped packets for a system with 10 TX units is 22 packets.

Server. The server tracks the assigned RX unit for each sensor node. Once one of the RX units detects a missing sensor, it notifies the server. The server then randomly notifies one of the other RX units to search for the missing sensor node and waits for the search result. If the search fails, the server notifies another RX unit, and this procedure continues until one of the RX units successfully communicates with the sensor node. The server holds a predefined period before notifying the same RX unit again.

4.3.4 Base Units Placement

Selecting the number of base units to cover an area and finding their optimum placement could be challenging, especially in residential and commercial buildings, which are the primary target of the MultiScatter system. Thus, we need a tool to help us plan the deployment and estimate the coverage area for a given placement of base units without the time-consuming process of deploying the units in the field. Although several RF propagation simulators are available [52, 51], to the best of our knowledge, none of them supports backscatter systems.

Several factors complicate the placement of base units in indoor environments. First, the

coverage of a single RX-TX pair of our multistatic network is a complex function of the RX-TX relative distance, as shown in Fig. 4.2, as well as other factors such as TX carrier power, RX sensitivity, and blocker tolerance [121]. Furthermore, indoor areas are most often divided into several sections by walls, partitions, or other obstacles. The RF signals attenuate as they pass through different materials. It is essential to consider the effect of these obstacles in the placement of the RX and TX units to achieve optimal performance. Finally, the base units have high energy consumption and need a permanent energy supply such as a wall power outlet. This adds another limit to the placement of the base units since we prefer to keep the base units closer to the wall power outlets and avoid long wires.

Our tool uses the Friis formula [93] to estimate the backscatter signal and carrier interference power levels at the receiver. We use the backscatter coverage equations in [121] to determine the backscatter coverage at each point in the environment. We estimate the attenuation through walls and other obstacles using the proposed models in [174, 58, 57]. Although our simulator is limited to path loss and absorption loss models in two dimensions and does not consider RF propagation effects such as reflections, diffraction, and scattering, it still provides valuable insight for placing the target area's base units.

Our deployment tool takes the geometry of the area and coordinates of the base units as the inputs and calculates the maximum backscatter signal power amongst all the RX-TX pairs at each point to generate a coverage map. We follow a manual trial-and-error process to find the number and position of the base units required to achieve the desired coverage. In each iteration, we move the base units and add more units, if needed, to get the desired coverage. More enhanced features, such as automatic placement of the base units to achieve defined coverage goals, are left for future work. We can use a hard threshold coverage function that outputs one when backscatter signal power is above RX sensitivity and the carrier interference is below the RX blocker tolerance, and zero otherwise, or a soft threshold coverage function that transitions smoothly between zero and one.

We use our simulator to plot the backscatter signal power in a 900 sq^2 two-bedroom apartment unit in two different cases, a single RX - two TX (Fig. 4.8(a)), and a single RX

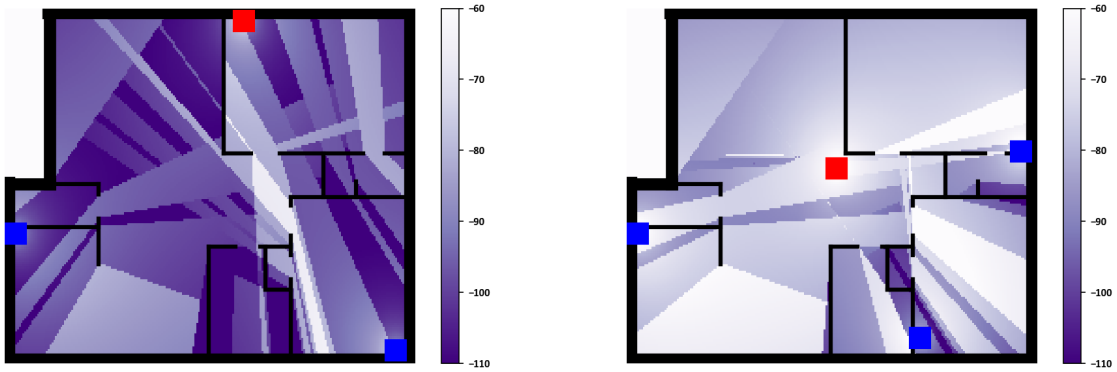

(a) One RX and two TX units

(b) One RX and three TX units

Figure 4.8: Simulating the backscatter signal power for a two-bedroom apartment using the deployment planning tool.

- three TX (Fig. 4.8(b)) configurations, where a brighter color shows a stronger backscatter signal power. In this simulation, we assume all devices use antennas with 0 dBi gain, and frequency band, carrier power, backscatter conversion loss, path loss exponent, and attenuation through internal walls are equal to 915 MHz, 25 dBm, 4 dB, 2 and 15 dB, respectively. The results clearly show that adding one more TX unit and placing the base units appropriately have a significant effect on the performance of the MultiScatter system.

During our evaluations (Sec. 4.6), we notice that placing the base units closer to walls or other large objects could improve backscatter performance. The strong multipath resulted from such large objects could help the backscatter systems by creating a frequency-dependent non-flat attenuation profile, resulting in enough operative frequency bands for backscatter communication. Improving the simulator to model these higher-order effects and creating a more accurate coverage map is left for future work.

4.4 Sensor Node Design

Our goal is to design a battery-free sensor node platform that can accommodate different sensors and communicate with the base units. We reduce the wireless power consumption of

the sensor node by using low-power backscatter for the sensor node uplink and an ultra-low-power wake-up radio for the sensor node downlink. The wake-up radio allows the sensor node to stay in idle mode until the base units activate it. We also implement a gating technique to reduce the energy burden of power-hungry sensors by adding low-power auxiliary sensors. For example, a motion sensor is used to gate the operation of the camera. Finally, we use a low-power micro-controller with several communication protocols in our sensor node platform, which can interface with various commercial sensors.

FSK Backscatter. The sensor node transmits the data to the RX unit using Frequency-Shift Keying (FSK) backscatter communication. In FSK backscatter, bits '0' and '1' are transmitted by changing the state of the RF switch connected to the antenna at frequencies f_0 and f_1. This results in a backscatter packet with $(f_0 + f_1)/2$ subcarrier modulation and $|f_0 - f_1|/2$ frequency deviation.

We use a temperature-compensated VCO to generate the variable frequency signal that controls the RF switch. We use two NMOS switches to control the resistor that sets the oscillator frequency, as shown in Fig. 4.9. Switch Q1 controls the backscatter subcarrier modulation frequency, and switch Q2 sets the transmitted bit to '1' or '0'. We use the micro-controller SPI interface derived by the MCU oscillator to generate accurate bit periods. Compare to using two individual oscillators to generate f_0 and f_1 frequencies [198], using a single controlled oscillator to generate both frequencies reduces the power consumption and ensures phase continuity in switching between the two frequencies.

Low Idle Power Consumption. The sensor node operates in the idle mode until it is activated by the base units to enable one of its sensors or report its latest recorded data. Therefore, our sensor nodes must be power efficient in the idle mode. Although the FPGAs allow us to implement custom communication protocols, they consume more power in the idle mode than the MCUs. We use a low-power MCU with several low-power idle modes in this work.

To wake up the MCU from the idle mode, we use a low-power and low-frequency wake-up

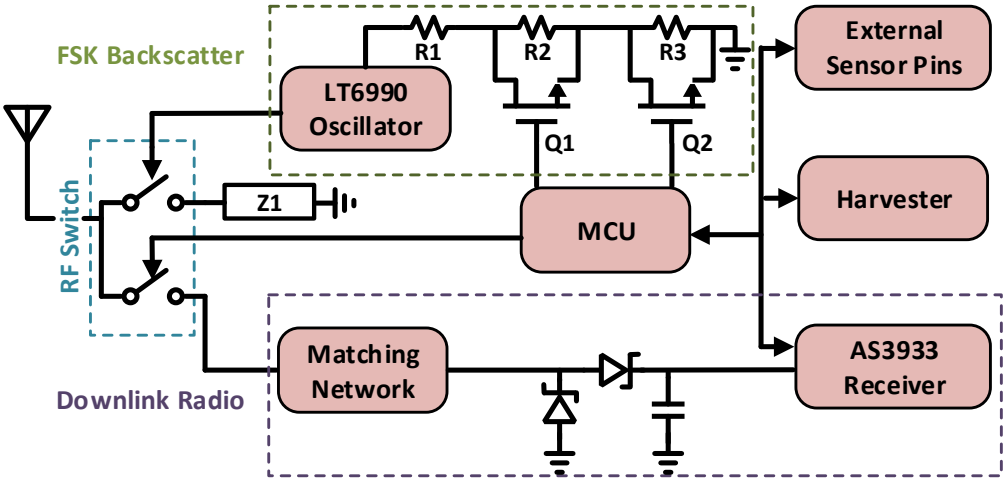

Figure 4.9: Sensor node block diagram.

radio [119]. While the MCU is in the idle mode, the wake-up radio listens to the packets transmitted by the TX units. If the received packet matches the sensor node's 16-bit ID, the radio generates an interrupt to the sensor node MCU and passes the received command to it.

Sensor Gating. We use low-power auxiliary sensors to gate the operation of the power-hungry sensors. For instance, a motion sensor can enable the operation of an image sensor when there is movement in the room. This helps us reduce the power consumption of the sensor node by limiting the operation of the power-hungry sensor (image sensor) to informative events. Similarly, the microphone activates only when the sound intensity passes a defined threshold.

We also implement second gating criteria by monitoring the energy storage element of the sensor node. The MCU measures the voltage of the energy storage element and sends it back to the base units in response to each sensor enable command. The base units monitor this voltage and use it to gate the commands issued to the sensor node. If the voltage falls below a defined threshold, the base units bypass the sensor reading requests from that sensor node and allow the energy harvesting unit to charge the storage element. The base units continue to monitor the energy storage voltage with a more extended reading period and

resume regular operation once the voltage reaches a certain level.

Energy Harvesting and Storage. The energy harvesting unit of the sensor node collects energy from ambient light and stores it on an energy storage element. The energy storage element connected to each sensor node should store enough energy to support reading the physical sensors connected to the sensor node and transmitting their data to the base units. While supercapacitors have longer life cycles and can be employed to build truly battery-free sensor nodes, rechargeable batteries have higher energy capacity and can tolerate longer energy drought periods [210, 167]. Our energy harvesting unit can work with both types of energy storage elements.

Modular Design. We follow a modular design approach to building our sensor nodes. The MCU, wireless communication units, temperature, humidity, and illuminance sensors are placed together as the basic sensor node. The energy harvesting unit, camera, and microphone sensors are designed as add-on boards that mount on top of the basic sensor node through 5 power and 12 Input/Output (IO) pins (see Fig. 4.10(c)-(e)). The modular design allows us to support more sensors without redesigning the communication section.

4.5 Implementation

We implement MultiScatter, consisting of the RX base units, TX base units, and sensor nodes, for operation in 902-928 MHz ISM band on 4-layer FR4 PCB. The system uses FSK modulation and 802.15.4g packet structure with seven preamble bytes, 16 CRC bits, and no whitening for communication between devices.

4.5.1 Base Units

Receiver Units. The RX unit has two parts, a communication board with the CC1352R [41] wireless MCU, and a Raspberry Pi 4B single-board computer (RPi) with 2GB RAM for processing and backhaul. The two boards are connected to each other, as shown in Fig. 4.10(a), and communicate through a 1Mbps serial link. The CC1352R supports FSK modulation with

data rates from 0.3 to 1985 Kbps and RX filter bandwidths from 4.3 to 3767 KHz. The RX filter bandwidth determines the carrier attenuation and should be set accurately considering the data rate, frequency deviation, and subcarrier modulation frequency. Our CC1352R board consumes 30 mW for its operation on average. The RPi board runs the Raspbian operating system. It processes the received data from the sensor nodes and determines the activation packet parameters. The RPi sends out this information to the CC1352R MCU to start the communication cycle, and the CC1352R MCU passes the received backscatter packets to the RPi as they are received. We implement the data handling and communication protocols explained in Sec. 4.3 using Python 3.7, which runs on the RPi.

Transmitter Units. Each TX unit consists of a CC1312R [40] sub-GHz wireless MCU that receives the activation packet and generates the carrier signal, and a SKY65313-21 [21] power amplifier (PA) that amplifies the carrier signal up to 28 dBm. Our TX unit consumes up to 3.3 W while transmitting carrier at 28 dBm and its ground planes distribute the heat generated by the PA to limit the PA surface temperature to $65°C$. Fig. 4.10(b) shows the fabricated TX unit.

Server. One of the RX units also handles the server tasks. We use the python socket.io protocol [50] to handle the communication between the RX units and server.

Data Collection Scheduling. The data collection process from each sensor initiates when the sensor node marks the availability of new data or when a pre-defined timeout is reached. The data collection might take one or several iterations. At each iteration, the RX unit first checks all the ongoing data collection processes for completion. If a portion of the data is missing, the RX unit generates the commands to read the missing parts and stores them in a queue. Next, all the commands in the queue are executed, and the responses to each command are processed. Once the queue is empty, the iteration is completed. We use time-division multiple access to accommodate multiple sensor nodes. Each sensor node has a unique ID, and only one sensor node responds to the command from the RX unit at each cycle.

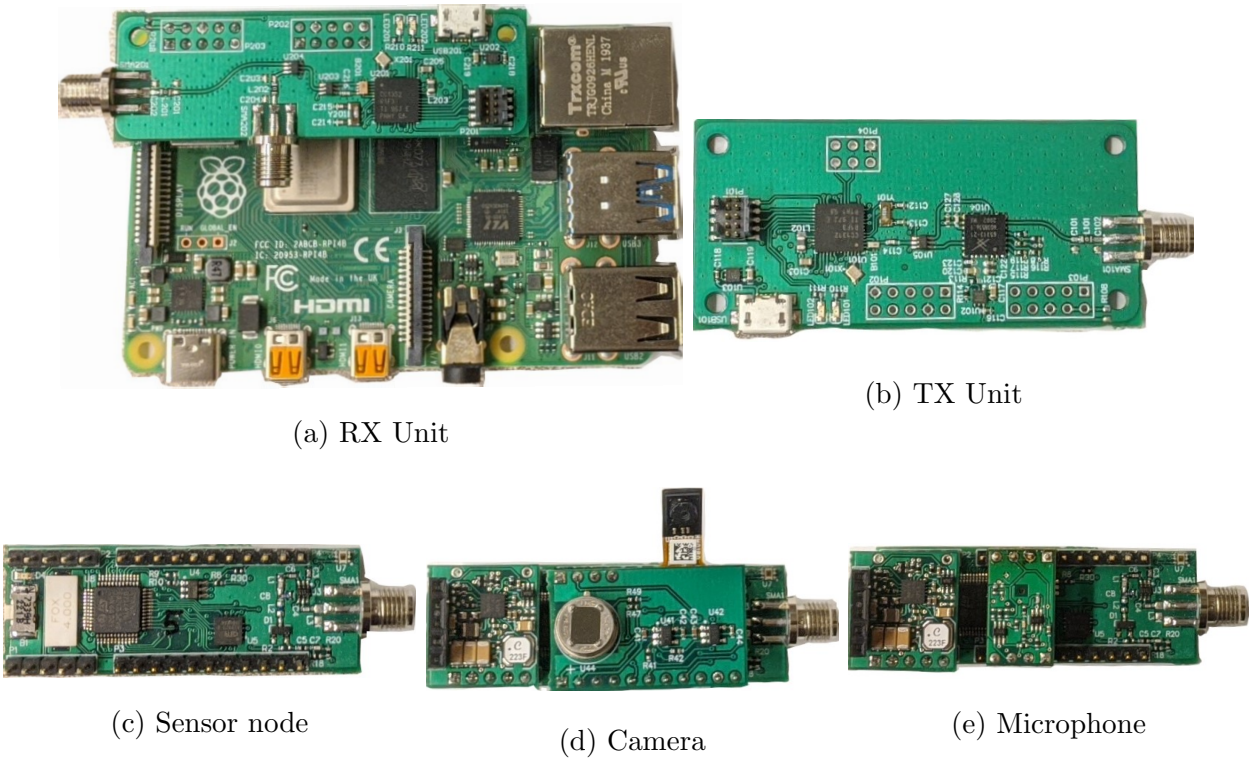

(a) RX Unit

(b) TX Unit

(c) Sensor node

(d) Camera

(e) Microphone

Figure 4.10: Prototype hardware.

Cost Analysis. We design MultiScatter intending to reduce the infrastructure cost of a wide area backscatter network. Our analysis using pricing data from Octopart [1] shows that at low volumes of 1,000 units, the TX and RX base units cost $16.1 and $49.6 (including $35 for the RPi), respectively. The number of base units required to cover a specific building depends on its floor plan. We provide two sample cases in Sec. 4.6.

4.5.2 Sensor Node

We select STM32L071C8 [35], an ultra-low-power ARM Cortex-M0+ MCU with 20 KBytes RAM, as the sensor node MCU. The memory capacity is enough to store one image frame or one second of audio recording. A 4 MHz external crystal generates the MCU clock. We use AS3933 [10] wake-up radio for downlink, and LT6990 [45] VCO for generating the backscatter

uplink signal. The sensor node is also equipped with HDC2080 [31] humidity and temperature sensor, and opt3002 [16] ambient light sensor. The sensor node is powered up using a 2.5 V regulator. We set the MCU core voltage to 1.2 V to reduce its power consumption. The antenna is shared between the wake-up-receiver downlink and backscatter uplink via the AS213-92LF [6] RF switch, as shown in Fig. 4.9. A 47 pF capacitor is chosen for $Z1$ (see Fig. 4.9), which has a small impedance at the carrier frequency.

The sensor node supports four uplink data rates, 31.25 Kbps, 62.5 Kbps, 125 Kbps, and 250 Kbps. We use 1 MHz subcarrier modulation with 25 KHz frequency deviation for the two lower data rates, and 1.79 MHz subcarrier modulation with 80 KHz frequency deviation for the two higher data rates, by setting the values of R1, R2 and R3 to 26.7 KΩ, 22.1 KΩ and 2.5 KΩ, respectively.

In each communication cycle, the sensor node receives a one-byte command from the base units. Some commands invoke an action, such as taking a picture, while others request specific information, such as a portion of the recorded image. The sensor includes the received command in its response to the base units for verification.

Energy Harvester. We design the energy harvesting unit with the BQ25570 IC [29]. We use AM-1801 and AM-1816CA solar panels, designed for indoor operation with areas of 2 in^2 and 17 in^2 respectively [46], to supply the energy harvester board. The energy harvested from the solar cells is stored on a 100 mF super-capacitor [38] to support sensors such as a camera and a microphone.

Camera. We use a Himax HM01B0 image sensor [32] running in 120×120 *pixel* QQVGA mode as the main sensor, and a Panasonic EKMB1104111 motion sensor [8] as the auxiliary gating sensor. Once the motion sensor is activated, or a take-picture command from the base unit is received, the MCU turns on the image sensor and enables its internal Phase-Locked Loop (PLL) to generate a 3 MHz clock for the image sensor. Once an image is captured, we turn off the motion sensor to avoid image overwrite and inform the base unit that an image is available. For data transmission, we divide one image into 12 large sections or

120 small sections, and the base unit can request a large or small section with a dedicated command to complete reading the image. Once the base unit successfully receives the image, it re-activates the motion sensor.

Microphone. Our microphone board is designed with a VM1010 microphone sensor [37]. The microphone has two operational modes, wake-up sound mode, and normal mode. In wake-up sound mode, which we use to gate the normal mode, it waits for an acoustic event to trigger the normal mode. The microphone records data for 1 second at 8 KS/s in normal mode. Transition between gating and normal modes and data transmission are similar to the camera.

Size and Cost Analysis. While we use commercial-off-the-shelf components to build our sensor node, recent works on integrated energy harvesters [84, 169], wake up radios [179, 153], and backscatter radios [202] clearly show the feasibility of integrating all electronics sections of our backscatter sensor node in an ASIC to significantly reduce its size and cost. In this case, the sensor node cost and size would be limited by the energy harvesting (i.e., solar cell) and the energy storage (i.e., supercapacitor) elements. In this work, we use a 100 mF supercapacitor to support sensors such as cameras and microphones. However, a 3.2 mm $\times$ 2.5 mm, 47 µF capacitor stores enough energy to read the low-power sensors such as temperature and humidity sensors and transmit the data via a backscatter packet 3 times. Furthermore, recent advances in solar cell design [156] have shown 4.5 $\times$ energy harvesting efficiency under indoor lighting conditions compared to the solar cells used in this work, which means a 0.45 in^2 solar panel would generate enough energy to power up our sensor node.

Energy Efficiency. The sensor node consumes 2.26 mW while transmitting backscatter packets, which is comparable to the commercial Sub-GHz active radios. However, we should note that this prototype is built with COTS components, while the commercial active radios are specifically optimized for low-power operation. Our evaluation in section 4.6 shows that the MCU consumes 74% of the energy in backscatter mode, which highlights the vast

potential for improving energy efficiency by designing backscatter ASICs.

4.6 Evaluation

We perform several experiments to demonstrate the performance of the MultiScatter system. First, we measure the power consumption of the sensor node with the camera module and evaluate the maximum sensor update rates using two solar cells with different sizes. Next, we evaluate the communication range of our system in line-of-sight and demonstrate the scalability of our solution in covering a two-floor educational complex. We verify the accuracy of our planning tool by comparing its outputs with measurements taken in an apartment unit. Also, we examine how deploying multiple RX and TX units affects the achievable aggregate throughput of the system. Finally, we show the handover performance when sensor nodes move in the network. We use omnidirectional whip antennas [5] for all devices in our evaluations.

4.6.1 Power Consumption

We evaluate the sensor node power consumption using the camera module since it is the most power-hungry sensor. Our setup consists of one RX-TX pair and a sensor node operating at 250 Kbps. Fig. 4.11(a) shows the measured power that the camera consumes while capturing and transmitting one image.

The operation of the camera starts in the idle mode, where it consumes 39 µW on average. At time = 0.06 second, the sensor node is activated to take a picture and transfer it to the MCU. This process takes 1.2 second, and the average power is 5.04 mW. MCU PLL operation at the start and end of the process causes peaks in the power plot. Next, the RX unit requests transmission of the first section of the image, marked with the blue rectangle in Fig. 4.11(a), at time = 2.1 second. This is followed by requests for transmission of the other 11 sections to complete the picture. The image transmission takes 1.69 second, and the average power during this time is 2.26 mW.

Fig. 4.11(b) breaks down the energy that the sensor node consumes in transmitting a

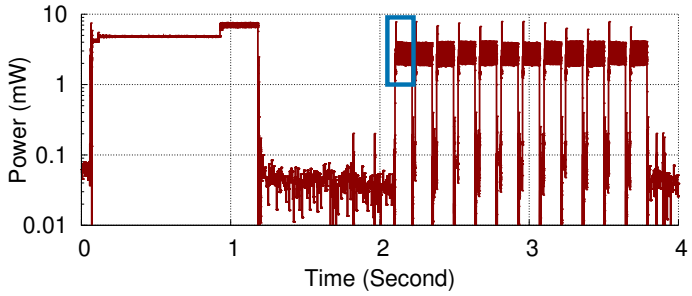

(a) Camera power consumption during one image

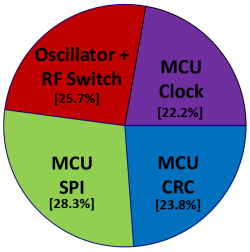

(b) Backscatter packet energy breakdown

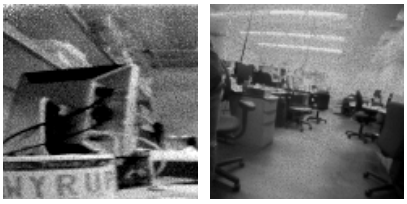

(c) Sample images

Figure 4.11: Battery-free camera evaluation results.

38 byte backscatter packet. The MCU core consumes 23.8%, and 28.3% of the total energy (4.21 µJ) during CRC calculation and data transfer, while the MCU clock accounts for another 22.2%. The LTC6990 oscillator plus the RF switch consume the remaining 25.7%. In our prototype, the MCU consumes three-quarters of the total energy in backscatter mode, highlighting the vast efficiency potentials in designing custom ASICs for backscatter sensor nodes.

Fig. 4.11(c) shows sample images captured by battery-free camera.

4.6.2 Energy Harvesting

We use AM-1801 and AM-1816CA solar panels to supply the energy harvester board and evaluate the battery-free sensor nodes update rates. We set up the solar-powered sensors in an office building with fluorescent ceiling lights. The illuminance at the surface of the solar

Table 4.1: Power consumption measurements for camera, microphone, and environmental sensors.

Measurement		Cam.	Mic.	Env.
Idle Power (µW)		39	51	25
Sensing Energy (mJ)		6.05	3.51	0.025
Communication Energy (mJ)		3.82	2.84	0.014
Solar-Powered Update Rate (Sec.)	2 in^2 panel	280	268	1
	17 in^2 panel	17	11	0.2

cell is 300 lux. We record data for 6 hours using each solar panel and sensor. Table 2.1 lists the achieved average update rates using each solar panel, as well as the idle power consumption, sensing energy, and communication energy for each sensor. Our evaluation shows that the sensing energy is 62%, 56%, and 65% of the total consumed energy for the camera, microphone, and environmental sensors, respectively, which shows that the sensing energy is the most power-consuming part of the sensor and limits the sensor nodes update rate.

The 2 in^2 solar cell can provide enough power for the operation of the camera and microphone sensors every 280 and 268 seconds. This is made possible by reducing the sensor node power consumption in idle mode using the gating sensors. We can increase the camera and microphone update rate to 17 and 11 seconds by using the larger solar panel. The sensor node 100 mF super-capacitor stores enough energy to transmit 21 images or 36 seconds of audio with a single charge (3.6 V-4.5 V).

The small solar cell supplies enough energy to read the environmental sensors, which include the temperature, humidity, and illuminance sensors, every second. The system in [14] uses the CC2650 wireless MCU to read a temperature and humidity sensor and transmit the result via a BLE packet. The evaluation in [14] shows that the setup consumes an average of 4.04 mA from a 3 V battery over 30 ms which results in a total energy consummation

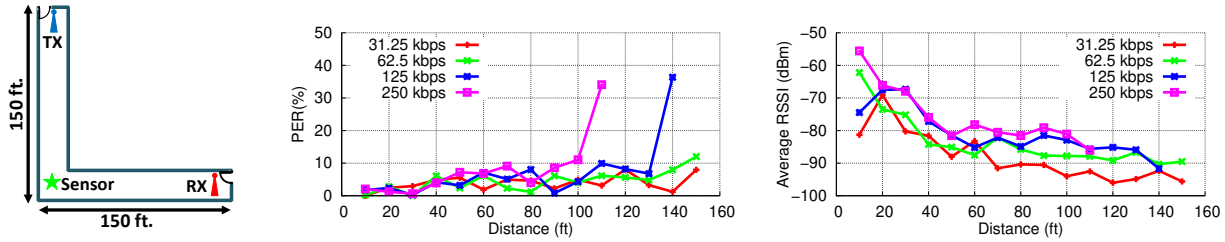

(a) Experiment setup. (b) PER vs Distance. (c) RSSI vs Distance.

Figure 4.12: Line-of-sight communication range.

of 363.3 µJ per measurement transfer. This energy includes the energy required to wake the MCU from the low-power mode, communicate with the sensor, activate the radio, and transmit the data. In comparison, our sensor node consumes 39 µJ per measurement transfer, which is 9 × lower than the BLE packet transfer implemented in [14].

4.6.3 Range

We set up the system in a 300× 5 ft hallway with floor plan shown in Fig. 4.12(a) to evaluate the communication range of the MultiScatter system in line-of-sight. The sensor node is in the middle of the hallway (indicated with the green star). In each measurement, we place the RX and TX units at the same distance from the sensor node and measure the Packet Error Rate (PER) of backscatter communication over 1000 packets. We place the sensor node at the same distance from TX and RX units since it is the most challenging setup in backscatter deployments [121, 117]. If the sensor is placed closer to one base unit, the other base unit could be placed further away while maintaining the same PER. Fig. 4.12(b) shows the PER for four data rates as we increase the RX and TX distances from the sensor node, from 10 ft to 150 ft. Our results show that the MultiScatter system can operate up to 150 ft (length of the hallway) at the data rate of 31.25 Kbps (PER $< 10\%$) with an average RSSI of -95 dBm. The maximum achievable range reduces to 100 ft when the sensor node transmits data at 250 Kbps with the RSSI of -80 dBm.

(a) Ground Floor.

(b) First Floor.

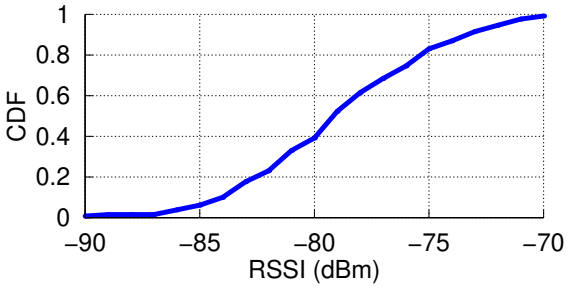

(c) RSSI CDF.

Figure 4.13: Backscatter coverage in a two-floor educational complex. RX units, TX units and tested sensor node spots are shown with red squares, blue squares and green circles, respectively.

Fig. 4.12(c) shows that the RSSI values at 10 ft for 31.25 Kbps and 62.5 Kbps data rates are less than the next several measuring points, although the distance is increasing. This happens due to the carrier power tuning in the MultiScatter system, as explained in Sec. 4.3.1. At this short distance between the devices, the backscatter link achieves low PER with lower carrier power.

4.6.4 Coverage

To evaluate the performance of MultiScatter in a non-line-of-sight scenario, we set up the system in a two-floor educational complex, covering multiple rooms separated by glass and

wood doors, as well as concrete walls, with a total area of 23400 ft^2. Fig. 4.13(a) and (b) show the floor plan of the ground and first floor of the building. In our setup, we have 5 RX units (red squares) placed at the height of 3 ft from the floor, and 20 TX units (blue squares) attached to the concrete walls at 6 ft height. This combination of base units costs $569 at low volumes based on our cost analysis (see Sec. 4.5). We place the sensor node at 5 ft height and move it between 130 test points (green circles), while it communicates with the base units at 125 Kbps. The sensor node transmits 1000 backscatter packets at each test point, and we measure the PER and RSSI of the backscatter packets. Our results show that all test points have PER less than 15 %, and the median of RSSI is -77 dBm (Fig. 4.13(c)), which demonstrates that our system is fully capable of covering the entire building.

Also, we evaluate the performance of MultiScatter in a 34.5 $ft \times 21$ ft single bedroom apartment (Fig. 4.14(a)). We use our deployment planning tool to determine the location of base units. To verify our tool model, we repeat the experiment using one RX unit and one to three TX units. In each test, we move the sensor node to 18 points around the apartment and calculate the PER over 500 packets. Fig. 4.14(b)-(d) show the simulated backscatter coverage using a soft threshold coverage function, where the darker points have a higher chance for successful backscatter coverage. The measured PER at each of the selected points is also specified in the figures. Our experiment results verify that our planning tool is a close estimate of the measured coverage.

4.6.5 Throughput

We deploy 5 RX, 20 TX, and 10 sensor node units operating at 125 Kbps in the building shown in Fig. 4.13 to evaluate the performance of MultiScatter in a multi-RX multi-TX scenario. The RX and TX units are placed as shown in Fig. 4.13(a) and (b), while the sensor node location is shown in the same figures with numbers 1 to 10. In this experiment, we assign two sensor nodes to each RX unit, select a subset of the sensor nodes with 1 to 5 members, command them to transmit data to their assigned RX units, and measure the achieved data rate at each RX unit. To calculate the aggregate throughput, we add up the

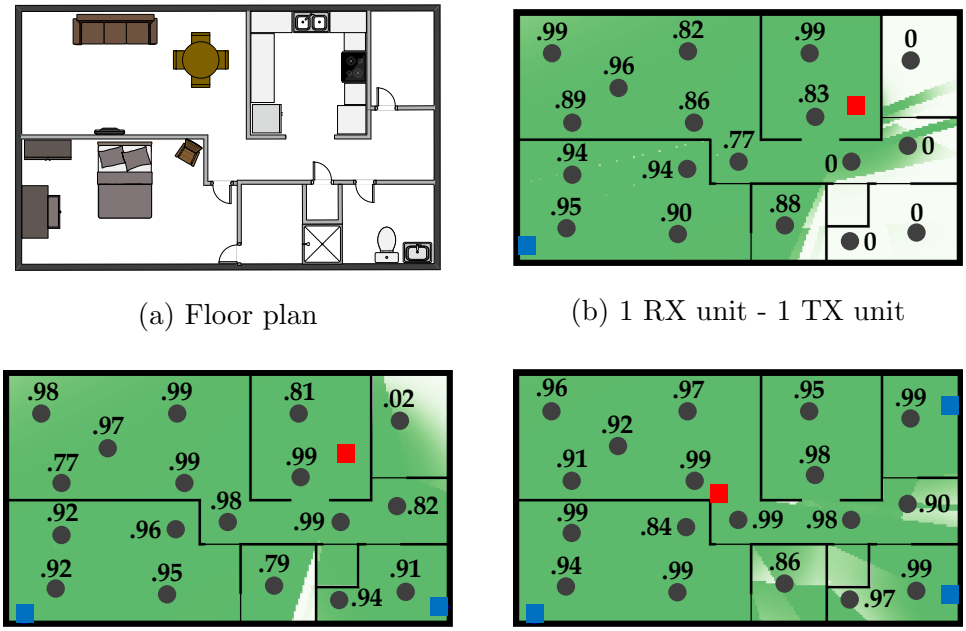

(a) Floor plan

(b) 1 RX unit - 1 TX unit

(c) 1 RX unit - 2 TX units

(d) 1 RX units - 3 TX units

Figure 4.14: Verifying the planning tool in a single bedroom apartment coverage. The simulated coverage map, shown in green in three different cases, is a close estimate of the measured PER results at 18 different points around the apartment.

individual throughput of all RX units involved. Each point in Fig. 4.15 shows the results of one measurement, where the numbers in the parenthesis indicate the location of the sensor nodes involved in the measurement.

Our results in a single RX setup show that the maximum achievable throughput using one sensor node is 90 Kbps. All sensor nodes achieve a throughput close to this nominal data rate when they operate alone. Comparing the nominal data rate to the physical data rate of 125 Kbps shows a 28 % overhead. Our analysis shows that 10 % of this overhead is caused by the TX activation and sensor wake up in the communication cycle. The other 18 % is due to wasted time interval between backscatter packets.

The aggregate throughput of the network also increases linearly as the number of RX units and sensor nodes in the measurement increases. The measurement with sensor nodes

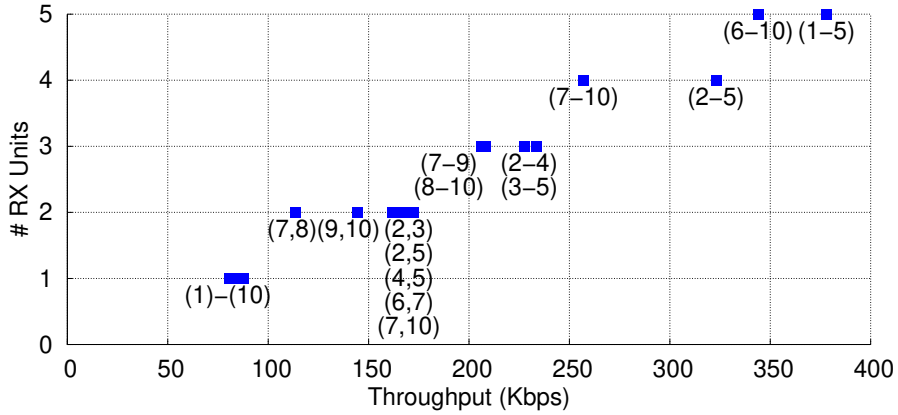

Figure 4.15: Aggregate throughput with multiple RX units.

placed at locations (1-5) achieves an aggregate throughput of 375 Kbps using 5 RX, which is 4.17 × faster than a single sensor node. This result shows that multiple backscatter sensor nodes can operate simultaneously and share the spectrum resources among themselves.

In cases where two close sensor nodes communicate with two different RX units, such as (7,8) and (9,10), we observe a lower aggregate throughput compared to the cases where sensor nodes are placed further away from each other, such as (2,3) or (7,10). Our analysis shows that this is mainly due to interference in waking up the sensor nodes since the sensor node wake-up radio uses amplitude modulation , which is more susceptible to interference. The second factor affecting the throughput is the interference caused by the carrier signals from other backscatter links. As the number of RX units increases, the number of simultaneous carrier signals increases too which contributes to data loss, especially where the sensors from multiple RX units are deployed near each other.

Although we test with a maximum of ten sensor nodes due to the limited hardware we have at our disposal, there is no strict limitation on the number of sensor nodes in the proposed network stack. We use 16-bit IDs for the sensor nodes in this work which limits the number of sensor nodes to 65535, but that limitation can be relaxed by using 32-bit IDs. In the current implementation, each backscatter cycle takes a minimum of 10ms. Therefore, each RX unit can communicate with up to 100 sensor nodes each second.

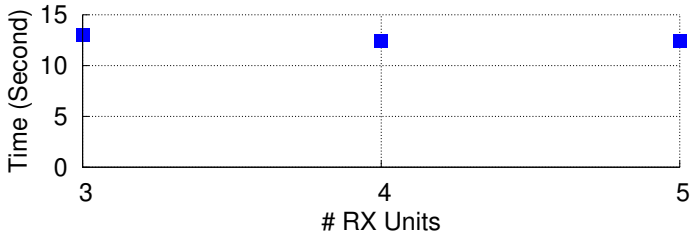

Figure 4.16: Handover duration.

4.6.6 Handover

To demonstrate that MultiScatter can manage the movement of sensor nodes between RX units, we set up the system in an office building with three isolated rooms, walk within these rooms at an average pace while carrying the sensor node. We repeat the experiment 10 times for each scenario where the system uses 3, 4, and 5 RX units and 2 TX units for each RX unit. We use a threshold of 20 consecutive dropped packets in all three measurements.

Our results in Fig. 4.16 show that the average time difference between the last successfully received packet at the previous location and the first one at the new location is 13, 12.4, and 12.4 seconds when our setup has 3, 4, and 5 RX units, respectively. This time includes both the relocating time, 8.2 seconds on average, and assigning a new RX unit to the sensor node placed in the new location. This result suggests that the RX assignment process is not significant compared to the movement time in our experiments, and once the sensor node is settled in its new location, the network successfully reassigns it to a new RX unit.

4.7 Case Study: Occupancy Detection

We used the MultiScatter system in an experimental case study for occupancy detection [109, 181, 120]. The system setup consists of two sensor nodes equipped with camera sensors, a TX unit, and a RX unit. We tested the system at two indoor locations, a residential unit, and a computer lab. During the system testing, the cameras are installed in each zone to capture images from different directions and angles. For privacy concerns, the system is only set up in the common areas such as the kitchen and the living room in the residential

unit. These selected testing locations are chosen to provide diverse indoor testing scenarios. For example, in the kitchen, occupants are often standing and walking as they are cooking or cleaning the dishes, while in the living room, occupants are usually sitting on the couch watching television or using their laptops. These scenarios produce images with different human postures, lighting conditions, and occupants' distance to the camera (human figure size in pictures), enabling a more comprehensive system performance evaluation.

In each location, we run the system for $\sim$10 hours from sunrise to sunset, with $0 \sim 2$ occupants in the zone throughout the experiment period. Moreover, to evaluate the reliability of the system, a final experiment is performed with an extended period, where we run the system uninterrupted for *5 days*, with the camera nodes installed in two zones (kitchen and living room) simultaneously. This experimental setup allows the system to cover a large area in the residential unit, with up to a $\sim$30 ft euclidean distance between the receiver and camera sensor nodes.

To detect human presence, we implement a recent state-of-the-art detection algorithm, YOLOv5 [112]. The models are introduced with four different sizes; small (s), medium (m), large (l), and extra-large (x), with the model sizes sorted in ascending order. The model sizes are increased by increasing the model height and width multiplier, which will increase the number of layers and layer channels. Considering the small input image size and the limited computation resources on Raspberry Pi, we choose the s model with a 0.33 height multiplier and 0.5 width multiplier for our application. The resulting model weight is merely 14 MB with 7.25 M parameters and 16.8 GFLOPs in the model.

Collected images by the cameras are labeled and annotated with bounding boxes around the occupants. We employ several data augmentation techniques such as brightness varying, image flipping, and mosaic data augmentations to generate a richer training image variation. These data augmentations procedures are essential to enhance the robustness of the trained model to various scenarios such as different illuminance levels and human position in the images. For this single-class detection implementation, we generate up to 4,308 images after augmentations(excluding mosaic augmentation), and we use 3,016 images for training, 430

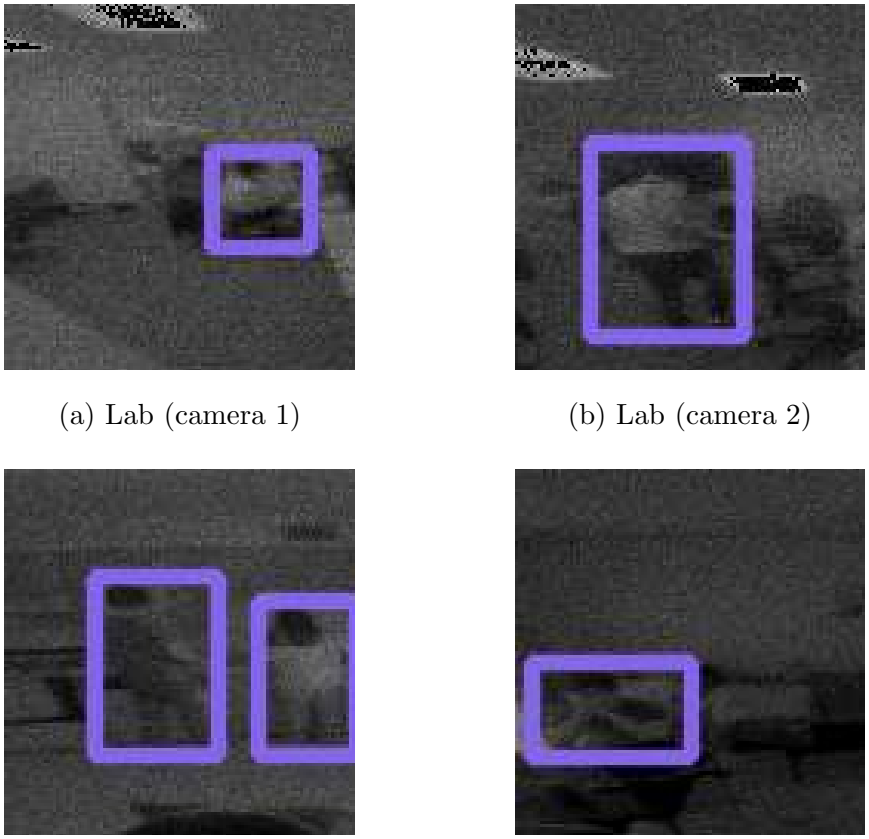

(a) Lab (camera 1)

(b) Lab (camera 2)

(c) Kitchen

(d) Living Room

Figure 4.17: Example occupancy detection results for each experiment zone.

images for validation, and 862 images for testing. In the next step, these images are fed into the YOLOv5 network for model training. The model is trained on Google Colab using a Tesla T4 GPU for 300 epochs. After training the model, the model weight and architecture are saved for inferencing purposes. The model weights are first converted into Tensorflow Lite (TF-Lite) format before deploying the saved model on Raspberry Pi.

4.7.1 Experiment Results

Fig. 4.17 shows four sample images collected with MultiScatter wherein the YOLOv5 model detects occupants and annotates them with bounding boxes. Each example image shown

Zones	**Total Num. Images**	**Accuracy(%)**
Lab	2,951	99.56
Kitchen	3,508	99.72
Living Room	3,082	92.53
Kitchen and Living Room (5 days)	32,914	92.72

Table 4.2: The total number of camera images collected and detection accuracy rates for different testing locations.

in the figure depicts a different zone/background or posture. For example, in Fig. 4.17(a), the image shows the person in a sitting position and far away from the camera. In contrast, another camera at the same location captures a picture of the person walking toward the door from a different angle. The model can detect the person in both scenarios despite the different posture and distance from the camera. Moreover, in Fig. 4.17(c), the image shows that our model can detect multiple people in one image. Finally, in Fig. 4.17(d), the image shows a scenario where the occupant is looking at the laptop in the living room with only the top half of the body visible. This example shows that the model can detect the person despite the occlusion of the lower half body and it is robust to a small angle of depression.

On top of the output illustrations, Table 4.2 also provides a summary of the outcome of the performed experiments. In each zone, the camera captures and inferences up to ∼3,000 images, and in the last experiment, the system records more than 30,000 images, with an inference time of only ∼100ms per image. To simplify results presentation, we use a 0.5 confidence threshold in the inferencing, and each frame with a detected person(s), will be labeled as *occupied*, and otherwise, as *unoccupied*. After evaluating these occupied and unoccupied frames, each experiment achieves an accuracy of $> 90\%$, including the last experiment with two zones and an extended experiment period. This shows that the

MultiScatter system can be used to collect data to accurately detect human presence and operate reliably in a large area for a long duration.

4.8 Related Work

Our work is related to prior efforts in backscatter communication, and battery-free sensing.

Backscatter Communication. Our work builds on recent efforts in advancing bistatic backscatter solutions to deliver ultra-low-power wireless connectivity. These efforts were focused on designing backscatter solutions compatible with existing wireless standards [90, 208, 119, 125, 108, 53, 213, 209, 141, 190, 163, 101], and improving backscatter throughput [146, 106, 215, 218], range [190, 198], reliability [177, 119] and deployability [94, 122]. While these works use a single RX-TX pair in their deployments, we use multiple RX and TX base units to realize wide area and scalable bistatic backscatter.

A wireless protocol to handle the concurrent transmission of backscatter devices was presented in [106], which uses chirp spread spectrum modulation to share the channel bandwidth between many devices communicating with a single monostatic backscatter access point. The access point can cover a wide area since each backscatter node has a low data rate that allows the backscattered signals to be recovered at very low signal powers. Using a single access point is not a scalable solution. In this work, we use a network of backscatter base units to extend the coverage at data rates up to 250 Kbps. Although we use 802.15.4g standard with FSK modulation and time-division multiplexing in this work, the techniques presented can be combined with other modulation and multiple access methods.

A scalable backscatter sensor mesh was introduced in [214] that uses distributed excitation to enable multi-hop backscatter between sensor nodes. Although this solution enables the sensor nodes to communicate with each other at longer distances, it requires an excitation source close to each sensor node resulting in significant deployment limitations. In our architecture, the sensor nodes only communicate with the base units. The network of base units handles the tasks that allow the sensor nodes to move freely inside the coverage area without adding any complexity to the sensor nodes.

Battery-free sensing. Battery-free solutions rely on the harvested energy from RF [182, 158, 191, 180, 157], solar [199, 152, 83], vibration [160, 140], motion [187], thermal [152] and magnetic [104] energy sources for their operation. [212] lists mean energy generated by 50 activities in residential buildings. Applications such as video [180, 105, 113] and audio [191] streaming, gaming [83], full-body temperature mapping [104], food quality monitoring [168], pulse oximetry [129, 204], structural health monitoring [147], flying insects EMG telemetry [194], indoor acoustic localization [216], eye-tracking [139], visible light sensing [199] and many others [187, 143, 134, 103, 137] have been realized with battery-free platforms. In this work, we develop a modular battery-free sensing platform based on bistatic backscatter wireless communication, and use camera, microphone and environmental sensors as examples to show the platform capabilities.

4.9 Conclusion

We present the first wide-area multistatic backscatter network for battery-free wireless sensors. We discuss the limitations of backscatter systems, such as the limited coverage area, frequency-dependent operability, and sensor node limitations in handling network tasks. Our MAC layer implementation is designed to overcome these limitations by selecting the best RX-TX pair, carrier power, and frequency in communicating with each sensor to maximize the throughput and handling the handover between base units as the sensor moves inside the coverage area. We build low-cost hardware using COTS components and prototype proof-of-concept battery-free sensors for capturing images, audio, and environmental data.

Chapter 5

CONCLUSION

In conclusion, this dissertation presents backscatter communication solutions that address challenges in achieving ubiquitous sensing. We designed a full-duplex backscatter reader to simplify the deployment of backscatter sensor nodes. We configured a low-power reader and showed that it can be integrated with mobile phones or mounted on drones to enable new applications. We investigated the reliability challenges of bistatic backscatter deployments and offered a closed-loop configuration selection algorithm to maximize the reliability of backscatter links in multipath-rich indoor environments. Building on this work, we presented a backscatter network architecture where multiple receivers and transmitters base units are employed to deliver backscatter connectivity to many battery-free sensor nodes over a wide area.

The work presented in this dissertation can be followed up in the future along these directions.

Low power wake-up radios. The backscatter technique reduces the energy required to transmit data from low-power sensor nodes. However, these nodes also need receivers to get network commands and settings. The passive envelope detection receiver presented in chapters 3 and 4 consumes 2.3 µA in listening mode and achieves a sensitivity of -43 dBm. For a backscatter system with carrier source P_{TX} and receiver sensitivity RX_{sen}, the sensitivity of wake-up radio at least should be better than $(P_{TX} + RX_{sen})/2$ since the backscatter signal propagates twice, but the wake-up signal only propagates once. Although the envelope-detection-based wake-up receiver can satisfy this requirement in most designs, it still suffers from several drawbacks. First of all, a better sensitivity receiver relaxes the deployment of backscatter nodes and makes sure that the wake-up receiver is not the communication

bottleneck. Furthermore, these receivers are susceptible to interference since they do not have any channel filter, which makes designing a large network with many backscatter nodes challenging. Recent works have proposed new architectures for improving the wake-up radio receivers, especially in backscatter systems [164, 116, 138]. Yet, ultra-low-power wake-up radio architectures remain an open research problem.

Energy harvesting. The backscatter sensor node designs presented in this thesis can be powered using batteries or energy harvesters that convert motion, vibration, light, EM radiation, or thermal energy into electrical energy. In chapter 4, we demonstrated how a small 2 in^2 solar cell can power up a sensor node to transmit one packet with temperature, humidity, and illuminance data each second. Also, our simulation result in chapter 3 confirms that application-specific integrated circuits (ASIC) solutions for backscatter communication further lower the barrier in designing self-powered sensor nodes. The energy source selection for backscatter nodes mainly depends on the application. Several factors including solution cost, form factor, output power, efficiency, and expected lifetime should be considered in designing energy harvesters. Low-cost energy harvesting is a key enabler in realizing ubiquitous connectivity.

Standard Compliant Hybrid Active-Backscatter Radios. One of the main focuses of this thesis was on reducing the complexity of backscatter deployments. In chapter 2, I proposed full-duplex LoRa backscatter reader to simplify backscatter deployments. In chapter 3, I discussed solutions to deliver reliable backscatter reliability, independent of the backscatter tag placement or orientation. And finally, in chapter 4, I considered the case of a backscatter network and suggested an architecture that allows the backscatter tags to move freely while the base units handle the complexities in keeping the communication alive. The reason I have placed this much attention on backscatter deployment is that I believe it is the main barrier toward widespread adaptation of the backscatter technology. Users have used conventional wireless systems where two devices communicate with each other for over 30 years now, and any wireless technology that cannot match that level of reliability and ease of use has a very difficult path to widespread adaptation. One approach to this challenge

is using backscatter radios beside conventional active radios, and activating the backscatter mode whenever possible to preserve energy, as suggested in [173, 177]. To achieve widespread adaptation, it is important to make sure the design is compatible with one of the current low-power wireless standards such as Bluetooth. In other words, the main research question here is how should one modify Bluetooth (or any other) standard to include hybrid radios while maintaining compatibility with current active devices? While we proposed a full-duplex backscatter reader architecture in chapter 2, and showed the generation of LoRa and BLE compatible packets in chapters 2 and 3, these are only the first steps. Many other questions such as low-cost full-duplex backscatter reader architectures with low-loss in normal active mode, low-cost hybrid active-backscatter architectures through hardware sharing, the criteria to switch between active and backscatter modes, carrier power and interference levels in each mode, required modulation and frequency accuracy in each mode, and the effects on other layers of the protocol should be carefully discussed. Standard-compliant hybrid active-backscatter radios could pave the way for ultra-low-cost backscatter radios.

Backscatter Wireless Networks. The backscatter network proposed in chapter 4 is a first step toward, and a sample implementation of wide-area low-cost backscatter networks. While we implemented the main pieces to build a backscatter network, there are many opportunities for improvements in future works. The backscatter network design is significantly affected by the capabilities of the underlying hardware. For example, the receiver units in our implementation can receive one backscatter packet at a time. Relaxing this limitation eliminates the need to wake up a specific backscatter node in each communication cycle. The base units can transmit a general initiation pattern, and several backscatter nodes can send their data upon receiving that pattern. Such implementation needs to carefully design the network protocol to minimize collision among backscatter nodes. Another possible architecture is using hybrid active-backscatter sensor nodes, where the sensor nodes could initiate the communication with the base units. While we use half-duplex base units in MultiScatter, using Full-Duplex base units adds another degree of freedom to the network. Full-Duplex base units could communicate with a backscatter tag by themselves, or seek assistance from

other base units to form a half-duplex backscatter link. Furthermore, synchronizing base units opens the door for new features such as the coherent transmission of carrier signals or detection of backscatter packets. These are just a few examples of how the base units and backscatter nodes' hardware capabilities affect the backscatter network design. I believe there are many interesting research opportunities in this area, to further extend the throughput, coverage, and reliability, and reduce the energy consumption and latency of wide-area multistatic backscatter networks.

Sensing. Over the past decade, wireless signals have been widely used in sensing applications such as occupancy detection, gesture recognition, activity monitoring, etc. In these solutions, the wireless signal received by radio is used to capture wireless channel variations over time and different classification methods are employed to analyze these variation patterns and extract useful information [144]. Low-cost backscatter radios communicate by reflecting wireless signals in the environment. In chapter 3, I show how small movements of backscatter nodes or human activities around backscatter nodes affect the backscatter links. I believe backscatter networks can help enhance the accuracy of wireless sensing techniques by providing a fine-grained smart reflection of wireless signals.

Localization. Localization is one of the most popular applications of IoT networks. Different approaches based on Received Signal Strength Indicator (RSSI), Angle of Arrival (AoA), Time of Arrival (ToA), Time Difference of Arrival (TDoA) using different wireless technologies such as WiFi, BLE, RFID, UWB, etc. have been investigated in the literature [97]. Backscatter networks, such as the one introduced in chapter 4, can bring indoor localization to a new category of small unplugged objects. Backscatter nodes reflections are not frequency selective and using a wideband excitation signal results in a wideband reflection from a backscatter node, which could result in high accuracy localization with minimum cost [150]. Investigating cooperation techniques among the base units in multi-static backscatter networks to further increase the localization accuracy is another interesting topic for future research.

BIBLIOGRAPHY

[1] www.octopart.com.

[2] www.pcbminions.com.

[3] www.github.com/MultiScatter/.

[4] Agilent 8753es Vector Network Analyzer, 2001. https://www.keysight.com/en/pd-1000002292%3Aepsg%3Apro-pn-8753ES.

[5] S463AH-915 datasheet, 2006. https://www.nearson.com/assets/pdfs/Antenna/S463XX-915.pdf.

[6] AS213-92LF datasheet, 2008. https://www.skyworksinc.com/en/Products/switches/AS213-92LF.

[7] CC1190 datasheet, 2010. https://www.ti.com/product/CC1190.

[8] EKMB1104111 datasheet, 2012. https://media.digikey.com/pdf/DataSheets/PanasonicSensorsPDFs/EKMB_MC_AMN2_3_Rev_Sep_2012.pdf.

[9] AGLN250 datasheet, 2014. https://www.microsemi.com/product-directory/fpgas/1689-igloo#igloo-nano.

[10] AS3933 datasheet, 2015. https://www.sciosense.com/products/wireless-sensor-nodes/as3933-lf-receiver-ic/.

[11] ADG904 datasheet, 2016. https://www.analog.com/media/en/technical-documentation/data-sheets/ADG904.pdf.

[12] ADG919 datasheet, 2016. https://www.analog.com/media/en/technical-documentation/data-sheets/ADG918_919.pdf.

[13] Bluetooth core specification v5.0, vol 6, part a, 2016.

[14] Humidity & temp sensor node for star networks enabling 10+ year coin cell battery life ref design, 2016. https://www.ti.com/tool/TIDA-00374.

[15] LMX2571 datasheet, 2016. https://www.ti.com/product/LMX2571.

[16] OPT3002 datasheet, 2016. https://www.ti.com/product/OPT3002.

[17] SKYFR-001400 datasheet, 2016. https://www.skyworksinc.com/en/Products/Circulators-and-Isolators/SKYFR-001400.

[18] ADF4351 datasheet, 2017. https://www.analog.com/media/en/technical-documentation/data-sheets/ADF4351.pdf.

[19] CC2640R2F datasheet, 2017. http://www.ti.com/lit/ds/symlink/cc2640r2f.pdf.

[20] PE64906 datasheet, 2017. https://www.psemi.com/pdf/datasheets/pe64906ds.pdf.

[21] SKY65313-21 datashett, 2017. https://www.skyworksinc.com/en/Products/Front-end-Modules/SKY65313-21.

[22] stm32F413RG datasheet, 2017. https://www.st.com/resource/en/datasheet/stm32f413rg.pdf.

[23] ANT-2.4-LCW datasheet, 2018. https://linxtechnologies.com/wp/wp-content/uploads/ant-2.4-lcw-ccc-data-sheet.pdf.

[24] CC1310 datasheet, 2018. https://www.ti.com/product/CC1310.

[25] MM8430 datasheet, 2018. https://media.digikey.com/pdf/Data%20Sheets/Murata%20PDFs/Microwave_Coaxial_Conn_Cat030E.pdf.

[26] nRF52840 datasheet, 2018. https://infocenter.nordicsemi.com/pdf/nRF52840_PS_v1.0.pdf.

[27] 2021 bluetooth market update, 2019. https://www.bluetooth.com/wp-content/uploads/2021/01/2021-Bluetooth_Market_Update.pdf.

[28] Anaren X3C09P1-03S datasheet, 2019. https://www.anaren.com/catalog/xinger/90-degree-hybrid-couplers.

[29] BQ25570 datasheet, 2019. https://www.ti.com/product/BQ25570.

[30] Electronic Code of Federal Regulations, Title 47, Chapter i, Subchapter A, Part 15, Subpart C, section 15.247, 2019. www.ecfr.gov.

[31] HDC2080 datasheet, 2019. https://www.ti.com/product/HDC2080.

[32] Himax HM01B0, 2019. https://www.himax.com.tw/products/cmos-image-sensor/image-sensors/hm01b0/.

[33] Living room size, 2019. https://www.houseplanshelper.com/living-room-size.html.

[34] ST25RU3993 datasheet, 2019. https://www.st.com/en/nfc/st25ru3993.html.

[35] STM32L071CB datasheet, 2019. https://www.st.com/resource/en/datasheet/stm32l071cb.pdf.

[36] SX1276 datasheet, 2019. https://www.semtech.com/products/wireless-rf/lora-transceivers/sx1276.

[37] Vm1010 datasheet, 2019. https://vespermems.com/products/vm1010/.

[38] 100 mF supercapacitor catalog, 2020. https://content.kemet.com/datasheets/KEM_S6015_FY.pdf.

[39] 3GPP TS 36.101 V16.6.0 , 2020. https://portal.3gpp.org/.

[40] CC1312R datasheet, 2020. https://www.ti.com/product/CC1312.

[41] CC1352R datasheet, 2020. https://www.ti.com/product/CC1310.

[42] HMC630 datasheet, 2020. https://www.analog.com/en/products/hmc630.html#product-overview.

[43] Impinj Speedway Revolution R120 UHF RFID Reader, 2020. https://www.atlasrfidstore.com/rfid-readers/.

[44] JSPHS-1000 datasheet, 2020. https://www.minicircuits.com/pdfs/JSPHS-1000+.pdf.

[45] LT6990 datasheet, 2020. https://www.analog.com/media/en/technical-documentation/data-sheets/LTC6990.pdf.

[46] Panasonic solar panel catalog, 2020. https://panasonic.co.jp/ls/psam/en/products/pdf/Catalog_Amorton_ENG.pdf.

[47] Parrot AR Drone 2.0, 2020. https://www.parrot.com/us/drones/parrot-ardrone-20-elite-edition.

[48] Photo by becca tapert on unsplash, 2020.

[49] S9028PCL Circular Polarity Antenna datasheet, 2020. https://connectivity-staging.s3.us-east-2.amazonaws.com/s3fs-public/2018-10/ANT-DS-S9028PCL%20S9028PCR-0515.pdf.

[50] Python socket.io project, 2021. https://pypi.org/project/python-socketio/.

[51] Tap software, 2021. https://www.softwright.com/.

[52] Wireless insite 3d wireless prediction software, 2021. https://www.remcom.com/wireless-insite-em-propagation-software.

[53] Ali Abedi, Mohammad Hossein Mazaheri, Omid Abari, and Tim Brecht. Witag: Rethinking backscatter communication for wifi networks. In *Proceedings of the 17th ACM Workshop on Hot Topics in Networks - HotNets '18*. ACM Press, 2018.

[54] Abeer Ahmad, Akshay Athalye, Milutin Stanacević, and Samir R. Das. Collaborative channel estimation in backscattering tag-to-tag networks. In *Proceedings of the 1st ACM International Workshop on Device-Free Human Sensing - DFHS'19*. ACM Press, 2019.

[55] Rami Akeela and Behnam Dezfouli. Software-defined radios: Architecture, state-of-the-art, and challenges. *Computer Communications*, 128:106–125, sep 2018.

[56] Rabe Arshad, Hesham ElSawy, Sameh Sorour, Tareq Y. Al-Naffouri, and Mohamed-Slim Alouini. Handover management in dense cellular networks: A stochastic geometry approach. In *2016 IEEE International Conference on Communications (ICC)*. IEEE, may 2016.

[57] Ari Asp, Yaroslav Sydorov, Mikko Keskikastari, Mikko Valkama, and Jarno Niemela. Impact of modern construction materials on radio signal propagation: Practical measurements and network planning aspects. In *2014 IEEE 79th Vehicular Technology Conference (VTC Spring)*. IEEE.

[58] Ari Asp, Yaroslav Sydorov, Mikko Valkama, and Jarno Niemela. Radio signal propagation and attenuation measurements for modern residential buildings. In *2012 IEEE Globecom Workshops*. IEEE.

[59] Manu Bansal, Aaron Schulman, and Sachin Katti. Atomix: A framework for deploying signal processing applications on wireless infrastructure. In *12th USENIX Symposium on Networked Systems Design and Implementation (NSDI 15)*, pages 173–188, Oakland, CA, May 2015. USENIX Association.

[60] Dinesh Bharadia, Kiran Raj Joshi, Manikanta Kotaru, and Sachin Katti. Backfi: High throughput wifi backscatter. In *Proceedings of the 2015 ACM Conference on Special Interest Group on Data Communication - SIGCOMM '15*. ACM Press, 2015.

[61] Dinesh Bharadia, Kiran Raj Joshi, Manikanta Kotaru, and Sachin Katti. Backfi: High throughput wifi backscatter. *ACM SIGCOMM Computer Communication Review*, 45(5):283–296, aug 2015.

[62] Dinesh Bharadia, Emily McMilin, and Sachin Katti. Full Duplex Radios. In *Proceedings of the ACM SIGCOMM 2013 Conference on SIGCOMM*, SIGCOMM '13, pages 375–386, New York, NY, USA, 2013. ACM.

[63] H. Bolcskei, M. Borgmann, and A. Paulraj. Space-frequency coded MIMO-OFDM with variable multiplexing-diversity tradeoff. In *IEEE International Conference on Communications, 2003. ICC '03.* IEEE.

[64] D. J. van den Broek, E. A. M. Klumperink, and B. Nauta. An In-Band Full-Duplex Radio Receiver With a Passive Vector Modulator Downmixer for Self-Interference Cancellation. *IEEE Journal of Solid-State Circuits*, 50(12):3003–3014, December 2015.

[65] Bruce Brown. Smart pill bottle, 2019. `https://healthtechinsider.com/2019/05/13/smart-pill-bottle/`.

[66] Michael Buettner, Richa Prasad, Matthai Philipose, and David Wetherall. Recognizing daily activities with RFID-based sensors. In *Proceedings of the 11th international conference on Ubiquitous computing - Ubicomp '09*. ACM Press, 2009.

[67] Sergio Castro-Hermosa, Giulia Lucarelli, Michiel Top, Matthias Fahland, John Fahlteich, and Thomas M. Brown. Perovskite photovoltaics on roll-to-roll coated ultra-thin glass as flexible high-efficiency indoor power generators. *Cell Reports Physical Science*, 1(5):100045, may 2020.

[68] Si Chen, Maolin Zhang, Jia Zhao, Wei Gong, and Jiangchuan Liu. Reliable and practical bluetooth backscatter with commodity devices. 29(4):1717–1729.

[69] Tingjun Chen, Mahmood Baraani Dastjerdi, Jin Zhou, Harish Krishnaswamy, and Gil Zussman. Wideband full-duplex wireless via frequency-domain equalization. In *The*

25th Annual International Conference on Mobile Computing and Networking. ACM, aug 2019.

[70] Xing Chen, Jacob Breiholz, Farah B. Yahya, Christopher J. Lukas, Hun-Seok Kim, Benton H. Calhoun, and David D. Wentzloff. Analysis and design of an ultra-low-power bluetooth low-energy transmitter with ring oscillator-based ADPLL and 4$\times$ frequency edge combiner. 54(5):1339–1350.

[71] Kae Won Choi, Arif Abdul Aziz, Dedi Setiawan, Nguyen Minh Tran, Lorenz Ginting, and Dong In Kim. Distributed wireless power transfer system for internet of things devices. *IEEE Internet of Things Journal*, 5(4):2657–2671, aug 2018.

[72] Julian Chokkattu. The Display of the Future Might Be in Your Contact Lens, 2020. `https://www.wired.com/story/mojo-vision-smart-contact-lens/`.

[73] Kyojin D. Choo, Li Xu, Yejoong Kim, Ji-Hwan Seol, Xiao Wu, Dennis Sylvester, and David Blaauw. 5.2 energy-efficient low-noise CMOS image sensor with capacitor array-assisted charge-injection SAR ADC for motion-triggered low-power IoT applications. In *2019 IEEE International Solid- State Circuits Conference - (ISSCC)*. IEEE, feb 2019.

[74] K. D. Chu, M. Katanbaf, C. Su, T. Zhang, and J. C. Rudell. Integrated CMOS transceivers design towards flexible full duplex (FD) and frequency division duplex (FDD) systems. In *2018 IEEE Custom Integrated Circuits Conference (CICC)*, pages 1–11, April 2018.

[75] Kun-Da Chu, Mohamad Katanbaf, Tong Zhang, Chenxin Su, and Jacques C. Rudell. A broadband and deep-TX self-interference cancellation technique for full-duplex and frequency-domain-duplex transceiver applications. In *2018 IEEE International Solid - State Circuits Conference - (ISSCC)*. IEEE, feb 2018.

[76] Simon L. Cotton and William G. Scanlon. A statistical analysis of indoor multipath fading for a narrowband wireless body area network. In *2006 IEEE 17th International Symposium on Personal, Indoor and Mobile Radio Communications*. IEEE, sep 2006.

[77] Alberto Coustasse, M. Tomblin, and Chelsea Slack. Impact of radio-frequency identification (rfid) technologies on the hospital supply chain: A literature review. *Perspectives in health information management / AHIMA, American Health Information Management Association*, 10:1d, 10 2013.

[78] D. Cox. Antenna diversity performance in mitigating the effects of portable radiotelephone orientation and multipath propagation. *IEEE Transactions on Communications*, 31(5):620–628, may 1983.

[79] Derek Crippin. Home automation protocols guide 2019. `https://www.alarmnewengland.com/blog/home-automation-protocols`.

[80] Andrei Croitoru, Dragos Niculescu, and Costin Raiciu. Towards wifi mobility without fast handover. In *12th USENIX Symposium on Networked Systems Design and Implementation (NSDI 15)*, pages 219–234, Oakland, CA, May 2015. USENIX Association.

[81] Mahmood Baraani Dastjerdi, Sanket Jain, Negar Reiskarimian, Arun Natarajan, and Harish Krishnaswamy. 28.6 full-duplex 2×2 MIMO circulator-receiver with high TX power handling exploiting MIMO RF and shared-delay baseband self-interference cancellation. In *2019 IEEE International Solid- State Circuits Conference - (ISSCC)*. IEEE, feb 2019.

[82] Jasper de Winkel, Carlo Delle Donne, Kasim Sinan Yildirim, Przemysław Pawełczak, and Josiah Hester. Reliable timekeeping for intermittent computing. In *Proceedings of the Twenty-Fifth International Conference on Architectural Support for Programming Languages and Operating Systems*. ACM.

[83] Jasper de Winkel, Vito Kortbeek, Josiah Hester, and Przemysław Pawełczak. Battery-free game boy. *Proceedings of the ACM on Interactive, Mobile, Wearable and Ubiquitous Technologies*, 4(3):1–34, sep 2020.

[84] Abhishekh Devaraj, Mohamed Megahed, Yutao Liu, Ashwin Ramachandran, and Tejasvi Anand. A switched capacitor multiple input single output energy harvester (solar + piezo) achieving 74.6% efficiency with simultaneous MPPT. *IEEE Transactions on Circuits and Systems I: Regular Papers*, 66(12):4876–4887, dec 2019.

[85] Tolga Dinc and Harish Krishnaswamy. A t/r antenna pair with polarization-based reconfigurable wideband self-interference cancellation for simultaneous transmit and receive. In *2015 IEEE MTT-S International Microwave Symposium*. IEEE, may 2015.

[86] M. Duarte, A. Sabharwal, V. Aggarwal, R. Jana, K. K. Ramakrishnan, C. W. Rice, and N. K. Shankaranarayanan. Design and Characterization of a Full-Duplex Multiantenna System for WiFi Networks. *IEEE Transactions on Vehicular Technology*, 63(3):1160–1177, March 2014.

[87] Paul Emrath. Spaces in new homes, 2013. `http://nahbclassic.org/generic.aspx?genericContentID=216616`.

[88] Joshua F. Ensworth, Alexander T. Hoang, Thang Q. Phu, and Matthew S. Reynolds. Full-duplex bluetooth low energy (BLE) compatible backscatter communication system for mobile devices. In *2017 IEEE Topical Conference on Wireless Sensors and Sensor Networks (WiSNet)*. IEEE, jan 2017.

[89] Joshua F. Ensworth and Matthew S. Reynolds. Every smart phone is a backscatter reader: Modulated backscatter compatibility with bluetooth 4.0 low energy (BLE) devices. In *2015 IEEE International Conference on RFID (RFID)*. IEEE, apr 2015.

[90] Joshua F. Ensworth and Matthew S. Reynolds. BLE-backscatter: Ultralow-power IoT nodes compatible with bluetooth 4.0 low energy (BLE) smartphones and tablets. *IEEE Transactions on Microwave Theory and Techniques*, 65(9):3360–3368, sep 2017.

[91] Hani Esmaeelzadeh and Sudhakar Pamarti. A quick startup technique for high- q oscillators using precisely timed energy injection. *IEEE Journal of Solid-State Circuits*, 53(3):692–702, mar 2018.

[92] E. Everett, A. Sahai, and A. Sabharwal. Passive Self-Interference Suppression for Full-Duplex Infrastructure Nodes. *IEEE Transactions on Wireless Communications*, 13(2):680–694, February 2014.

[93] H.T. Friis. A note on a simple transmission formula. *Proceedings of the IRE*, 34(5):254–256, may 1946.

[94] Ander Galisteo, Ambuj Varshney, and Domenico Giustiniano. Two to tango: hybrid light and backscatter networks for next billion devices. In *Proceedings of the 18th International Conference on Mobile Systems, Applications, and Services*. ACM, jun 2020.

[95] R. Ganesh and K. Pahlavan. On the modeling of fading multipath indoor radio channels. In *IEEE Global Telecommunications Conference, 1989, and Exhibition. 'Communications Technology for the 1990s and Beyond*. IEEE.

[96] Kai Geissdoerfer and Marco Zimmerling. Bootstrapping battery-free wireless networks: Efficient neighbor discovery and synchronization in the face of intermittency. In *18th USENIX Symposium on Networked Systems Design and Implementation (NSDI 21)*, pages 439–455. USENIX Association, April 2021.

[97] Sheetal Ghorpade, Marco Zennaro, and Bharat Chaudhari. Survey of localization for internet of things nodes: Approaches, challenges and open issues. 13(8):210.

[98] Bradford W. Gildon. InPen smart insulin pen system: Product review and user experience. *Diabetes Spectrum*, 31(4):354–358, sep 2018.

[99] Andrea Goldsmith. *Wireless Communications*. Cambridge University Pr., 2005.

[100] Wei Gong, Haoxiang Liu, Kebin Liu, Qiang Ma, and Yunhao Liu. Exploiting channel diversity for rate adaptation in backscatter communication networks. In *IEEE INFOCOM 2016 - The 35th Annual IEEE International Conference on Computer Communications*. IEEE, apr 2016.

[101] Wei Gong, Longzhi Yuan, Qiwei Wang, and Jia Zhao. Multiprotocol backscatter for personal IoT sensors. In *Proceedings of the 16th International Conference on emerging Networking EXperiments and Technologies*. ACM, nov 2020.

[102] Joshua D. Griffin and Gregory D. Durgin. Multipath fading measurements at 5.8 GHz for backscatter tags with multiple antennas. *IEEE Transactions on Antennas and Propagation*, 58(11):3693–3700, nov 2010.

[103] Philipp Gutruf, Rose T. Yin, K. Benjamin Lee, Jokubas Ausra, Jaclyn A. Brennan, Yun Qiao, Zhaoqian Xie, Roberto Peralta, Olivia Talarico, Alejandro Murillo, Sheena W. Chen, John P. Leshock, Chad R. Haney, Emily A. Waters, Changxing Zhang, Haiwen Luan, Yonggang Huang, Gregory Trachiotis, Igor R. Efimov, and John A. Rogers. Wireless, battery-free, fully implantable multimodal and multisite pacemakers for applications in small animal models. *Nature Communications*, 10(1), dec 2019.

[104] Seungyong Han, Jeonghyun Kim, Sang Min Won, Yinji Ma, Daeshik Kang, Zhaoqian Xie, Kyu-Tae Lee, Ha Uk Chung, Anthony Banks, Seunghwan Min, Seung Yun Heo, Charles R. Davies, Jung Woo Lee, Chi-Hwan Lee, Bong Hoon Kim, Kan Li, Yadong Zhou, Chen Wei, Xue Feng, Yonggang Huang, and John A. Rogers. Battery-free, wireless sensors for full-body pressure and temperature mapping. *Science Translational Medicine*, 10(435):eaan4950, apr 2018.

[105] Mehrdad Hessar, Saman Naderiparizi, Ye Wang, Ali Saffari, Shyamnath Gollakota, and Joshua R. Smith. Wireless video streaming for ultra-low-power cameras. In *Proceedings of the 16th Annual International Conference on Mobile Systems, Applications, and Services*. ACM, jun 2018.

[106] Mehrdad Hessar, Ali Najafi, and Shyamnath Gollakota. Netscatter: Enabling large-scale backscatter networks. In *Proceedings of the 16th USENIX Conference on Networked Systems Design and Implementation*, NSDI'19, pages 271–283, Berkeley, CA, USA, 2019. USENIX Association.

[107] Nguyen Van Huynh, Dinh Thai Hoang, Xiao Lu, Dusit Niyato, Ping Wang, and Dong In Kim. Ambient backscatter communications: A contemporary survey. *IEEE Communications Surveys & Tutorials*, 20(4):2889–2922, 2018.

[108] Vikram Iyer, Vamsi Talla, Bryce Kellogg, Shyamnath Gollakota, and Joshua Smith. Inter-technology backscatter: Towards internet connectivity for implanted devices. In *Proceedings of the 2016 ACM SIGCOMM Conference*, SIGCOMM '16, pages 356–369, New York, NY, USA, 2016. ACM.

[109] Margarite Jacoby, Sin Yong Tan, Mohamad Katanbaf, Ali Saffari, Homagni Saha, Zerina Kapetanovic, Jasmine Garland, Anthony Florita, Gregor Henze, Soumik Sarkar, and Joshua Smith. WHISPER: Wireless home identification and sensing platform for energy reduction. 10(4):71.

[110] Cheonhoo Jeon, Jahyun Koo, Kyongsu Lee, Minseob Lee, Su-Kyoung Kim, Sangbaie Shin, Sei Kwang Hahn, and Jae-Yoon Sim. A smart contact lens controller IC supporting dual-mode telemetry with wireless-powered backscattering LSK and EM-radiated RF transmission using a single-loop antenna. *IEEE Journal of Solid-State Circuits*, 55(4):856–867, apr 2020.

[111] Chengkun Jiang, Yuan He, Meng Jin, Xiaolong Zheng, and Junchen Guo. Canon: Exploiting channel diversity for reliable parallel decoding in backscatter communication. In *2018 IEEE 26th International Conference on Network Protocols (ICNP)*. IEEE, sep 2018.

[112] Glenn Jocher, Alex Stoken, Jirka Borovec, NanoCode012, Ayush Chaurasia, TaoXie, Liu Changyu, Abhiram V, Laughing, tkianai, yxNONG, Adam Hogan, lorenzomammana, AlexWang1900, Jan Hajek, Laurentiu Diaconu, Marc, Yonghye Kwon, oleg, wanghaoyang0106, Yann Defretin, Aditya Lohia, ml5ah, Ben Milanko, Benjamin Fineran, Daniel Khromov, Ding Yiwei, Doug, Durgesh, and Francisco Ingham. ultralytics/yolov5: v5.0 - YOLOv5-P6 1280 models, AWS, Supervise.ly and YouTube integrations, April 2021.

[113] Colleen Josephson, Lei Yang, Pengyu Zhang, and Sachin Katti. Wireless computer vision using commodity radios. In *Proceedings of the 18th International Conference on Information Processing in Sensor Networks - IPSN '19*. ACM Press, 2019.

[114] Sung-Chan Jung, Min-Su Kim, and Youngoo Yang. A reconfigurable carrier leakage canceler for UHF RFID reader front-ends. *IEEE Transactions on Circuits and Systems I: Regular Papers*, 58(1):70–76, jan 2011.

[115] Sai Nithin R. Kantareddy, Ian Mathews, Rahul Bhattacharyya, Ian Marius Peters, Tonio Buonassisi, and Sanjay E. Sarma. Long range battery-less PV-powered RFID tag sensors. *IEEE Internet of Things Journal*, 6(4):6989–6996, aug 2019.

[116] Zerina Kapetanovic, Ali Saffari, Ranveer Chandra, and Joshua R. Smith. Glaze: Overlaying occupied spectrum with downlink iot transmissions. *Proceedings of the ACM on Interactive, Mobile, Wearable and Ubiquitous Technologies*, 3(4):1–21, dec 2019.

[117] Ramgopal Kashyap. Applications of wireless sensor networks in healthcare. In *Advances in Wireless Technologies and Telecommunication*, pages 8–40. IGI Global, 2020.

[118] Mohamad Katanbaf, Kun-Da Chu, Tong Zhang, Chenxin Su, and Jacques C. Rudell. Two-way traffic ahead: RF\/analog self-interference cancellation techniques and the challenges for future integrated full-duplex transceivers. *IEEE Microwave Magazine*, 20(2):22–35, feb 2019.

[119] Mohamad Katanbaf, Vivek Jain, and Joshua R. Smith. Relacks: Reliable backscatter communication in indoor environments. *Proceedings of the ACM on Interactive, Mobile, Wearable and Ubiquitous Technologies*, 4(2):1–24, jun 2020.

[120] Mohamad Katanbaf, Ali Saffari, and Joshua R. Smith. MultiScatter. In *Proceedings of the 19th ACM Conference on Embedded Networked Sensor Systems*. ACM.

[121] Mohamad Katanbaf, Ali Saffari, and Joshua R. Smith. Receiver selectivity limits on bistatic backscatter range. In *2020 IEEE International Conference on RFID (RFID)*. IEEE, sep 2020.

[122] Mohamad Katanbaf, Anthony Weinand, and Vamsi Talla. Simplifying backscatter deployment: Full-duplex lora backscatter. In *18th USENIX Symposium on Networked Systems Design and Implementation (NSDI 21)*, pages 955–972. USENIX Association, April 2021.

[123] Edward A. Keehr. A low-cost, high-speed, high-resolution, adaptively tunable microwave network for an SDR UHF RFID reader reflected power canceller. In *2018 IEEE International Conference on RFID (RFID)*. IEEE, apr 2018.

[124] Edward A. Keehr. A low-cost software-defined UHF RFID reader with active transmit leakage cancellation. In *2018 IEEE International Conference on RFID (RFID)*. IEEE, apr 2018.

[125] Bryce Kellogg, Vamsi Talla, Shyamnath Gollakota, and Joshua R. Smith. Passive wi-fi: Bringing low power to wi-fi transmissions. In *Proceedings of the 13th Usenix Conference on Networked Systems Design and Implementation*, NSDI'16, pages 151–164, Berkeley, CA, USA, 2016. USENIX Association.

[126] Seiran Khaledian, Farhad Farzami, Besma Smida, and Danilo Erricolo. Inherent self-interference cancellation for in-band full-duplex single-antenna systems. *IEEE Transactions on Microwave Theory and Techniques*, 66(6):2842–2850, jun 2018.

[127] A. Kiayani, M. Z. Waheed, L. Anttila, M. Abdelaziz, D. Korpi, V. Syrjälä, M. Kosunen, K. Stadius, J. Ryynänen, and M. Valkama. Adaptive Nonlinear RF Cancellation for Improved Isolation in Simultaneous Transmit #x2013;Receive Systems. *IEEE Transactions on Microwave Theory and Techniques*, 66(5):2299–2312, May 2018.

[128] Daeyoung Kim, M.A. Ingram, and W.W. Smith. Measurements of small-scale fading and path loss for long range RF tags. *IEEE Transactions on Antennas and Propagation*, 51(8):1740–1749, aug 2003.

[129] Jeonghyun Kim, Philipp Gutruf, Antonio M. Chiarelli, Seung Yun Heo, Kyoungyeon Cho, Zhaoqian Xie, Anthony Banks, Seungyoung Han, Kyung-In Jang, Jung Woo Lee, Kyu-Tae Lee, Xue Feng, Yonggang Huang, Monica Fabiani, Gabriele Gratton, Ungyu Paik, and John A. Rogers. Miniaturized battery-free wireless systems for wearable pulse oximetry. *Advanced Functional Materials*, 27(1):1604373, nov 2016.

[130] Kai Klinker, Manuel Wiesche, and Helmut Krcmar. Smart glasses in health care: A patient trust perspective. In *Proceedings of the 53rd Hawaii International Conference on System Sciences*. Hawaii International Conference on System Sciences, 2020.

[131] David C. Klonoff and David Kerr. Smart pens will improve insulin therapy. *Journal of Diabetes Science and Technology*, 12(3):551–553, feb 2018.

[132] D. Korpi, M. Heino, C. Icheln, K. Haneda, and M. Valkama. Compact Inband Full-Duplex Relays With Beyond 100 dB Self-Interference Suppression: Enabling Techniques and Field Measurements. *IEEE Transactions on Antennas and Propagation*, 65(2):960–965, February 2017.

[133] D. Korpi, J. Tamminen, M. Turunen, T. Huusari, Y. S. Choi, L. Anttila, S. Talwar, and M. Valkama. Full-duplex mobile device: pushing the limits. *IEEE Communications Magazine*, 54(9):80–87, September 2016.

[134] Siddharth R. Krishnan, Chun-Ju Su, Zhaoqian Xie, Manish Patel, Surabhi R. Madhvapathy, Yeshou Xu, Juliet Freudman, Barry Ng, Seung Yun Heo, Heling Wang, Tyler R. Ray, John Leshock, Izabela Stankiewicz, Xue Feng, Yonggang Huang, Philipp Gutruf, and John A. Rogers. Wireless, battery-free epidermal electronics for continuous, quantitative, multimodal thermal characterization of skin. *Small*, 14(47):1803192, oct 2018.

[135] Abhishek Kumar and Sankaran Aniruddhan. A 2.35 GHz cross-talk canceller for 2×2 MIMO full-duplex wireless system. In *2019 IEEE MTT-S International Microwave Symposium (IMS)*. IEEE, jun 2019.

[136] Antonio Lazaro, David Girbau, and David Salinas. Radio link budgets for UHF RFID on multipath environments. *IEEE Transactions on Antennas and Propagation*, 57(4):1241–1251, apr 2009.

[137] Sanghoon Lee, Hao Wang, Jiahui Wang, Qiongfeng Shi, Shih-Cheng Yen, Nitish V. Thakor, and Chengkuo Lee. Battery-free neuromodulator for peripheral nerve direct stimulation. *Nano Energy*, 50:148–158, aug 2018.

[138] Songfan Li, Hui Zheng, Chong Zhang, Yihang Song, Shen Yang, Minghua Chen, Li Lu, and Mo Li. Passive dsss: Empowering the downlink communication for backscatter systems.

[139] Tianxing Li and Xia Zhou. Battery-free eye tracker on glasses. In *Proceedings of the 24th Annual International Conference on Mobile Computing and Networking - MobiCom '18*. ACM Press, 2018.

[140] Xin Li, Li Teng, Hong Tang, Jingying Chen, Haoyu Wang, Yu Liu, Minfan Fu, and Junrui Liang. Vipsn: A vibration-powered iot platform. *IEEE Internet of Things Journal*, 2020.

[141] Yan Li, Zicheng Chi, Xin Liu, and Ting Zhu. Passive-zigbee: Enabling zigbee communication in IoT networks with 1000x+ less power consumption. In *Proceedings of the 16th ACM Conference on Embedded Networked Sensor Systems - SenSys '18*. ACM Press, 2018.

[142] B. van Liempd, B. Hershberg, S. Ariumi, K. Raczkowski, K. F. Bink, U. Karthaus, E. Martens, P. Wambacq, and J. Craninckx. A 70 dBm IIP3 Electrical-Balance Duplexer for Highly Integrated Tunable Front-Ends. *IEEE Transactions on Microwave Theory and Techniques*, 64(12):4274–4286, December 2016.

[143] Xiaoyou Lin and Boon-Chong Seet. Battery-free smart sock for abnormal relative plantar pressure monitoring. *IEEE Transactions on Biomedical Circuits and Systems*, 11(2):464–473, apr 2017.

[144] Jian Liu, Hongbo Liu, Yingying Chen, Yan Wang, and Chen Wang. Wireless sensing for human activity: A survey. 22(3):1629–1645.

[145] Vincent Liu, Aaron Parks, Vamsi Talla, Shyamnath Gollakota, David Wetherall, and Joshua R. Smith. Ambient backscatter: Wireless communication out of thin air. In *Proceedings of the ACM SIGCOMM 2013 Conference on SIGCOMM*, SIGCOMM '13, pages 39–50, New York, NY, USA, 2013. ACM.

[146] Xin Liu, Zicheng Chi, Wei Wang, Yao Yao, and Ting Zhu. Vmscatter: A versatile {MIMO} backscatter. In *17th {USENIX} Symposium on Networked Systems Design and Implementation ({NSDI} 20)*, pages 895–909, 2020.

[147] Gaël Loubet, Alexandru Takacs, Ethan Gardner, Andrea De Luca, Florin Udrea, and Daniela Dragomirescu. LoRaWAN battery-free wireless sensors network designed for structural health monitoring in the construction domain. *Sensors*, 19(7):1510, mar 2019.

[148] Zhihong Luo, Qiping Zhang, Yunfei Ma, Manish Singh, and Fadel Adib. 3d backscatter localization for fine-grained robotics. In *16th USENIX Symposium on Networked Systems Design and Implementation (NSDI 19)*, pages 765–782, Boston, MA, February 2019. USENIX Association.

[149] Yunfei Ma, Xiaonan Hui, and Edwin C. Kan. 3d real-time indoor localization via broadband nonlinear backscatter in passive devices with centimeter precision. In *Proceedings of the 22nd Annual International Conference on Mobile Computing and Networking - MobiCom '16*. ACM Press, 2016.

[150] Yunfei Ma, Nicholas Selby, and Fadel Adib. Minding the billions. In *Proceedings of the 23rd Annual International Conference on Mobile Computing and Networking*. ACM.

[151] Yunfei Ma, Nicholas Selby, and Fadel Adib. Drone relays for battery-free networks. In *Proceedings of the Conference of the ACM Special Interest Group on Data Communication - SIGCOMM '17*. ACM Press, 2017.

[152] Michele Magno, Xiaying Wang, Manuel Eggimann, Lukas Cavigelli, and Luca Benini. InfiniWolf: Energy efficient smart bracelet for edge computing with dual source energy harvesting. In *2020 Design, Automation & Test in Europe Conference & Exhibition (DATE)*. IEEE, mar 2020.

[153] Vivek Mangal and Peter R. Kinget. 28.1 a 0.42nw 434mhz -79.1dbm wake-up receiver with a time-domain integrator. In *2019 IEEE International Solid- State Circuits Conference - (ISSCC)*. IEEE, feb 2019.

[154] Kayla Matthews. Comparing the best smart home network protocols in 2019, available online at: "https://www.iotforall.com/comparing-best-smart-home-network-protocols-2019/", accessed: 10/03/2019.

[155] Joseph Mauro, Kelly B. Mathews, and Eric S. Sredzinski. Effect of a smart pill bottle and pharmacist intervention on medication adherence in patients with multiple myeloma new to lenalidomide therapy. *Journal of Managed Care & Specialty Pharmacy*, 25(11):1244–1254, nov 2019.

[156] Hannes Michaels, Michael Rinderle, Richard Freitag, Iacopo Benesperi, Tomas Edvinsson, Richard Socher, Alessio Gagliardi, and Marina Freitag. Dye-sensitized solar cells under ambient light powering machine learning: towards autonomous smart sensors for the internet of things. *Chemical Science*, 11(11):2895–2906, 2020.

[157] Timothy Miller, Stephen S Oyewobi, Adnan M Abu-Mahfouz, and Gerhard P Hancke. Enabling a battery-less sensor node using dedicated radio frequency energy harvesting for complete off-grid applications. *Energies*, 13(20):5402, 2020.

[158] Saman Naderiparizi, Aaron N. Parks, Zerina Kapetanovic, Benjamin Ransford, and Joshua R. Smith. WISPCam: A battery-free RFID camera. In *2015 IEEE International Conference on RFID (RFID)*. IEEE, apr 2015.

[159] Rajalakshmi Nandakumar, Vikram Iyer, and Shyamnath Gollakota. 3d localization for sub-centimeter sized devices. In *Proceedings of the 16th ACM Conference on Embedded Networked Sensor Systems - SenSys '18*. ACM Press, 2018.

[160] Francesco Orfei, Chiara Benedetta Mezzetti, and Francesco Cottone. Vibrations powered LoRa sensor: An electromechanical energy harvester working on a real bridge. In *2016 IEEE SENSORS*. IEEE, oct 2016.

[161] Christoph Paasch, Gregory Detal, Fabien Duchene, Costin Raiciu, and Olivier Bonaventure. Exploring mobile/WiFi handover with multipath TCP. In *Proceedings of the 2012 ACM SIGCOMM workshop on Cellular networks: operations, challenges, and future design - CellNet '12*. ACM Press, 2012.

[162] L.I. Parad and R.L. Moynihan. Split-tee power divider. *IEEE Transactions on Microwave Theory and Techniques*, 13(1):91–95, jan 1965.

[163] Yao Peng, Longfei Shangguan, Yue Hu, Yujie Qian, Xianshang Lin, Xiaojiang Chen, Dingyi Fang, and Kyle Jamieson. Plora: a passive long-range data network from ambient lora transmissions. In *Proceedings of the 2018 Conference of the ACM Special Interest Group on Data Communication - SIGCOMM18*. ACM Press, 2018.

[164] Rajeev Piyare, Amy L. Murphy, Csaba Kiraly, Pietro Tosato, and Davide Brunelli. Ultra low power wake-up radios: A hardware and networking survey. *IEEE Communications Surveys & Tutorials*, 19(4):2117–2157, 2017.

[165] G.P. Pollini. Trends in handover design. *IEEE Communications Magazine*, 34(3):82–90, mar 1996.

[166] C.Y. Pon. Hybrid-ring directional coupler for arbitrary power divisions. *IEEE Transactions on Microwave Theory and Techniques*, 9(6):529–535, nov 1961.

[167] Poonam, Kriti Sharma, Anmol Arora, and S.K. Tripathi. Review of supercapacitors: Materials and devices. *Journal of Energy Storage*, 21:801–825, feb 2019.

[168] Radislav A. Potyrailo, Nandini Nagraj, Zhexiong Tang, Frank J. Mondello, Cheryl Surman, and William Morris. Battery-free radio frequency identification (RFID) sensors for food quality and safety. *Journal of Agricultural and Food Chemistry*, 60(35):8535–8543, aug 2012.

[169] Anthony Quelen, Gael Pillonnet, Pierre Gasnier, Francois Rummens, and Sebastien Boisseau. 32.3 electromagnetic mechanical energy-harvester IC with no off-chip component and one switching period MPPT achieving up to 95.9% end-to-end efficiency and 460% energy-extraction gain. In *2020 IEEE International Solid- State Circuits Conference - (ISSCC)*. IEEE, feb 2020.

[170] Philipp A. Rauschnabel and Young K. Ro. Augmented reality smart glasses: an investigation of technology acceptance drivers. *International Journal of Technology Marketing*, 11(2):123, 2016.

[171] Behzad Razavi. *RF microelectronics*. Prentice Hall, Upper Saddle River, NJ, 2nd ed edition, 2012.

[172] Negar Reiskarimian, Mahmood Baraani Dastjerdi, Jin Zhou, and Harish Krishnaswamy. Analysis and design of commutation-based circulator-receivers for integrated full-duplex wireless. *IEEE Journal of Solid-State Circuits*, 53(8):2190–2201, aug 2018.

[173] Matthew S. Reynolds. A 2.4-GHz, hybrid 10-mb/s BPSK backscatter and 1-mb/s FSK bluetooth TX with hardware reuse. 27(12):1155–1157.

[174] Ignacio Rodriguez, Huan C. Nguyen, Niels T. K. Jorgensen, Troels B. Sorensen, and Preben Mogensen. Radio propagation into modern buildings: Attenuation measurements in the range from 800 MHz to 18 GHz. In *2014 IEEE 80th Vehicular Technology Conference (VTC2014-Fall)*. IEEE.

[175] James Rosenthal, Alexandra Pike, and Matthew S. Reynolds. A 1 mbps 158 pJ/bit bluetooth low energy (BLE) compatible backscatter communication uplink for wireless neural recording in an animal cage environment. In *2019 IEEE International Conference on RFID (RFID)*. IEEE, apr 2019.

[176] James Rosenthal, Apoorva Sharma, Eleftherios Kampianakis, and Matthew S. Reynolds. A 25 mbps, 12.4 pJ/b DQPSK backscatter data uplink for the NeuroDisc brain–computer interface. *IEEE Transactions on Biomedical Circuits and Systems*, 13(5):858–867, oct 2019.

[177] Mohammad Rostami, Jeremy Gummeson, Ali Kiaghadi, and Deepak Ganesan. Polymorphic radios: A new design paradigm for ultra-low power communication. In *Proceedings of the 2018 Conference of the ACM Special Interest Group on Data Communication*, SIGCOMM '18, pages 446–460, New York, NY, USA, 2018. ACM.

[178] Jihoon Ryoo, Yasha Karimi, Akshay Athalye, Milutin Stanaćević, Samir R. Das, and Petar Djurić. BARNET towards activity recognition using passive backscattering tag-to-tag network. In *Proceedings of the 16th Annual International Conference on Mobile Systems, Applications, and Services - MobiSys 18*. ACM Press, 2018.

[179] Kamala Raghavan Sadagopan, Jian Kang, Sanket Jain, Yogesh Ramadass, and Arun Natarajan. A 365nw -61.5 dBm sensitivity, 1.875 cm2 2.4 GHz wake-up receiver with rectifier-antenna co-design for passive gain. In *2017 IEEE Radio Frequency Integrated Circuits Symposium (RFIC)*. IEEE, jun 2017.

[180] Ali Saffari, Mehrdad Hessar, Saman Naderiparizi, and Joshua R. Smith. Battery-free wireless video streaming camera system. In *2019 IEEE International Conference on RFID (RFID)*. IEEE, apr 2019.

[181] Ali Saffari, Sin Yong Tan, Mohamad Katanbaf, Homagni Saha, Joshua R. Smith, and Soumik Sarkar. Battery-free camera occupancy detection system. In *Proceedings of the 5th International Workshop on Embedded and Mobile Deep Learning*, EMDL'21, page 13–18, New York, NY, USA, 2021. Association for Computing Machinery.

[182] A.P. Sample, D.J. Yeager, P.S. Powledge, A.V. Mamishev, and J.R. Smith. Design of an RFID-based battery-free programmable sensing platform. *IEEE Transactions on Instrumentation and Measurement*, 57(11):2608–2615, nov 2008.

[183] A. El Sayed, A. Ahmed, A. K. Mishra, A. H. M. Shirazi, S. P. Woo, Y. S. Choi, S. Mirabbasi, and S. Shekhar. A full-duplex receiver with 80mhz bandwidth self-interference cancellation circuit using baseband Hilbert transform equalization. In *2017 IEEE Radio Frequency Integrated Circuits Symposium (RFIC)*, pages 360–363, June 2017.

[184] Bojing Shi, Zhou Li, and Yubo Fan. Implantable energy-harvesting devices. *Advanced Materials*, 30(44):1801511, jul 2018.

[185] Lukas Sigrist, Rehan Ahmed, Andres Gomez, and Lothar Thiele. Harvesting-aware optimal communication scheme for infrastructure-less sensing. *ACM Trans. Internet Things*, 1(4), June 2020.

[186] M. S. Sim, M. Chung, D. Kim, J. Chung, D. K. Kim, and C. B. Chae. Nonlinear Self-Interference Cancellation for Full-Duplex Radios: From Link-Level and System-Level Performance Perspectives. *IEEE Communications Magazine*, 55(9):158–167, 2017.

[187] Yu Song, Jihong Min, You Yu, Haobin Wang, Yiran Yang, Haixia Zhang, and Wei Gao. Wireless battery-free wearable sweat sensor powered by human motion. *Science Advances*, 6(40):eaay9842, sep 2020.

[188] E.A. Sourour and M. Nakagawa. Performance of orthogonal multicarrier CDMA in a multipath fading channel. *IEEE Transactions on Communications*, 44(3):356–367, mar 1996.

[189] Joanna Stewart. Average bedroom size and dimensions., 2017.

[190] Vamsi Talla, Mehrdad Hessar, Bryce Kellogg, Ali Najafi, Joshua R. Smith, and Shyamnath Gollakota. Lora backscatter: Enabling the vision of ubiquitous connectivity. *Proceedings of the ACM on Interactive, Mobile, Wearable and Ubiquitous Technologies*, 1(3):1–24, sep 2017.

[191] Vamsi Talla, Bryce Kellogg, Shyamnath Gollakota, and Joshua R. Smith. Battery-free cellphone. *Proceedings of the ACM on Interactive, Mobile, Wearable and Ubiquitous Technologies*, 1(2):1–20, jun 2017.

[192] Vamsi Talla, Joshua Smith, and Shyamnath Gollakota. Advances and open problems in backscatter networking. 24(4):32–38.

[193] Emmeric Tanghe, Wout Joseph, Leen Verloock, Luc Martens, Henk Capoen, Kobe Herwegen, and Wim Vantomme. The industrial indoor channel: large-scale and temporal fading at 900, 2400, and 5200 MHz. *IEEE Transactions on Wireless Communications*, 7(7):2740–2751, jul 2008.

[194] S. J. Thomas, R. R. Harrison, A. Leonardo, and M. S. Reynolds. A battery-free multichannel digital neural/EMG telemetry system for flying insects. *IEEE Transactions on Biomedical Circuits and Systems*, 6(5):424–436, oct 2012.

[195] Stewart J. Thomas and Matthew S. Reynolds. A 96 mbit/sec, 15.5 pJ/bit 16-QAM modulator for UHF backscatter communication. In *2012 IEEE International Conference on RFID (RFID)*. IEEE.

[196] Lekhobola Tsoeunyane, Simon Winberg, and Michael Inggs. Software-defined radio FPGA cores: Building towards a domain-specific language. *International Journal of Reconfigurable Computing*, 2017:1–28, 2017.

[197] Peter J. M. van Laarhoven and Emile H. L. Aarts. Simulated annealing. In *Simulated Annealing: Theory and Applications*, pages 7–15. Springer Netherlands, 1987.

[198] Ambuj Varshney, Carlos Pérez-Penichet, Christian Rohner, and Thiemo Voigt. Lorea: A backscatter architecture that achieves a long communication range. In *Proceedings of the 15th ACM Conference on Embedded Network Sensor Systems - SenSys 17*. ACM Press, 2017.

[199] Ambuj Varshney, Andreas Soleiman, Luca Mottola, and Thiemo Voigt. Battery-free visible light sensing. In *Proceedings of the 4th ACM Workshop on Visible Light Communication Systems*. ACM, oct 2017.

[200] Deepak Vasisht, Zerina Kapetanovic, Jong-ho Won, Xinxin Jin, Ranveer Chandra, Ashish Kapoor, Sudipta N. Sinha, Madhusudhan Sudarshan, and Sean Stratman. Farmbeats: An iot platform for data-driven agriculture. In *Proceedings of the 14th USENIX Conference on Networked Systems Design and Implementation*, NSDI'17, page 515–528, USA, 2017. USENIX Association.

[201] Po-Han Peter Wang, Haowei Jiang, Li Gao, Pinar Sen, Young-Han Kim, Gabriel M. Rebeiz, Patrick P. Mercier, and Drew A. Hall. A near-zero-power wake-up receiver achieving -69-dBm sensitivity. *IEEE Journal of Solid-State Circuits*, 53(6):1640–1652, jun 2018.

[202] Po-Han Peter Wang, Chi Zhang, Hongsen Yang, Dinesh Bharadia, and Patrick P. Mercier. 20.1 a 28μw IoT tag that can communicate with commodity WiFi transceivers via a single-side-band QPSK backscatter communication technique. In *2020 IEEE International Solid- State Circuits Conference - (ISSCC)*. IEEE, feb 2020.

[203] Pavan S. Yedavalli, Taneli Riihonen, Xiaodong Wang, and Jan M. Rabaey. Far-field RF wireless power transfer with blind adaptive beamforming for internet of things devices. *IEEE Access*, 5:1743–1752, 2017.

[204] Hao Zhang, Philipp Gutruf, Kathleen Meacham, Michael C. Montana, Xingyue Zhao, Antonio M. Chiarelli, Abraham Vázquez-Guardado, Aaron Norris, Luyao Lu, Qinglei Guo, Chenkai Xu, Yixin Wu, Hangbo Zhao, Xin Ning, Wubin Bai, Irawati Kandela, Chad R. Haney, Debashis Chanda, Robert W. Gereau, and John A. Rogers. Wireless, battery-free optoelectronic systems as subdermal implants for local tissue oximetry. *Science Advances*, 5(3):eaaw0873, mar 2019.

[205] Maolin Zhang, Si Chen, Jia Zhao, and Wei Gong. Commodity-level BLE backscatter. In *Proceedings of the 19th Annual International Conference on Mobile Systems, Applications, and Services*. ACM.

[206] Pengyu Zhang, Dinesh Bharadia, Kiran Joshi, and Sachin Katti. Hitchhike: Practical backscatter using commodity wifi. In *Proceedings of the 14th ACM Conference on Embedded Network Sensor Systems CD-ROM*, SenSys '16, pages 259–271, New York, NY, USA, 2016. ACM.

[207] Pengyu Zhang, Jeremy Gummeson, and Deepak Ganesan. Blink: a high throughput link layer for backscatter communication. In *Proceedings of the 10th international conference on Mobile systems, applications, and services - MobiSys12*. ACM Press, 2012.

[208] Pengyu Zhang, Colleen Josephson, Dinesh Bharadia, and Sachin Katti. Freerider: Backscatter communication using commodity radios. In *Proceedings of the 13th International Conference on emerging Networking and Technologies - CoNEXT17*. ACM Press, 2017.

[209] Pengyu Zhang, Mohammad Rostami, Pan Hu, and Deepak Ganesan. Enabling practical backscatter communication for on-body sensors. In *Proceedings of the 2016 conference on ACM SIGCOMM 2016 Conference - SIGCOMM '16*. ACM Press, 2016.

[210] Sanliang Zhang and Ning Pan. Supercapacitors performance evaluation. *Advanced Energy Materials*, 5(6):1401401, dec 2014.

[211] T. Zhang, C. Su, A. Najafi, and J. C. Rudell. Wideband Dual-Injection Path Self-Interference Cancellation Architecture for Full-Duplex Transceivers. *IEEE Journal of Solid-State Circuits*, 53(6):1563–1576, June 2018.

[212] Yang Zhang, Yasha Iravantchi, Haojian Jin, Swarun Kumar, and Chris Harrison. Sozu: Self-powered radio tags for building-scale activity sensing. In *Proceedings of the 32nd Annual ACM Symposium on User Interface Software and Technology*. ACM, oct 2019.

[213] Jia Zhao, Wei Gong, and Jiangchuan Liu. Spatial stream backscatter using commodity WiFi. In *Proceedings of the 16th Annual International Conference on Mobile Systems, Applications, and Services - MobiSys 18*. ACM Press, 2018.

[214] Jia Zhao, Wei Gong, and Jiangchuan Liu. Towards scalable backscatter sensor mesh with decodable relay and distributed excitation. In *Proceedings of the 18th International Conference on Mobile Systems, Applications, and Services*. ACM, jun 2020.

[215] Renjie Zhao, Fengyuan Zhu, Yuda Feng, Siyuan Peng, Xiaohua Tian, Hui Yu, and Xinbing Wang. OFDMA-enabled wi-fi backscatter. In *The 25th Annual International Conference on Mobile Computing and Networking - MobiCom19*. ACM Press, 2019.

[216] Yi Zhao and Joshua R. Smith. A battery-free RFID-based indoor acoustic localization platform. In *2013 IEEE International Conference on RFID (RFID)*. IEEE, apr 2013.

[217] J. Zhou, T. H. Chuang, T. Dinc, and H. Krishnaswamy. Integrated Wideband Self-Interference Cancellation in the RF Domain for FDD and Full-Duplex Wireless. *IEEE Journal of Solid-State Circuits*, 50(12):3015–3031, December 2015.

[218] Fengyuan Zhu, Yuda Feng, Qianru Li, Xiaohua Tian, and Xinbing Wang. DigiScatter: efficiently prototyping large-scale ofdma backscatter networks. In *Proceedings of the 18th International Conference on Mobile Systems, Applications, and Services*. ACM, jun 2020.